5-2009

Cardiac Cell Mechanics at the Single Cell Level

John Mcrae
Clemson University, jmcrae@clemson.edu

CARDIAC CELL MECHANICS AT THE SINGLE CELL LEVEL

A Thesis
Presented to
the Graduate School of
Clemson University

In Partial Fulfillment
of the Requirements for the Degree
Master of Engineering
Bioengineering

---

by
John Andrew McRae
May 2009

Accepted by:
Dr. Bruce Z. Gao, Committee Chair
Dr. Kenneth Webb
Dr. Gang Li

Abstract

The analysis of the cellular microenvironment is an area that has received much attention recently in the study of the tractions cells use for locomotion. Specifically, the study of cardiac cell mechanics is of particular interest as cardiac dysfunction is one of the leading causes of death in America. This progression is fueled by the need to have a system capable of reproducing mechanical environments before, during and after a dysfunctional event in order to fully characterize the causes and prevent any permanent damage. The current study proposes a system capable of providing quantitative measurements of the cellular microenvironment while concurrently allowing the same environment to be spatially controlled through collagen deposition and alignment. In this study, we have developed a system capable of characterizing the mechanical environment of contractile cardiac myocytes and migratory cardiac fibroblasts while concurrently allowing for fine control over cell position and alignment using a combination of Traction Force Microscopy with a deformable substrate and Finite Element Analysis. The results of this study indicate that this system can be applied to the study of the mechanical nature of cardiac dysfunctions like hypertrophy, myocardial infarction and hypertension.

Dedication

I dedicate this work to my grandfather John Rolland Singer who taught me how to be

"*The Master of my Fate; The Captain of my Soul*"

-Invictus, William Ernest Henley

Table of Contents

List of Equations, Figures, Graphs and Tables

Graphs **Page**

Tables **Page**

Chapter 1: Introduction

1.I. Cardiac Dysfunction

As the leading cause of death in America today, Heart Disease poses a prevalent and serious risk. In 2005, heart disease was recorded to have been responsible for 652,091 deaths according to the CDC [3]. Included in this figure are ischemic conditions (myocardial infarction), hypertensive conditions, atherosclerotic conditions and arrhythmic conditions. The heart is a complex organ consisting of chemical, mechanical and electrical pathways. Being a muscle, the heart utilizes a system of mechanical contractions in order to pump blood throughout the body. Cardiac contraction begins with pacemaker cells that are able to spontaneously contract. These contractions then propagate throughout the entire heart through electrical, chemical and mechanical pathways. Any deviations from this normal cardiac function, can potentially lead to organ-level and even cellular-level dysfunction.

Cardiac dysfunction is defined as an abnormal function in the heart. Thus, any aberration from normal cardiac function can be classified as dysfunction. For this study, we will focus on the mechanical aspects of cardiac dysfunctions; specifically, the dysfunction of individual cardiac myocytes, the basic functional cell in the heart. Many of the studies reviewed in this thesis illustrate the important role that proper myocyte mechanical function plays into normal cardiac function [5-7].

Many of the common cardiac diseases result in a mechanical dysfunction in one form or another. Myocardial Infarction, for one example, creates a dense scar in the

muscle of the heart. As a result the scar stiffens the heart and increases the stress on the remaining viable tissue. This stress then causes the individual myocytes to adapt to the dysfunctional mechanical condition. As an end result, the myocytes adapt to their new environment in order to attempt to maintain normal cardiac function. However, for reasons that will be discussed, the myocytes are not capable of surviving in this new mechanical environment and will eventually die leading to further damage or even death.

In order to fully understand, treat, and prevent heart diseases, the mechanical environment of heart tissue needs to be characterized. Many techniques have been utilized to understand the mechanical pathways in the heart; however, few are able to characterize the mechanical environment at the single cell level [4, 8, 9]. The current research proposes to produce a computational system capable of quantitatively analyzing the mechanical environment surrounding individual cardiac myocytes.

1.II. Thesis Goal and Outline

It is the goal of this research to create a system capable of characterizing the mechanical environment of specially designed myocyte cultures for the purpose of understanding the stress distribution of a normal and dysfunctional contractile myocyte. The specific objectives are defined as:

1. To show that aligned contractile myocytes generate smaller stresses than unaligned myocytes
2. To show that cells seeded onto stiffer substrates will generate stronger contractile forces

3. To demonstrate that this system is appropriate for the study single cell cardiac mechanics

We plan to show that the system we created is capable of meeting all of our objectives and our project goal. We accomplished this through the use of the Deformable Substrate Technique, Correlation-Based Optical Flow, Traction Force Microscopy and a Dynamic Simulation Technique. In Chapter 2, the details of normal and dysfunctional cell function will be outlined. In Chapter 3, the history of cell mechanical studies is discussed followed by the development of our tractional force microscopy system in Chapter 4. Chapter 5 gives an outline of our experimental procedure. Chapter 6 illustrates our results and Chapter 7 discusses the meaning of our results with respect to our project goal. Lastly, Chapter 8 will conclude the thesis followed by the appendices and references.

Chapter 2: Cell Function

2.I. Normal Cell Function

This chapter will look at cardiac myocytes and how they function *in vivo*. Specifically, this chapter focuses on the pulsatile mechanism, various forms of cellular communication both chemical and physical, and lastly on the importance of cellular orientation. Myocytes are the primary muscle cell in the heart and as such they undergo contraction. This process is similar to those seen in other striated muscle but there exist a few discrepancies. Myocytes are also a dynamic cell they experience consistent contraction, receiving signals from pacemaker cells. In addition to the typical chemical and molecular signals, myocytes must also accommodate for mechanical and electrical signals. Orientation is also important for myocyte function as well as overall cardiac function. Since myocytes are muscle cells, if they are not properly oriented with other myocytes then catastrophic imbalances in mechanical force can cause tissue death and lead to cardiac failure [10, 11].

2.I.A. The Pulsatile Mechanism

The cardiac myocyte is a specialized muscle cell that reacts to action potentials, induced either by an innervating axon or through cell-cell coupling, by contracting itself using actins and myosins. Through chemical and physical interactions these proteins with the addition of tropomyosin and Ca^{++} compose the fundamental unit that produces contractile force in each cell. These proteins are arranged into myofilaments, which in turn are bundled into myofibrils. Myofibrils contain units called sarcomeres, which are

what give myocytes their striated appearance. The following sections will lay out exactly how an action potential can lead to sarcomere contraction.

2.I.A.1. Sarcomere Contraction

The process where an action potential causes myocyte contraction is called Excitation-Contraction Coupling (ECC). A non-pacemaker cell, one that keeps a consistent resting membrane potential, contains special L-type Ca^{++} channels in its membrane. During normal signal propagation, the cell membrane will depolarize by opening inbound Na^{+} channels and closing outbound K^{+} channels, which results in a rapid increase in resting membrane potential from approximately -90mV to +10mV, which can be visualized in Figure 1 as Phase 0. Phase 1 represents the reopening of K^{+} channels and the initiation of repolarization. In skeletal muscle cells, this phase would restore resting membrane potential but it does not occur as rapidly as in cardiac myocytes and this is due to the concurrent opening of inbound the afore mentioned L-type Ca^{++} channels with the K^{+} channels. As Ca^{++} enters the cell, the repolarization is delayed and it takes considerably longer to restore resting membrane potential as seen in Figure 1 as Phase 2. Finally in Phase 3, Ca^{++} channels are closed and

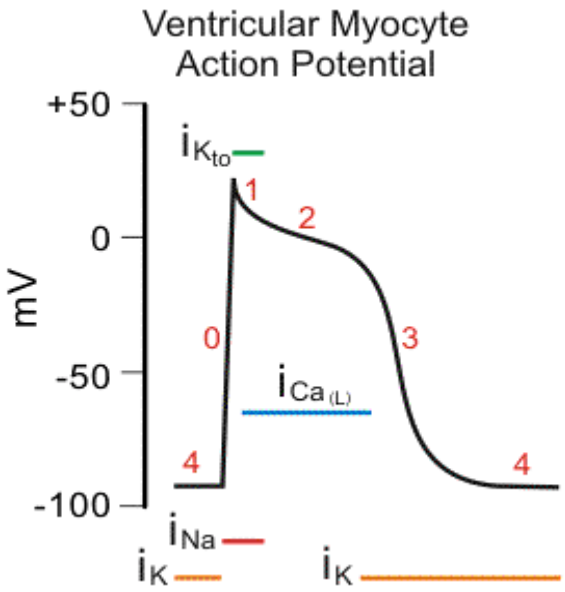

Figure 1. Ventricular Myocyte Action Potential.[1] **Phase 0**, Rapid Depolarization. **Phase 1**, Initial Repolarization. **Phase 2**, Plateau. **Phase 3**, Repolarization. **Phase 4**, Resting Membrane Potential.

resting membrane potential is established in Phase 4. One of the defining differences between skeletal and cardiac muscle cells is the distinctive plateau in Phase 2. Once inside the cell, Ca^{++} will stimulate a myocyte specific organelle called the Sarcoplasmic Reticulum (SR) and initiate the contractile mechanism.

The SR is a double membrane bound organelle like the endoplasmic reticulum that houses an abundance of Ca^{++} ions. It also contains channels in its membrane that will open in the presence of Ca^{++} in the cytoplasm. When these channels are open Ca^{++} will flood into the cytoplasm, effectively raising Ca^{++} concentration from 10^{-7} to 10^{-5} M. These channels remain open for only a short time, after which the Ca^{++} is then actively pumped back into the SR until the channels are opened again from Ca^{++} ions brought in through an action potential.

During this brief moment when the SR Ca^{++} channels are open and Ca^{++} ion concentration is elevated, the actin and myosin proteins are permitted to interaction and contraction occurs. Within the myofilaments are the contractile proteins: actin, myosin, troponin and tropomyosin. The organization of these fibers can be seen in Figure 2.

Myosin is a ~470 kD protein that makes up the "thick" filaments of the striations, which contains approximately 300 molecules. At the end of each filament are two heads which contain a myosin ATPase. This enzyme is normally inactive and can only hydrolyze ATP once it has bound to actin.

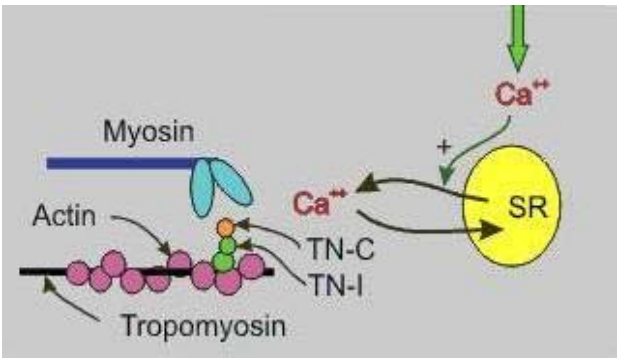

Figure 2. Cartoon of contractile poteins[1]

The other "thin"filaments are composed of three proteins: actin, troponin and tropomyosin called the Regulatory Protein Complex. The later of the three provides the structure with its rod-like structure, while the former two play a more active role in contraction. Actin is a globular protein that is arranged in sub-units that wrap around tropomyosin with an alpha helix structure. In the actin protein are active sites where the myosin head can attach and subsequentially activate the affore mentioned ATPase complex. To prevent these two sites on actin and myosin from uncontrolably binding and causing contraction, the actin sites are blocked from myosin binding by troponin.

Troponin consists of three sub-units: Troponin-T (TN-T) which is bound to tropomyosin, Troponin-I (TN-I) which blocks and inhibits the actin-myosin binding sites and Troponin-C (TN-C) which binds to free Ca^{++} ions. In the presence of elevated Ca^{++} ions (SR channels are open) TN-C will bind and conformationally change TN-I to expose the actin-myosin binding sites. Once exposed, myosin will freely bind to actin and the ATPase complex will become active. By hydrolyzing ATP, the actin-myosin complex will have a conformational change and the thick and thin filaments will begin to move past each other with a ratcheting motion generating contraction. This will continue as long as Ca^{++} levels are elevated. At the end of Phase 2 of the action potential, the SR and other Na-Ca exchange pumps will actively move Ca^{++} ions from the cytoplasm back into the SR or out of the cell, restoring the lower Ca^{++} levels. With the Ca^{++} concentration reduced, TN-C will return to its other conformational shape and as a consequence of this, TN-I will return to block the actin-myosin binding sites. The myosin heads will replace the hydrolyzed ADP with new ATP and the system will have reset in anticipation for the next action potential. Now that the inner mechanism of the contraction has been

presented, the next step in understanding the overall pulsatile mechanism is to look at how cells communicate contraction between each other. Intuitively, this can be done electro-chemically with action potentials but it can also occur through mechanical interactions as well [1, 2, 10, 11].

2.I.A.2. Signal Transduction

Cellular communication is a complex topic and many new discoveries are still being made. The most common concept of cellular communication is through chemical messengers which are secreted from one cell and bind to a receptor on another cell, initiating an intra-cellular reaction. However, one of the more direct methods of cellular communication is through cell-cell junctions. Junctions are places where the membranes of two adjacent cells either physically touch or share one or a complex of transmembrane proteins. Of particular interest to signal transduction in cardiac tissue are gap junctions and adherent junctions. In a general sense, these two junctions can be thought of as a medium for electrical and mechanical signals, respectively.

Gap junctions are named such because they create a direct thoroughfare between the cytoplasm of two adjacent cells and bridge the gap between them. Each junction is an aggregate of smaller proteins called connexins (Cx). Connexins are found

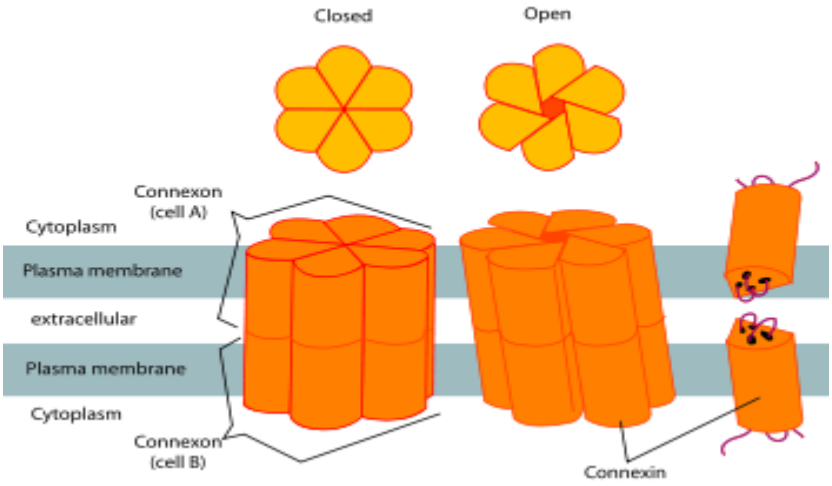

Figure 3. Cartoon diagram of gap junction structure [1]

in numerous cells in the body and have many isoforms: Cx-41, Cx-43, and Cx-45 among some found in cardiac tissues. The most predominant form of Cx in ventricular tissue is Cx-43 and as such has been extensively studied with relation to myocyte communication.

Connexins will naturally gather into a 2-3nm cluster called a Connexon (Figure 3), which will in effect act as the gap junction. Connexons have a distinct hexagonal shape as they are composed of six Cx proteins. The arrangement of Cx creates a hydrophilic tunnel that allows for the passage of molecules between the connected cells. In general, molecules up to 1kD can pass freely between gap junctions. Some of the more common molecules that are transmitted using gap junctions are cyclic AMP, nucleotides, glucose-6-phosphate and various ions. Inclusive in the later are Na^{+}, K^{+} and Cl^{-} which are implemental to the propagation of action potentials.

To help regulate the passage of molecules between cells, each junction has the capacity to be open or closed. Gap junctions will close when in the presence of certain molecules, known are a low pH and high concentrations of Ca^{++} although many others are predicted to exist. Gap junctions present rapid and direct communication between cells by sharing smaller molecules in their cytoplasm. It is in this fashion that ions involved in action potential propagation will travel through gap junctions from an excited cell to a resting cell where they will depolarize the membrane and continue the action potential. Also, as mentioned before gap junctions will close when high concentrations of Ca^{++} are in the cytoplasm. Thus during contraction gap junctions are closed, preventing undesired contractions in adjacent myocytes. Only when K^{+} concentrations induce an action potential will TN-I reveal the binding site for the myosin heads and contraction occur.

The second type of junction that has bearing on the pulsatile mechanism is the adherent junction. Adherent junctions are a broad group of junctions that are located at an intercalated disc that serves as an anchor while other transmembrane proteins reach across the extracellular space to connect to each other. These transmembrane proteins are common to all adherent junctions and are called cadherins (Cd). A general representation of an adherent junction can be seen in Figure 4. The specific type of adherent junction in ventricular myocytes is a ribbon-like structure called fascia adherens and contains N-cadherin (N-Cd). There have been many forms of cadherins found and it has been shown that cadherins exclusively bind to their own type; that is, N-Cd will only bind to another N-Cd. The reason for this is that it allows similar cell types to form exclusive adherent junctions with each other and prevents other cells in the vicinity from forming a connection. As a result, there have been many types of Cd identified in cells throughout the body.

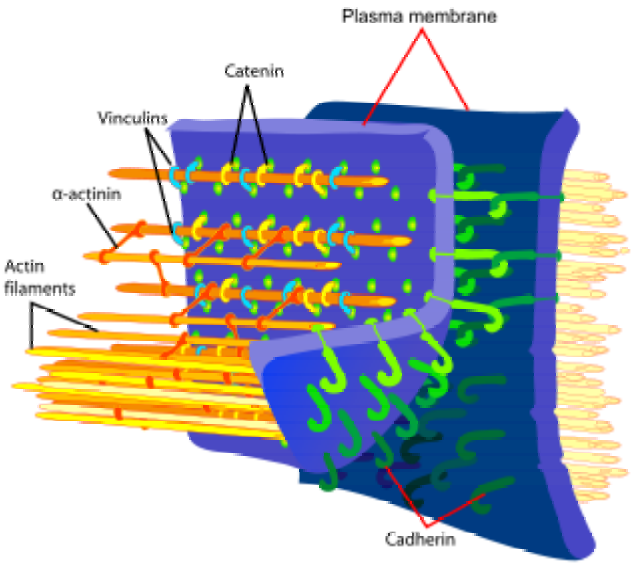

Figure 4. Cartoon diagram of adherens junction structure [2]

Intracellularly, Cds are bound to proteins called Catenins. There exist two subunits of catenins, α and β. When associated with Cd, both α and β catenins act as a linker between Cds and F-actin filaments, not to be confused with actin in the sarcomere. Vinculins are proteins that in adherent junctions function in the same manner as catenins

and structurally are similar to α-catenin. By binding to actin filaments in the cytoskeleton, adherent junctions create a complex that allows for a cell to impose mechanical force on the cytoskeleton of adjacent cell. Mechanical interactions between cells, which will be covered more thoroughly in the following section, are made possible through adherent junctions and help myocytes coordinate contraction [1, 2, 11].

2.I.A.3. Mechanical Interactions

Myocytes are connected to their environment not only through chemical and electrical signals but also through mechanical signals. All muscles, especially the cardiac muscle, are very mechanical by design and as such their cells need to be aware of the physical nature of their surroundings. Myocytes form lateral mechanical connections with other cells as well as basal mechanical connections the ventricular ECM, of which adherent junctions are only one type. Cells may also form tight junctions as well as desmosomes, but adherent junctions have been the primary junction of interest when looking at ventricular myocyte studies. Myocytes, as discussed in the section 2.I.A.2, will form junctions between other myocytes and will also form junctions with cardiac fibroblasts. These junctions can provide a different set of signals, which will be discussed in later sections pertaining to cardiac dysfunctions.

Myocyte-myocyte lateral mechanical junctions serve allow myocytes to control and adapt their contractions. For example, it has been shown that when a sarcomere receives an action potential, the resulting contraction will generate more tension if the cell is being stretched. This phenomenon has been called Length-Dependent Activation. Studies show that applying a preload to myocytes will increase the affinity of TN-C for Ca^{++}, which would increase the rate of actin-myosin attachment and detachment and thus

increase the tension developed by the sarcomere. Knowing this, having mechanical force transmitted through adherent junctions from adjacent cells could significantly amplify the resulting tension from contraction. In maladaptive situations where myocyte-myocyte mechanical junctions are disrupted, reorganized, damaged or destroyed serious pathologies will result; emphasizing the critical role that mechanical interactions play in contractile function and regulation.

Interactions between myocytes and fibroblasts are less clear. Fibroblasts are motile cells that primarily maintain ECM by creating and constructing collagen fibers. However, fibroblasts can also assist with regulation of contraction. Mechanically, fibroblasts are motile and will exert force on surrounding cells. They help to transmit mechanical signals propagated from cells and signals that mediate the ECM. In the presence of dysfunctions like hypertrophy and infarct scars, fibroblasts can increase the tension and contractile force of the viable cardiac tissue. Since these interactions are multi-faceted and not only mechanical, they will be discussed in 2.II.A

Lastly, cell-ECM mechanical interactions are mediated primarily through junctions called focal adhesions (FA). FA can be considered as sub-cellular macromolecules that mediate the regulatory effects of ECM adhesion on cell behavior. Focal adhesions serve as the mechanical linkages to the ECM, and as a biochemical signaling hub to concentrate and direct numerous signaling proteins at sites of integrin binding and clustering. Proteins will bind to FAs through specific amino acid sequences and transmit signals to the cytoskeleton through catenins or other heterodimers, similar to connections seen in adherent junctions. In addition to anchoring cells, FAs help to keep cells informed about the condition of the ECM. Thus in periods where contractile rates

are required to change (exercise) the ECM can easily increase the pre-load stress on myocytes leading to a stronger contraction.

In summary, the pulsatile mechanism is a complex system that can change an action potential into cell contraction through Ca++ release and actin-myosin binding. These contraction rates are then controlled by the cell and the environment in various ways. Cells can control contraction through gap junctions and adherent junctions and by imposing pre-stresses on adjacent cells. Also, other proximal cells as well as the ECM can change contraction by applying mechanical stresses onto myocytes. In the next section, the development and regulation of myocytes will be discussed. It will confer those proteins and molecules that play a part in the development of myocytes and their function in maintaining normal cardiac function [2, 12, 13]

2.I.B. Myocyte Development and Regulation

Myocyte development and regulation is controlled by the rate, location and concentration of signals in the form of proteins and molecules. In order for a myocyte to function normally in cardiac tissue, it must be assembled properly and its functional proteins and pathways must be complete. Of particular importance to the current discussion are Angiotensin II (Ang II), Atrial Natriuretic Factor (ANF), Cx43, N-Cd, α-actin isoforms and Myosin Heavy Chain isoforms. In the following sections, each of these factors will be discussed emphasizing their role in myocyte function. Lastly, those signals which have spatial importance, the significance of changing orientation and position will be briefly discussed.

2.I.B.1 Soluble Signals: Angiotensin II and Atrial Natriuretic Factor

Cardiac cells are exposed to large numbers of signals at any one moment. The most commonly observed form of cellular communication is in the form of soluble signaling molecules or proteins. These signals are typically generated by a cell for a particular purpose. They are secreted the cell and will bind to integrins of surround cells, the cell that secreted the signal or the signal may enter the blood stream and bind to cells downstream. Some of these signals affect the cell's function in more drastic ways that others. Two soluble signaling peptides that have received particular attention due to their pivotal role in cardiac function are Ang II and ANF. Both of these can either directly or through a system interactions change blood pressure and myocyte contraction.

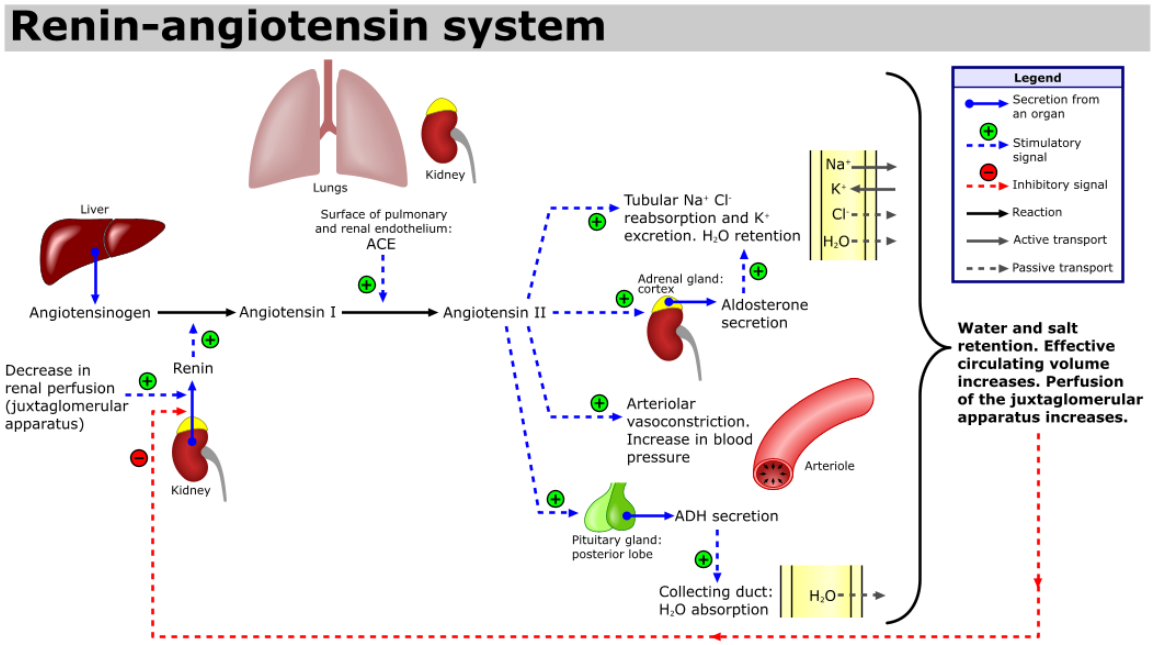

Figure 5. The Renin-Angiotensin System (RAS) [1]

Ang II is an oligopeptide hormone that circulates in the blood stream that causes vasoconstriction and is a major component of the Renin-Angiotensin System (RAS) (Figure 5). The RAS is a controlled system that the body uses to increase the circulating

blood volume in response to decreased perfusion of juxtaglomerular apparatus in the kidneys from water and salt loss. When this occurs, the kidney will release the hormone renin into the blood. Renin will then cleave another hormone called angiotensinogen, which is constitutively secreted by the liver, to form Angiotensin I (Ang I). Ang I is then converted to Ang II by Angiotensin-Converting Enzyme (ACE), which is predominantly present in capillaries of the lungs and kidneys. Among other functions, Ang II will increase the level of water reperfusion in the kidneys and will induce contraction of vascular smooth muscle cells via an IP3-dependant mechanism which increases blood pressure. Ang II lasts approximately 30 seconds in circulation before it is degraded to Angiotensin III by angiotensinases located on red blood cells and most vascular beds. But, if Ang II diffuses into tissues it can last up to 15-30 min. With its ability to induce contraction of muscle cells, it is apparent that long term overexposure of Ang II to myocytes in ventricular tissues can cause increased stresses that could lead to cardiomyopathies and overall dysfunction. The function of Ang II in cardiac tissues does not always lead to problems. In controlled, adaptive hypertrophy during development Ang II can induce cardiac cell growth. It is thought that this mechanism by which Ang II induces this adaptive hypertrophy in juvenile myocytes is similar to the mechanism involved with maladaptive hypertrophy of mature myocytes [2, 7, 14, 15]. In order to counter balance the RAS, the body uses another peptide called Atrial Natriuretic Factor (ANF).

ANF is a hormone that is released by atrial myocytes in response to high blood pressure. It is also expressed in ventricular tissues is response to high levels of stress that result from increased afterload or injury. ANF levels have been shown to increase in

response to exercise. Thus, ANF can be used in research to evaluate chronic elevated blood pressure. If high levels of ANF persist without achieving a necessary drop in blood pressure, it could indicate the presence of dysfunction. Also, it has been shown that groups of mice lacking ANF receptor NPRA develop an increase in cardiac mass, fibrosis and sudden death. However, if NPRA is re-expressed in these mice, the cellular phenotype is restored, pointing to the pivotal role of ANF in cardiac function.

Both Ang II and ANF play important roles in regulating both blood pressure and cardiac muscle tensions. Maintenance of normal cell and tissue function rely heavily on the regulation of both proteins. In situations where Ang II and ANF regulation is hindered or lost (such as in the presence of infarction or hypertension), blood pressure becomes unstable and can lead to maladaptive hypertrophy, which will be discussed further in section 2.II.

2.I.B.2 Structural Proteins

Soluble factors play an important in myocyte development and regulation but many other facets of signaling and signal transduction contribute equally to overall normal cell function. In order for a cell to respond in the designed phenotypic fashion, it must be constructed to do so. Specifically, the structural proteins that make up the sarcomeric unit: actin and myosin. During development and maturity, differing isoforms of both of these proteins are employed by myocytes as compared to the isoforms seen in mature myocytes. The differences in these proteins will be discussed in the following section and the significance of the preference in isoforms will be demonstrated.

Actin is globular protein and is found in all eukaryotic cells. They are the monomeric unit of microfilaments, one of three major fibers that comprise the

cytoskeleton, and of thin filaments in the sarcomere. Actin isoforms are divided into three distinct groups: alpha, beta and gamma. Beta and gamma actins are primarily found in non-muscle cells while alpha actins are primarily found in muscle cells, most of which are in the sarcomere. Of particular interest to this discussion are three alpha actin isoforms: α-skeletal (α-sk), α-smooth muscle (α-sm) and α-cardiac (α-cd). Their predominant locations in a mature person are evident from their names. However, during development the locations of their expression vary [7].

During early development of cardiac tissue, before the establishment of a tubular heart, α-sm actin is expressed. As development progresses expression of α-sm is reduced as α-sk and α-cd expression increases. In the mature myocardium, α-cd becomes the major actin isoform in the myocardium while α-sk becomes predominant in the whole cardiac tissue [16]. It has been shown that each form of actin is important in its own way. The structure of α-cd differs from α-sm by four substitutions and from α-sk by eight substitutions. Also, a study performed by Kumar et al. demonstrated that repression of α-cd coupled with an overexpression of α-sk and α-sm in prenatal murine fetuses did not yield a viable pup [17]. Thus, the order and resulting location of α-actin expression is crucial to cardiac development and regulation.

Myosin is another structural protein that plays a role in development and regulation of cardiac function. It is a motor protein that utilizes ATP hydrolysis to fuel moving along actin filaments in the sarcomere. The process of cardiac development involves a switch of myosin isoforms as the tissue matures, as seen with the conversion from α-sm to α-cd. There are two isoforms of myosin in cardiac muscle units that are seen in juvenile and mature cardiac tissues: Myosin Heavy Chain-α (MHCα) and Myosin

Heavy Chain-β (MHCβ) and both forms are present in different concentrations depending on the stage of cardiac development.

In early fetal development, MHCβ is expressed in ventricular tissues and MHCα is expressed in atrial tissues. The functional differences between these isoforms has been shown in experiments to have shown that MHCβ results in a 40% reduction in unloaded shortening velocity and a similar reduction in the rate of ATP hydrolysis. The molecular basis for these discrepancies has been shown to lie in amino acid differences in the myosin protein; specifically in the myosin rod, the hinge, the light chain domain, the actin binding site, and the ATP binding site [18]. Functionally, MHCβ is called the "slow twitch" isoform and works better with the reduced loads required by the juvenile heart. However, at the end of maturation, the heart favors MHCα almost completely over MHCβ. The reason is that MHCα is able to generate higher loads in faster times, which the mature heart requires. Thus, in a healthy mature heart, MHCα is present in ~90% of cardiac tissues and MHCβ is almost entirely replaced. However, when the heart undergoes excess stress or damage, MHCβ has been shown to be re-expressed in high quantities (~50%) [19]. This reemergence of the juvenile isoform is part of a process cells may undergo called Dedifferentiation and will be discussed further in 2.II.A.1.b.

So far, the function of the soluble factors Ang II and ANF as well as the function of actin and myosin isoforms have been discussed in relation to cardiac development and function. One last factor that is important to development and function of cardiac tissues deals with cell alignment in terms of how that cell is organized and how it relates to other adjacent cells.

2.I.B.3 Cell Alignment

Cell alignment is a feature that can be more important in some cells than in others. Cardiac tissue, for one, is highly dependent on its anisotropic arrangement. Mature myocytes have a rod-like phenotype that accommodates optimal cardiac function. Contraction occurs along the long axis of myocytes to generate the most force it can through its sarcomere. In addition, cell junctions are arranged in ways that conduct signals best when the cell is properly aligned in its rod-like phenotype. However, cells need to have external cues that let them know the proper alignment. This is done through the alignment of collagen fibers in the ECM, which are synthesized and set up by cardiac fibroblasts. Part of the response of myocytes to changes in the normal mechanical or electrochemical signaling pathways induce the cell to undergo a process of remodeling, which may be a form of de-differentiation and will be discussed further in 2.II.A.2. Part of this process is that the cell loses its rod-like shape and takes on an amoeboid shape, changes its phenotype and looses its anisotropic functionality. This process plays an important role in the following discussion of cell alignment. The following section will discuss why cell alignment is necessary for proper cell function by looking at these factors.

The mechanics of sarcomere formation is still under debate. There is discussion about the order of synthesis and the presence of intermediates in thin and thick filament formation [20]. However, one accepted fact is that sarcomere formation follows the underlying stress pattern present in the tissue. Regardless of the assembly, it is always seen that sarcomeres will assemble in myocytes with their striations perpendicular to the direction of contraction. Also, this sarcomere alignment reflects the overall cell alignment

with the striations perpendicular to the long axis of the rod-like myocyte. Functionally, this is the most effective sarcomere alignment and achieves the best cardiac output. In cases where the cardiac output is less than desirable and dysfunction is present, sarcomere alignment has been shown to change. For reasons that will be discussed in 2.II, pathologies like hypertrophy and myocardial infarction disrupt the normative stress distributions in cardiac tissue. Myocytes will react to this change in stress by attempting to accommodate its function by remodeling its sarcomere orientation. The result is that contractile anisotropy is lost as myocytes are no longer rod-like with perpendicular sarcomeres and the contraction of one myocyte may interfere with the contraction of another, drastically reducing cardiac output.

Similar to sarcomere alignment, cells will align their junctions to maximize signal transduction during contraction. Intercalated discs, which house many cell-cell junctions like gap and adherent junctions, are located at the ends of the rod-like myocyte.

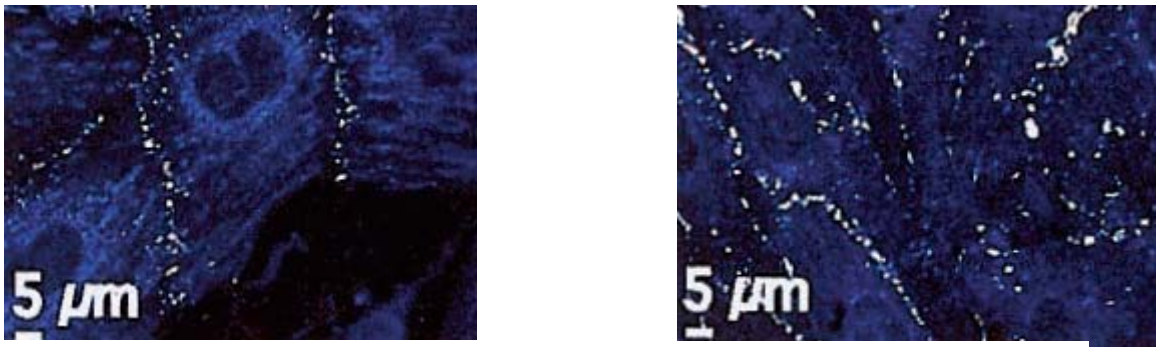

Figure 6. Gap junction relocation. [4]

a) Gap junctions are located at the ends of myocytes **b)** gap junctions have relocated all around the cell membrane

Specifically, gap junctions have a major role in the electrophysiological function of the cardiac tissue (Section 2.I.A.2). In the presence of cellular remodeling typically initiated by dysfunction, the electrophysiologic anisotropy is lost as gap junctions migrate from the ends of the myocyte (Figure 6). Gap junction relocation, like sarcomere realignment,

is an attempt to accommodate to the change in stress. The result is a change is contractile signaling that can result in arrhythmia and interfering contractions between myocytes [21].

Both sarcomere realignment and gap junction relocation are examples of intracellular processes that show the importance of cell alignment, but the extracellular microenvironment also affects cell alignment; specifically, through collagen fiber alignment in the ECM. During cardiac development, collagen fibers are synthesized and deposited into the ECM by cardiac fibroblasts. These fibers provide a scaffold in which myocytes will align themselves as stresses are propagated through the ECM. Myocytes will form focal adhesions to the collagen fibers and the cell will be connected to the ECM for the duration of the cell's life. However, in the presence of cardiac dysfunctions, collagen arrangement is altered and the previous aligned scaffold is lost. Also, the total collagen volume is disproportionate to that in normal functional maturity. Mechanically, this results in a stiffening of the ECM in addition to a further loss of alignment [22].

This section conferred factors that are important to this discussion of cardiac function. The role of the soluble factors Ang II and ANF as well as the role of the isoform of structural proteins was discussed in relation to how they help in the maturity and normal function of cardiac myocytes. Also, the role of cell alignment was discussed and the intracellular and extracellular factors that can affect it. The purpose the previous section was to elaborate on factors that not only affect functional normality but are integral during cardiac dysfunction. The next section of Chapter 2 will discuss cardiac hypertrophy and myocardial infarction. Many of the topics covered in the previous

section will be shown to have significant effects on the initiation and progression of these forms of cardiac dysfunction.

2.II. Cardiac Myocyte Hypertrophy

The term hypertrophy is defined in various ways from source to source, but all definitions include a version of the following: Hypertrophy is the heart's response to a combination of extrinsic and/or intrinsic factors that result in an increase of cellular/myocardial mass [23-31]. At the cellular level however, hypertrophy describes a change in phenotype defined by cytoskeletal proteins, extra- and intra- cellular factors, surface proteins, alignment of the sarcomere and its mechanical behavior [4, 5, 7, 23-33]. Whether cell-level hypertrophy yields tissue- and organ-level hypertrophy dictates the presence of cardiac dysfunction.

Normal growth of the cardiac muscle generates an increase in the overall size of the heart but it is done while preserving the ratio of the heart wall to the ventricular volume which is to maintain ventricular ejection and cardiac output. During this process, individual cardiac myocytes may undergo cellular hypertrophy but due to cellular plasticity and replication of juvenile cardiac myocytes during maturation as well as other pathways (pregnancy or exercise) the heart itself does not hypertrophy. Cardiac dysfunction stemming from organ-level hypertrophy occurs when excess stress is placed on the heart as mature and possibly terminally differentiated myocytes hypertrophy [5, 7, 34]. To distinguish these two situations, researchers and physicians have coined hypertrophy during normal activity as "physiological" hypertrophy and hypertrophy

during dysfunctional activity as “pathological” hypertrophy. Although these terms are more accurate, there still remain discrepancies and similarities that are still being researched [5, 35].

Examples of physiological hypertrophy occur during normal cardiac maturation, pregnancy and chronic exercise. During these events, the heart will increase in mass with no dysfunctional after effects on the muscle. However, current research suggests that the mechanisms in each onset of hypertrophy will differ, which can be presumed as the stimuli are very different. Since the mechanistic details are yet to be clearly defined, we cannot clearly define each instance of hypertrophy is “physiologic” or “pathologic”. In fact, they may contain many similar mechanisms. In lieu of the terms “physiologic” and “pathologic”, “adaptive” and “maladaptive” have been suggested which may be more accurate when describing a hypertrophic event. Adaptive hypertrophy being cellular-level hypertrophy with normal or improved contractile function and maladaptive hypertrophy being cellular-level hypertrophy with impaired contractile function [5, 7, 24, 28, 35, 36]. These terms prevent hypertrophy from being mislabeled but ensure a less specific diagnosis.

This is necessary though, as research progresses we are finding that pathways we thought previously to be isolated to have many common mechanisms. To illustrate the benefit of these descriptors, consider cardiac hypertrophy resulting from exercise. This organ-level physiologic hypertrophy will increase ventricular ejection as well as contractility without any loss in myocytes function. However, in the instance where the heart has postischemic damage, pathologic hypertrophy can occur from a previously physiologic stimulus[37, 38]. Whereas, we may say that the non-ischemic heart had an

adaptive response and the postischemic heart had a maladaptive response based on the resulting organ function. Until we have uncontested (or at least highly detailed) molecular, cellular and organ-level pathways, it would remove uncertain diagnoses to use "adaptive" and "maladaptive" rather than "physiologic" and "pathologic" [5]. What is currently known about the cellular mechanisms of hypertrophy will be the subject of the next sections.

2.II.A. Cellular Mechanisms of Hypertrophy

The hypertrophic phenotype is marked with the upregulation of fetal genes for α-skeletal (SK) and α-smooth muscle (SM) actin, β-myosin heavy chain (βMHC) and atrial natriuretic factor (ANF) while downregulating α-myosin heavy chain (αMHC) and Ca pumps in the endoplasmic reticulum with a rearrangement of cellular junctions like connexins, cadherins and focal adhesions. The end result is a myocyte that has lost its rod like shape, has changed to an amoeboid phenotype and lost its contractile alignment. The genes upstream of the fetal genes, or early-onset genes, activate within 30-60min after exposure in a pressure overload model. Some known genes are *Egr-1, Hsp70, c-fos, c-jun, and c-myc*. The changes in MHC, actin and ANF expression are seen 6-24hr after exposure [5, 7, 39-41]. As previously stated the stimuli that initialize these changes in gene expression are numerous, including but not limited to growth factors, cytokines, catecholamines, vasoactive peptides, hormones and mechanical loading [42-45].

2.II.A.1. Cell-Cell Junctions

It is known that hypertrophy interferes with normal myocyte electrical and mechanical conduction, which is associated with an increased susceptibility ventricular dysfunction [46-48]. Changes in cell-cell coupling during hypertrophy are theorized to have a detrimental effect on cell membrane depolarization and conduction. The junction proteins involved in these functions appear to be affected by the process of hypertrophy. It has been suggested that the presence of Ang II and cAMP, early moderators of hypertrophy, will upregulate the expression gap junction proteins [4, 49, 50]. Also, as the myocyte hypertrophies, it increases in size. This increase in size promotes cell-cell adherent junctions, which regulate mechanical transduction between myocytes. Thus, if hypertrophied myocytes have more adherent junctions then they might amplify mechanical signals creating regions of anisotropic force distribution in the ventricular tissue, resulting in arrhythmia as well as promoting further cellular hypertrophy [51-53].

2.II.A.2. De-differentiation

Myocyte de-differentiation is a phenomenon that has been observed in the presence of many cardiac dysfunctions: hibernating myocardium [54], fibrillation [55], infarct [56] and maladaptive pressure-overload hypertrophy [57]. The term is defined as a change in the cell such that it no longer resembles the adult phenotype but rather a more an embryonic or a fetal phenotype. Specifically, the cell will attempt to compensate for an increase in blood pressure or blood volume by growing. This is done by expressing immediate early genes which control cytoskeletal composition. As mentioned in 2.1.B.2., α-cd is the dominant actin isoform present in adult myocytes. During de-differentiation,

the cell will down regulate α-cd expression and up regulate α-sm, which is reminiscent of the fetal phenotype. With α-sm composition in the cytoskeleton increased, the cell becomes more plastic and looses its rod-like shape and becomes more amoeboid. In this state, the cell can rearrange itself to respond to the mechanical environment that has been changed from dysfunction. In addition to the change of actin isoforms, many other changes in phenotype are hallmarks of de-differentiation: myolysis, glycogen accumulation, dispersion of nuclear chromatin, changes in mitochondrial shape and size, loss of the sacroplasmic reticulum as well as a change in expression of titin, MHC, troponin and desmin [58]. Some studies have proposed that the nature of this cellular change may be reversible following the restoration of normal cardiac function. However, many results have shown that other factors contribute to the maintenance of de-differentiation which has led to cellular apoptosis [59].

One factor that has shown to have an effect on the reestablishment of the adult myocyte phenotype is the presence of cardiac fibroblasts. In a study done by Rücker-Martin in 2002, the effect of the presence of fibroblasts in a culture of de-differentiated myocytes was performed. The results showed that in the absence of fibroblasts, the adult phenotype was reestablished 3-4 weeks after being removed from a dysfunctional stimulus and exposure to cytosine b-D-arabino-furanoside (ara-C), a substance that prevents proliferative cells like fibroblasts from replicating. While cultures that were cultured without ara-C (fibroblasts present) demonstrated myocytes that did not retain the atypical rod-like phenotype and instead had random orientations of cytoskeletal proteins, cell-cell receptors and sarcoplasmic orientation [60]. This would suggest that fibroblasts

play some role in the recovery from the de-differentiated phenotype observed during maladaptive hypertrophy as well as other cardiac dysfunctions.

2.II.B. Causes of Maladaptive Hypertrophy

As previously stated, tissue- and organ-level maladaptive hypertrophy typically results from an underlying dysfunction and prolonged hypertrophy increases risk of cardiac failure and death [28]. Hypertrophic compensations are known to occur with arrhythmia, high blood pressure, hypertension, congenital conditions and myocardial infarction (MI) [7, 61]. In theory hypertrophy can result from various cardiomyopathies; however, these dysfunctions have a high correlation to maladaptive hypertrophy.

Cardiac arrhythmia (also dysrhythmia) is a term for any of a large and heterogenous group of conditions in which there is abnormal electrical activity in the heart. The heart beat may be too fast or too slow, and may be regular or irregular. Many types of arrhythmias exist such as tachycardia (accelerated heart rate), bradycardia (slowed heart rate), automaticity (non pacemaker cells fire automatically), re-entry (circular conduction) and fibrillation (micro re-entry events occurring throughout tissue causing chaotic impulses). During any of the previous events, signal conduction changes in the cardiac tissue and cells beat in an unnatural fashion. The more common occurrences of maladaptive hypertrophy with arrhythmias results from an increase in the cyclic stress resulting from tachycardia and from misdirection of contraction signals during fibrillation [62].

High blood pressure and hypertension (high atrial pressure) can both contribute to maladaptive hypertrophy in similar ways. One of the stimuli that cardiac myocytes use to

regulate cell morphology and contraction is pressure. The effects of pressure on cardiac tissues are well documented and show that an increase in ventricular pressure will lead to increase contractile load and increase the stress on myocytes. Such a scenario can be generated by a change in Ang II or ANF levels. In such an environment, myocytes will adapt by hypertrophying through genetic re-expression of fetal isoforms of structural proteins as mentioned in section 2.I.B.2. In this fetal state, the cell is unable to support the increased loads over extended periods of time and will die leading to tissue and organ failure.

There are also individuals who have a genetic predisposition to hypertrophy and suffer from Familial Hypertrophy Cardiomyopathy (FHCM). This disease is autosomal dominant condition that is characterized by the presence of hypertrophy in the absence of other causes of hypertrophy. The specifics of this disease are still being debated however there is evidence to suggest spontaneous mutations of genes that produce βMHC, TN-T and tropomyosin [61].

Lastly, MI (heart attack) has a high correlation of hypertrophy after the infarct. MI is a condition where a section of the heart is necroses after a loss of blood supply through coronary arteries, most typically through a blockage from an atherosclerotic plaque. When blood supply is lost, a section of the heart muscle dies and the contractile ability of the muscle is severely affected. Because of this dead area of cardiac tissue, the contractile force of the muscle has a solid area that must be circumvented in order to generate a total contraction. As mentioned in section 2.1.A., cardiac contraction is induced by an electrical signal that moves through the tissue. When the signal reaches the infracted area, it must go around in order to reach those cells on the other side. When the

signal changes direction, it also changes the orientation of the myocytes as the contractile signal helps direct the cell contraction orientation. Thus, the remaining myocytes are receiving a contractile signal in an anisotropic direction and rearrange the normal contractile orientation of cells. In addition to the change in orientation, the amount of stress that cells are required to generate is greatly increase as they attempt to compensate for the cells that died during the infarction. For reasons discussed earlier, the additional stress in addition to the anisotropic contractile signal leads to maladaptive hypertrophy of the myocytes surrounding the infarcted area. As the hypertrophic environment persists, these cells will die under the increased load and the dead infarct area will, in effect, enlarge inducing more cells to undergo maladaptive hypertrophy.

2.III. Mechanical Regulation in Myocyte Function

The mechanical micro-environment of cardiac myocytes is heavily influenced by the conduits with which mechanical force is transmitted: cell-cell interactions and cell-ECM interactions. A large proportion of cell-cell mechanical interactions occur at adherent junctions. As discussed in Section 2.I.A.2, these junctions allow for communication between myocytes in order to regulate the contractile mechanism and overall cardiac pulsatile function. Cell-ECM mechanical interactions occur at focal adhesions. As discussed in Section 2.II.A.3, focal adhesions allow for the cell to receive mechanical information from the ECM which is processed and used to regulate the contractile mechanism. In the following section, the specific roles that mechanical junctions have on myocyte contractility will be discussed both during normal tissue

function and dysfunction, followed by what is to be desired of research tools in order to increase the body of information pertaining to myocyte mechanical regulation.

2.III.A. Normal Myocyte Function

In the absence of cardiac dysfunctions, mechanical regulation is pivoted around pathways and cellular mechanisms where the signal at one point is in the form of a force, which indicates that the cell's cytoskeleton will be affected in some fashion. Of the various types of cell junctions, adherent junctions and focal adhesions represent cell-cell and cell-ECM junctions that are capable of translating either chemical or mechanical extracellular signals into intracellular mechanical signals.

Contractile function in myocytes is controlled by both electro-chemical signals and mechanical signals. It is known that the contractile fibers of myocytes are stimulated primarily through Ca^{++} release in the sarcoplasmic reticulum; however the amount of stress generated during contraction is also affected by pre-stress. This pre-stress is the tension present in a sarcomeric unit when it is not undergoing contraction, in other words when Ca^{++} levels are such that they block actin-myosin binding. Pre-stress can affect the total force generated by increasing or decreasing the tension in the sarcomeric unit, discussed in Section 2.I.A.3 called Length-Dependent Activation. Pre-stress is maintained intracellularly through the cytoskeleton by keeping the cell structure rigid and two major pathways that control cytoskeletal stiffness involve adherent junctions and focal adhesions.

Adherent junctions relay cell-cell mechanical signals by providing connections though extracellular molecular connections at intercalated discs at the polar ends of myocytes. These connections directly link one cell's cytoskeleton to the cytoskeleton of

another cell. Thus, if one myocyte is receiving signals to elevate or reduce its pre-stress, the other cell will also change its pre-stress accordingly. In this fashion, electro-chemical signals are converted to mechanical stress and then transferred between cells through adherent junctions. This mechanism helps to keep cardiac tissue at a more uniform pre-stress and prevent accumulations of stress which may interfere with contractility and overall organ function [63].

Focal adhesions are connections that cells make with the ECM. Focal adhesions are used for many purposes in various cell types, which include the translation of mechanical signals to intracellular and genetic signals which the cell can use to read its environment. It is known that focal adhesions contain many types of signaling complexes including: Focal Adhesion Kinases [64], Src Tyrosine Kinases [65], PTP-TEST phosphatases [66], Rho Kinases [67] and FAK as well as other pathways. These adhesions bind to ECM proteins such as fibronectin and collagen. It has been found that external ECM stress can induce cells to assemble focal adhesions at the site of application of the force and even help the adhesions mature (assemble most of the known components). Of particular interest in external force regulation is the FAK pathway. It was found that cells that were genetically modified to not express FAK were incapable of responding to increases in the rigidity of their substrate by changing their pre-stress. Thus it is consistent that FAK is regulated in fibroblasts, the cell type most responsible for the composition of the ECM. By using the ECM, myocytes can obtain stress information about their environment and other cells such as fibroblasts that influence the ECM have sequential control over the pre-stress of myocyte through the focal adhesion mechanism [68, 69].

2.III.B. Understanding Myocyte Mechanical Behavior

At this point, the necessary biologic pathways and mechanisms have been discussed to the degree required to look at studies aimed at mechanical behaviors of cardiac dysfunctions. First, considerations in the treatment and prevention of maladaptive hypertrophy will be discussed. Then the requirements of technologies in the promotion of study for such dysfunctions will be briefly discussed. Lastly we will present how our system developed to study myocyte cell mechanics fills the requirements of current research as well as opening a new venue for the study of cell mechanics through fine control of the cell microenvironment using traction force microscopy and laser micropatterning.

Most common treatments for individuals with a maladapted myocardium are to reduce cardiac stress as much as possible, to take medications that will reduce blood pressure or to have operations to help improve overall cardiac function. The overall goal is compensatory action, to help the individual adapt to the dysfunctional condition of their heart. After the point where the cardiac mass begins to undergo hypertrophy there is no known method of restoring the myocytes to their original adult state due to the permanent reconstruction of the cytoskeleton and sarcomere orientation. Similarly for a heart attack, the viable cells proximal to the dead scar tissue become permanently dedifferentiated for compensatory reasons to maintain stroke volume. At this point, individuals who have begun maladaptive hypertrophy have little chance of restoring the functional adult heart [60, 70]. Thus, it is imperative that all is done to prevent situations

like this from occurring. In order to do so, we must fully understand the conditions and the mechanical signals that insight these cardiac dysfunctions.

To better understand and thus to better prevent cardiac dysfunctions like maladaptive hypertrophy, we need to understand all of its facets. Mechanical signaling is just one side of this dysfunction but it is crucial as mechanical forces are a largely connected to heart function. Thus, much research has been performed in order to study cardiac cellular mechanics under normal and dysfunctional environments. Many tools have been created to qualitatively and quantitatively assess these forces through a deformable substrate and cell traction microscopy to name a few [32, 71]. Much of what has been done utilizes systems that apply force to cardiac cells and the cells response is measured. This research, which will be the subject of Chapter 3, has discovered many aspects of myocyte mechanics that has been crucial in pushing the knowledge base of cardiac dysfunction even further. However, the time has come to establish a new tool capable of creating more *in vivo* like microenvironments as opposed to simply measuring cells plated onto a deformable substrate. We have developed a system capable of generating precisely controlled cellular microenvironments while also capable of quantitatively measuring the mechanical forces the cells generate. This system utilizes techniques such as Traction Force Microscopy, which includes The Deformable Substrate Method, Correlation-Based Optical Flow and Continuum Mechanics, as well as Laser Micropatterning. To clarify upon these techniques as well as establish their place in the progression of cellular mechanic studies, the following chapters are dedicated to those subjects. Chapter 3 will discuss the research history and progression of the study of cardiac cellular mechanics. Chapter 4 is devoted solely to Traction Force Microscopy as

it is instrumental to this project. Chapter 5 will explain the components and goals of this project in relation to the mechanics of cardiac dysfunction discussed in this chapter and the techniques used to study cardiac cell mechanics discussed in Chapters 3 and 4.

Chapter 3: Cardiac Mechanical Studies

3.I. Stretch Modulated Mechanical Studies

One of the earlier and most direct methods of testing the response of a mechanical stimulus was to directly apply force to a cell culture and observe any changes. One example of such a study was done by Cooper and Tomanek. In this study, the response of feline cardiac tissue was observed during a controlled unloading due to loss of blood pressure. Sections of tissue were collected and connected to a photoelectric displacement transducer on one end and to a semiconductor strain gauge on the other end. Through this technique, the mechanical strain was measured and quantitative data was obtained [72]. While it is the most direct testing method it leaves many uncontrolled variables and makes precise conclusions difficult to reach. However, through these methods more modern techniques of applying specific and localized mechanical forces have been derived. In this chapter, the earlier studies in observing the application of mechanical force to cardiac cultures for hypertrophic cues will be presented. First studies that applied uniaxial stretch to cardiac cell cultures will be discussed, then studies that utilized biaxial stretch and lastly studies that used anisotropic stretch.

3.I.A Uniaxial Stretch Studies

Uniaxial Stretch refers to a test that applies stress along only one axis of a two dimensional cell culture surface. This stretch has been applied either parallel to the axis

of contraction or perpendicular to it [9, 73]. The result of uniaxial stretch is that cells will experience strain and thus stress in a single direction, which can cause various reactions depending on cell type and orientation. With cardiac myocytes, orientation is tied to function and as such being able to control the direction and magnitude in which strain and stress are applied allows for fine control over the cellular response. Many investigators have used modes of uniaxial stretch to test for a variety of myocyte responses including protein turnover, early immediate early genes and Angiotensin II expression [9, 73, 74].

One of the premier models for cell stretch was designed by Vandenburgh and Kaufman in 1979. This model consisted of a fabricated frame that used four screws to apply the stretch, see Figure 7:

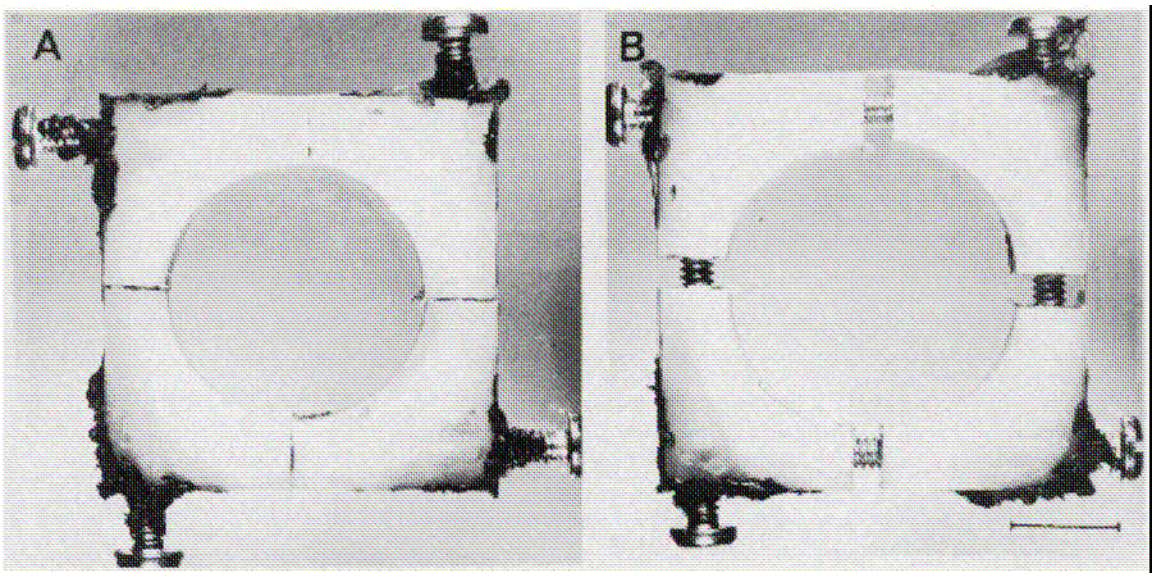

Figure 7. Cell Culture Stretch Frame. Fabricated frame used to apply stretch by adjusting screws to extend the sides. A. Unextended bracket. B. Bracket is extended in two dimensions. [75]

Day 12 embryonic chicken pectoral myoblasts were plated onto a silicone rubber substrate in a well plate that would then be attached to one of the stretch frames. The

myoblasts were allowed to culture before attaching the frame to identify the cell orientation so that strain could be applied along the desired axis of the muscle cells. Each of the four screws would control one direction along one axis. When the screws are extended the pieces of the frame would be pulled apart and apply stretch to the cell culture. Choosing which screws to use will dictate the direction of the stretch applied indicating that this frame can be used for uniaxial or biaxial stretch. In fact, this frame model is used in many subsequent experiments and has been vital to the progression of cardiac mechanic studies. The stretch performed in this experiment was done parallel to the long axis of the myoblasts. The results of this 1979 study showed an average increase in amino acid accumulation by 30% via the radiolabeled amino acid analog a-aminoisobutyric acid (AIB) and an increase in β-MHC production by 14.7% via electrophoresis at 10.8% cell stretch, indicating that this degree of strain is significant to instigate a hypertrophic response [75].

Despite the stretch frame's capability to apply strain in two dimensions, most studies only utilized it in one dimension to simplify the analysis by reducing direction specific factors from interacting. In this respect, most studies focused on stretch applied parallel to the long axis of myocytes as this is the orientation that muscle cells are structurally designed to contract in vivo. As previously mentioned, parallel uniaxial stretch was used to quantitatively link hypertrophic cues to stretch. In addition to β-MHC increase, immediate early gene *c-fos* was shown to increase in expression in direct relation to an increase in the percent strain through a northern blot assay: 5% stretching, 15 ± 5%; 10% stretching, 89 ± 9%; 20% stretching, 100%; mean ± SE., n = 5. In addition these expression levels were found to activate as soon as 15 minutes after being stretched,

showed a maximum expression around 30 minutes and was not seen after 60 minutes [73]. This study demonstrates that parallel stretch activates *c-fos*, which has been shown to be one of several genes that are expressed prior to myocytes expressing a hypertrophic phenotype [7].

These and many other uniaxial stretch experiments have shown just how much a mechanical stimulus can change cellular response and progress maladaptive hypertrophy. However, to get a more broad scope of the full range of mechanical signals that a myocyte will experience in vitro, a multidimensional analysis of these mechanical forces needs to be designed. To emphasize this statement, a study done by Simpson *et al* demonstrates the difference between applying mechanical stretch in the parallel axis versus the perpendicular axis. This study tested the effect of 5% stretch on protein expression in beating myocytes. Cells were cultured in methionine deficient DMEM that was then supplemented with *trans*-labeled [^{35}S] methionine, which would be taken in by cells during protein fabrication. After applying a 5% perpendicular stretch, not only was there a 125% increase in optical density of MHC and a 75% increase in optical density of actin during a SDS-PAGE/laser densitometry test, but also myocyte cultures demonstrated physical damage, as seen in Figure 2 [9]:

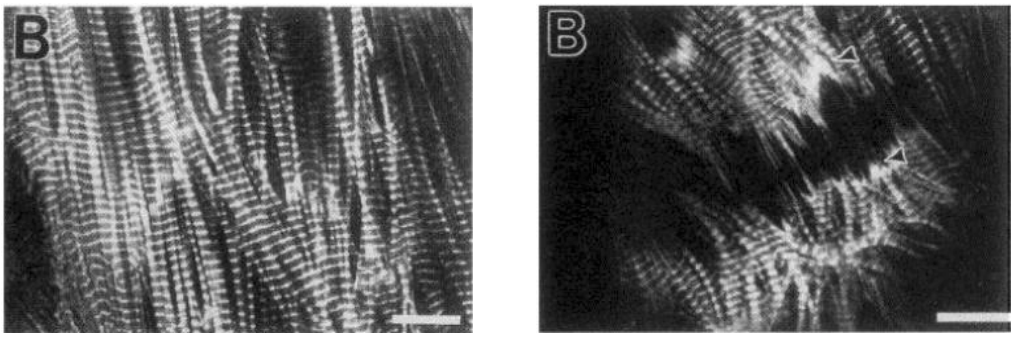

Figure 8 Mechanical damage of perpendicular stetch.
Myocytes that were aligned and stained with phalloidin. Cells were stretched perpendicularly in the right figure showing damage to myocyte's contractile units. [9]

This study emphasizes the importance of directionality in mechanical regulation of myocyte stretch. Even in the previous study utilizing uniaxial stretch, the difference between parallel and perpendicular stretch is apparent. With this in mind, the need to study mechanical regulation of myocytes in a multi-directional model is paramount to accurately define its maladaptive hypertrophic responses.

3.I.B. Multiaxial Stretch Studies

Multiaxial Stretch refers to tests that apply stress along only more than one axis of a two dimensional cell culture surface. Uniaxial studies have helped to elucidate many facets of maladaptive hypertrophy, a few of which were mentioned in the previous section. However, these studies control factors such as cell shape, alignment, cell-cell and cell-ECM adhesion complexes that are not representative of the conditions in vivo. These in vitro cell cultures used in uniaxial tests do not control orientation and are multipolar, while in vivo myocytes are rod-shaped and aligned. In addition to the cells not reflecting the physiologic environment, applying mechanical strains in one direction differs considerably from the multiaxial and anisotropic stretch that myocytes experience in vivo [76]. According to this, the next step in the research would be to begin applying stretch in more than one axis and to develop new devices capable of applying equibiaxial and anisotropic stretch [77].

Applying a uniaxial stretch is relatively simple. By pulling along one axis and keeping the other still, stretch can be applied in one desired direction. The conceptual problem that occurs once multiaxial stretch is applied is that stretch in two simultaneous directions can cause a variety of effects depending on the degree of stretch and the

combinations of directions. Thus, it is necessary to control the stretch in the desired directions so that they are done uniformly.

One of the first experiments to generate a device capable of generating this kind of stretch was done by Lee *et al* [78]. The stretch frame created in this experiment was designed to generate homologous, plane strains and to ensure equibiaxial stretch on a cell culture that is seeded on an elastic silicon membrane. This is accomplished by the rotation of a screwtop lid that compresses on the inner indenter ring of the holder. This compression stretches the membrane, which is clamped to the ring (Figure 9).

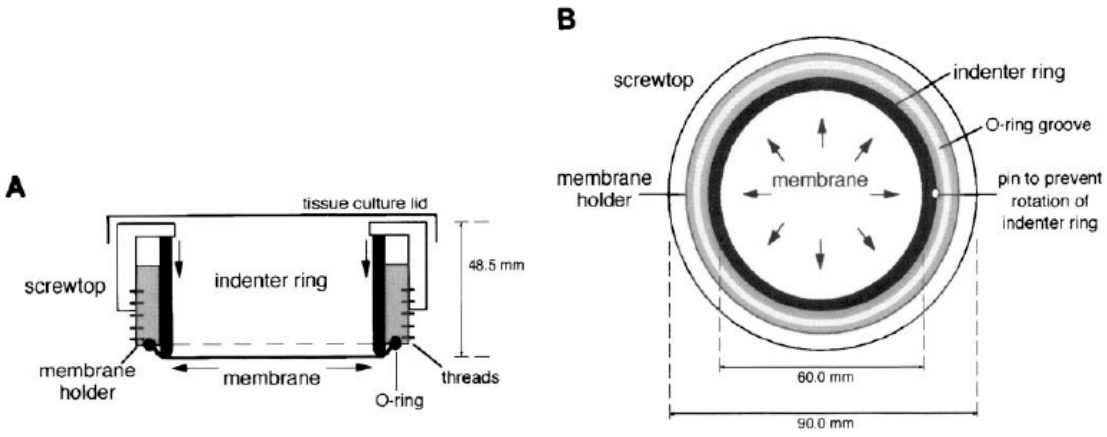

Figure 9: **Equibiaxial stretch device**. Cross-sectional view (A). Top-down view (B) [78].

By using this method to apply stretch, Lee *et al* demonstrated that by tightening the screwtop lid the stretch will be dispersed in the Normal Lagrangian strains in the circumferential and radial axes with relatively zero sheer stretch (0.000 ± 0.003). This indicates that the stretch that the cells feel is truly equibiaxial and directly proportional to the ratio of the vertical displacement (measured by the pitch of the screw thread) to the radius of the elastic membrane.

Many experiments have since used this equibiaxial stretch device, most of which have investigated the response of vascular smooth muscle to specific stretch. However, some studies have investigated the expression of hypertrophic factors in cardiac myocytes and cardiac fibroblasts.

A study done by Leri *et al* utilized Lee's equibiaxial stretch device to test for the up regulation of AT_1 and AT_2 angiotensin II. Load-dependent sarcomere elongation in myocytes has been shown to lead to an increase in cell surface angiotensin II receptors, AT_1 and AT_2 as well as an increase in local Ang II production. By applying a 20% equibiaxial stretch for 3 and 12 hours on myocyte cultures, both from a myocardial infarct model and from a normal myocyte culture, it was observed that cells progressively showed a 2.4x and a 2.3x increase in AT_1 and AT_2, respectively, on the surface of post infarct myocytes as well as a 2.0x and a 1.7x increase in AT_1 and AT_2, respectively, on the surface of normal myocytes. In addition to the increase in angiotensin surface receptors, ang II concentration was shown to be significantly upregulated and demonstrated a 39% and 57% increase in post infarct myocytes at 3 and 12 hours, respectively [79]. The data shown indicates that cells that have been in an infracted environment are more likely to increasing both local ang II expression as well as cell angiotensin receptors, which means that cells that have already undergone mechanical stress are more susceptible to hypertrophy, progression of the dysfunction and total heart failure.

In a more recent study, cardiac fibroblasts were also exposed to 3% and 6% equibiaxial stretch in the presence of radiolabeled [P^{35}] GTP, which are used in the fabrication of G-proteins specific to focal adhesions responsible for mechanical

transduction between fibroblasts and the ECM. Under these conditions, fibroblasts demonstrated a 4.7x increase in the 6% at 6 cycle stretch studies and a 5.5x increase in the 3% at 12 cycle stretch studies. Also, these same cells showed a 2.8x increase in G-Protein synthesis in the presence of Ang II. This study shows that cardiac fibroblasts increase their cellular mechanical connections in the presence of strain and hypertrophic factors. Doing so indicates that these fibroblasts will relay mechanical forces to the ECM, which will increase the environmental stress for the entire tissue [80].

Equibiaxial stretch has shown to be a valuable tool in the study of cardiac dysfunction and maladaptive hypertrophy. Currently, more developments are being made to improve the homogeneity of the applied stretch by using electronic control [81]. Even with these current developments the true nature of the in vivo cardiac mechanical environment remains far more complex than biaxial. There have been some developments in anisotropic stretch, which applies a stretch unevenly across an elastic substrate.

As stated in the beginning of this section, cells in vivo experience irregular and anisotropic stretch and typically not stretch that is limited to one or two dimensions. Thus, another important step in the analysis of mechanical regulation of maladaptive hypertrophy is testing anisotropic stretch, which more closely resembles physiologic stretch. In a study done by Gopalan *et al*, the same equibiaxial stretching device was modified to have an elliptical indenter in lieu of the circular indenter, thus generating an anisotropic stretch profile (Figure 10):

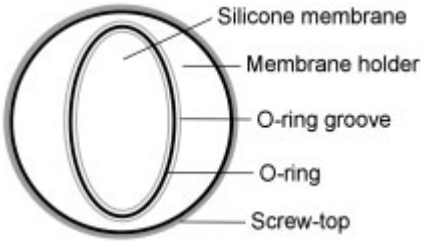

Figure 10. Elliptical shape of polycarbonate indenter ring which generates anisotropic stretch [76].

When this frame is compressed against the silicate elastic membrane, the shorter axis will have a larger amount of stretch than the longer axis. By changing the orientation of cell culture, the different effects of stretch favoring one axis while still supplying stretch along another axis can be examined. In order to change cell orientation, a procedure using photolithographic membranes was used to generate a cell stencil which spatially controls cell deposition. Essentially, a silicon wafer is treated with photoresistant Epon SU8, which is exposed to UV light through a high resolution transparency with a pattern causing the exposed SU8 to solidify in the pattern from the transparency. Once the liquid SU8 is washed away, the remaining pattern is that of the transparency. Polydimethylsiloxane (PDMS) can be spin-coated onto this wafer, cured and removed to generate a high resolution stencil identical to the pattern from the original transparency. PDMS is a bio-inert polymer that cells will not attach to, thus when placed over a coverslip, cells will fall into the stencil and be seeding in the pattern [82]. A resulting cartoon of cells patterned in defined rows on an anisotropic membrane can be seen in Figure 11:

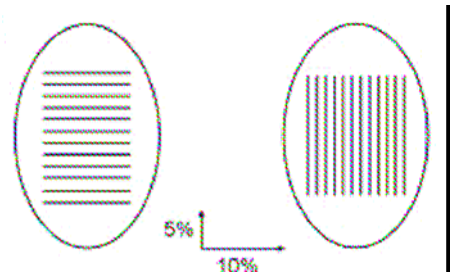

Figure 11. Representation of cells patterned using PDMS stencils on elastic membranes in an anisotropic stretch frame.

where cell cultures were exposed to two profiles of stretch defined by cell orientation to the shape of the indenter frame: cell orientation parallel to the long axis (right) and cell orientation perpendicular to the long axis (left).

The results of this study were demonstrated by staining myocytes for F-Actin, N-Cadherin, Connexin-43 and ANF. The cells that were stretched with their long axis perpendicular to the long axis of the frame (right) exhibited a continuous stain for F-Actin as compared with the normal striations in myocytes indicating an up regulation and loss of specialization of the actin filaments. Also, these cells show a two-fold increase in N-Cadherin and Connexin-43 concentrations and a seven-fold increase in ANF concentrations. This indicates that applying 10% stretch to myocytes perpendicular to the orientation of contraction, cells will begin to express proteins at concentrations that indicate a hypertrophic response [76].

The current trend of research into axial stretch devices has made multiple advances in the investigation of maladaptive cardiac hypertrophy as well as a multitude of other dysfunctions. As one of the earlier forms of testing that involved application of mechanical force, it shows how truly important the progression to develop more in vivo-like systems is. Eventually, these studies will support work that will accurately define the mechanical environment around cardiac myocytes under normal physiologic and

dysfunctional conditions and how these cells respond to such forces. However, another consideration for describing this environment is each cell's contribution to the total environment. We have seen how a cell will respond to external mechanical stimuli by changing its intracellular structure but how do cells regulate the forces they exert in similar mechanical environments. The study of single or small group cardiac myocyte contraction mechanics has been the interest of research for the last thirty years and many techniques have been developed to generate a more accurate model of the forces that mobile and non-mobile cells exert on their environments. Of particular interest for this project are deformable substrate techniques, which is the subject of the following section.

3.II. Deformable Membrane Studies

The concept of a deformable substrate is integral to this project and as such it will be explained in depth. The initial study that developed the concept of using a deformable substrate was Harris *et al*. Prior to this study, researchers were beginning to uncover the acinomyosin cytoskeletal networks that generate tractional migratory forces. This study points out that that we may know how a cell carries out contraction we still do not know the degree of strength cells use during traction. The main difficulty with quantifying cellular traction was that the magnitudes of these forces were too small to measure with the methods at the time such as micromanipulation.

Harris' response was to culture cells on directly on the surface of some elastic material weak enough to be visibly distorted by the small traction forces by which cells crawl. Then, if the elastic properties of the substratum are known or can be measured, the

forces exerted by individual cells can be read out continuously from the distortions they produce in this substrate. Harris concluded that this substrate should be inert to biochemical charge, shrinkage, non-toxic, transparent and should not interfere with any microscopic observations. The chosen material was a silicon rubber created by polymerization of poly-dimethylsiloxane (PDMS) chains. This silicone fluid was placed on a cover-slip, inverted and passed over a low flame Bunsen burner for 2 seconds. In this brief time period the outermost later of PDMS is polymerized and creates a substrate 1µm thick, which is thin enough such that cardiac fibroblasts could apply traction to the surface and creates observable deformations, see Figure 12:

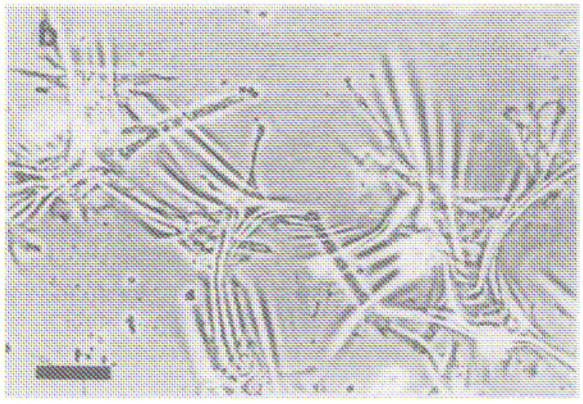

Figure 12. Cardiac fibroblasts seeded onto an elastic silicon membrane generating deformations on the substrate surface [83].

As the cells spread on these surfaces, the cells slowly pull the rubber sheet centripetally past their lower surface, stretching and distorting it enough to produce pronounced wrinkles in the rubber. Fibroblasts on substrates like these are capable of creating deformations up to a millimeter away and once the cells were trypsinized the substrate re-expands to its original shape. It was also reported that initial measurements show that tractions may be in excess of 0.001 dynes/µm, despite not reporting a value for the elastic modulus of the elastic substrates [83]. This study created a very useful tool

with which to quantitatively analyze the mechanical stresses that cells generate under traction or contraction.

In 1994, the method that Harris developed was modified by Lee *et al* in order to generate data that was more easily quantifiable. Poly-dimethylsiloxane was poured into a Rappaport chamber with a glass coverslide sealed to the bottom and allowed to spread evenly. Once the surface was even, Latex beads (~1μm diameter) were applied to the surface using a fine brush after which the silicone rubber was cross-linked using glow discharge. By comparing the placement of beads before and after traction, Lee was able to calculate quantitative force measurements of the tractions generated by fish keraocytes. The analysis was performed by comparing individual beads in their stretched and unstretched position, Figure 13:

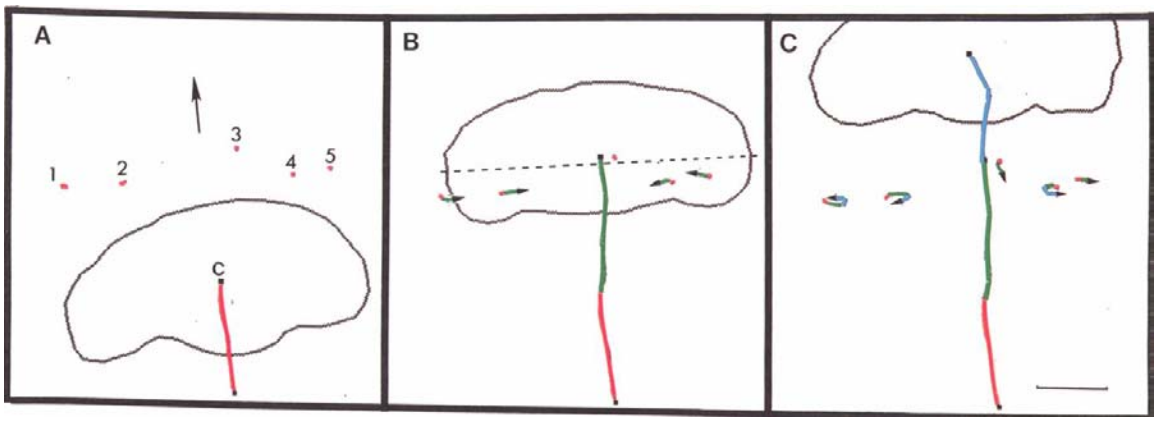

Figure 13. Locomotion of fish keratocyte.
A) Cell motion has no effect on bead movement (red).
B) As cell moves over section with beads, the beads are pulled inward, under the cell (green)
C) The cell moves past the beads and they return to their initial position (blue) [84].

Each image was taken 40s apart. The displacement between each image was measured and using the compliance of each substrate, the stresses at the position of each bead was obtained:

Experiment number	Substratum type	Compliance	Bead #	Maximal displacement	Force
		($\times 10^{-8}$ N/μm)		(μm)	($\times 10^{-8}$ N)
1	Elastic	1.06	1	0.914	0.97
			2	0.750	0.79
			3	1.172	1.24
2	Elastic	1.06	1	0.990	1.05
			2	1.260	1.33
3	Elastic	2.14	1	1.104	2.36
			2	0.762	1.63
4	Elastic	1.26	1	1.459	1.84
5	Hyper-complaint	0.46	1	3.850	1.77
			2	4.430	2.03
			3	2.880	1.32
6	Elastic	0.80*	1	2.930	2.34
			2	2.967	2.37
			3	2.930	2.34

Table 1. Estimation of maximal traction forces. [84]

As seen in Table 1, the displacements and the subsequent traction forces increase as the compliance drops, which is to be expected [84]. This study provides a valuable tool to be used in quantitatively determining tractional cell forces, however the forces determined here are only point forces and do not reflect the continuum of stresses that the cell exerts during traction.

One of the more recent modifications to the elastic substrate method was done in an experiment by Oliver *et al*. In this study, the same method presented in Lee was analyzed using a technique called Traction Density Mapping. Briefly, mapping was done on stiff films so as to produce small, fully recoverable, elastic displacements, which behave in accordance with small strain linear elasticity theory. This allows for the calculation of a distribution of discrete tractions under the cell which give rise to a bead displacement pattern, which are superimposed onto a mesh of the substrate area directly underneath the cell (Figure 14). In concept, Green's stress functions are placed at discrete locations under the cell and varied in direction and magnitude until the observed field of bead displacements is reproduced with maximum accuracy through Bayesian Hypothesis Testing [85, 86]. These processes will be discussed in detail in the following chapter.

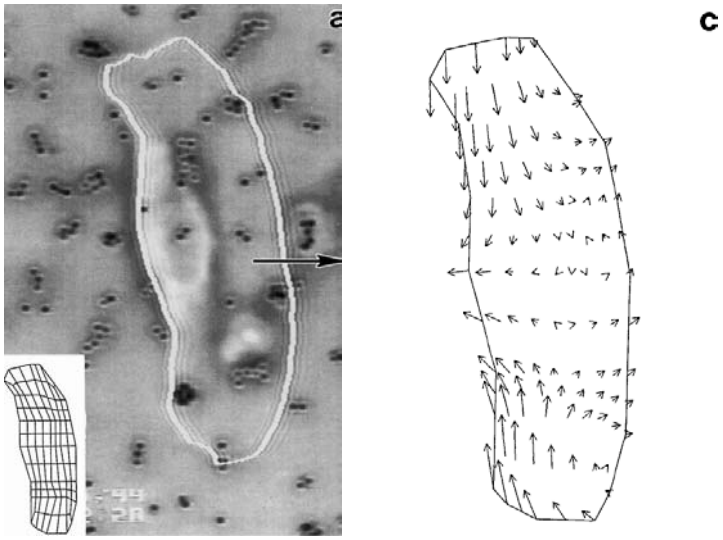

Figure 14. Comparison of actual image of cell migration (left) to the generated traction map (right) [85].

Through studies that over the last twenty years have investigated the interaction between cellular tractional mechanics and maladaptive hypertrophy, many advances have been made in the characterization of cardiac cell mechanics. In addition, the progression of deformable substrate techniques has presented many valuable adaptations that have helped shape a more continuous depiction of cell traction. In the following chapter, a technique developed by Dembo and Wang combines many of the features of the previous deformable substrate techniques with some new alterations which provide for a system that is capable of producing a highly accurate continuous stress maps [71, 87].

Chapter 4: Development of Traction Force Microscopy

As discussed in the previous chapter, new techniques were being aimed at direct force measurement of displacements using deformable substrates [84]. The trends in these studies lead to a definite point where the measurement techniques had become progressively more accurate as the displacement measurement developed from wrinkles to micron-sized fluorescent beads [83, 85]. Despite the increase in the accuracy in the measurements of the substrate's deformation, these displacements are only secondary reflections of the biologically generated tractions. As such, in order to calculate the actual stress forces generated by cells it is necessary to analyze the collected substratum displacements through statistical methods. To accomplish this, Dr Dembo of The University of Boston in correlation with Dr Wang of The University of Massachusetts Medical School incorporated into Traction Force Microscopy the use of Bayesian Hypothesis Testing which defines such traction fields as a distribution of elementary delta functions and then fits the data to find the most likely positions and amplitudes of these elementary sources of stress [71, 87].

Additional modifications from previous techniques include switching from a silicon membrane substrate to a polyacrylamide membrane substrate. The usefulness of this change is that polyacrylamide gels can be controlled for stiffness by adjusting the proportions of monomer and cross-linker during formation. Doing so can produce substrates with defined physical characteristics that are not subject to experimental

factors. Thus, by trial and error, an appropriate form of substrate can be generated specific to the type of cells used in order to create controlled linear deformations while still being able to be detected [88, 89].

With the previous modifications, Traction Force Microscopy moves beyond using the direct substrate deformations as the end result but uses those data in predicting the most statistically likely stress map for the particular cell. In addition, switching from silicon based substratum to polyacrylamide substratum allow for fine control of the physical properties a system that can be tailored to the specific type of cell used. The following section briefly describes Traction Force Microscopy developed by Dembo *et al* [87] and how it was modified for the purposes of the current study. For full details on Traction Force Microscopy, consult Appendix A.

4.I. Overview of Traction Force Microscopy

Traction Force Microscopy utilizes three major processes: the fabrication of the deformable substrate, the image processing using Correlation-Based Optical Flow and Continuum Mechanics, and the verification of the continuous stress field through Bayesian Hypothesis Testing.

Polyacrylamide gels were generated by combining amounts of acrylamide (30% w/v) mixed with *N*, *N*-methylene-bis-acrylamide (2.5% w/v) and distilled H_2O to obtain a final concentration of 10% acrylamide and 0.03% BIS. More rigid or more flexible substrata were generated as the percentage of BIS was increased or decreased, respectively. Fluorescent latex beads (0.2 mm FluoSpheres, carboxylate-modified) were

sonicated briefly in a bath sonicator and added to the acrylamide mixture in volume ratio of 1:125. The gel was added to activated coverslips and sandwiched with an unactivated coverslip to ensure an even surface. This gel sandwich was then inverted to encourage the fluorescent beads to migrate to the "upper" surface of the substrate as the gel solidified. The end result is a deformable acrylamide substrate that has an even layer of fluorescent particles just underneath the cell culture surface. Lastly, to allow cells to attach and live on these gels, type I collagen was attached using a photoactivated linker called sulfo-SANPAH (sulfosuccinimidyl 6 (4-azido-2-nitrophenyl- amino) hexanoate) that binds to the acrylamide surface and type I collagen [87]. The result was a fully characterized substrate embedded with fluorescent particles capable of supporting a cell culture of tractional cells.

3T3 fibroblasts were seeded onto the acrylamide substrates and allowed to attach. In order to generate one stress map, two images must be taken so that the positions of the beads embedded in the gels can be compared. In the current study, this was accomplished using images taken just prior to cells being trypsinized and images taken just after the trypsinization. Doing so will produce images where the substrate is stressed (prior to trypsinization) and images where the substrate is relaxed (after trypsinization). After these images are captured, they are processed to create distribution maps that are representative of the displacements of the fluorescent particles within the substrates.

The generation of finite strain maps is done by processing the pre- and post-trypsinized images. In order to calculate the displacement between the stressed and relaxed images, the process of Correlation-Based Optical Flow was utilized. Briefly, Optical Flow identifies a region of defined intensity in one image and then uses a

correlation function (Equation 1) to compare this region to another of equal size in another image.

$$R(x,y,u,v,C) = \frac{\sum_{\delta_x}\sum_{\delta_y} P_0(x+\delta_x, y+\delta_y) P_1(u+\delta_x, v+\delta_y)}{(\sum_{\delta_x}\sum_{\delta_y} P_0^2(x+\delta_x, y+\delta_y))^{1/2} (\sum\sum P_1^2(u+\delta_x, v+\delta_y))^{1/2}} \quad \text{Eq1}$$

Equation 1 compares specific intensity values of each of the desired Images. The result is a value *R* that ranges from -1 to +1. The closer *R* is to +1, the greater the likelihood that the first region has moved to the position of the second region. By comparing the positions of the two regions and processing the data, a displacement map can be generated that identifies the strains between the stressed and relaxed images, as seen in Figure 15:

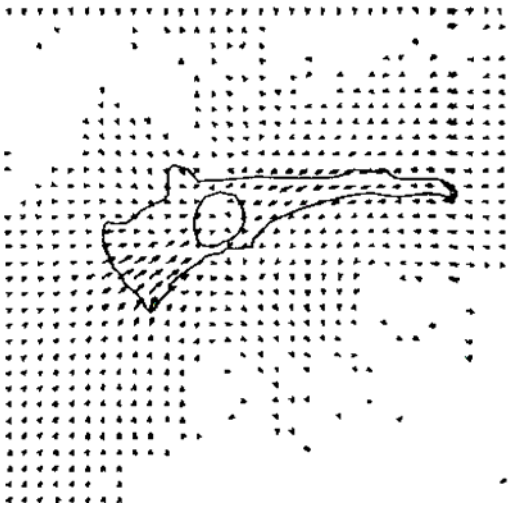

Figure 15. Displacement map of a locomoting 3T3 fibroblast.
The displacement map generated through correlation-based optical flow of a fibroblast applying traction during locomotion on a deformable substrate [90].

After processing the fluorescent images taken of the polyacrylamide deformable substrate by using Correlation-Based Optical Flow, the resulting displacements are then used to predict the stress map that most closely reflects the given displacements. In order

to do so, it must first be realized that the displacements generated through optical flow are measurements of the observed strains in the fluorescent images can generate many possible stress maps. The displacement maps are finite, point maps and as such there are numerous possible continuous stress fields that could be calculated. As such, converting the displacement map to a stress map will not necessarily be the most accurate. Thus, in order to find the most accurate stress map that corresponds best to the measured displacements, statistical methods must be employed to match the measured displacement map values to test displacement values that have been calculated from potential stress maps. Stress maps needed for this process must first be generated through classical continuum mechanics and then test displacement maps are calculated and compared to the measured correlation displacement maps using Bayesian Hypothesis Testing [71, 87].

Key assumptions in these calculations were considered prior to any calculations. First, the substrate was assumed to be an infinitely flat membrane composed of a uniform isotropic elastic material with the center of the membrane coincident with the plane, $x_3 = 0$. Supposing that the only external loads acting on the membrane consist of tangential tractions on the top surface, the dimensionality of the problem is reduced by invoking a standard plane stress approximation. Another key point to make note of was that the thickness of the gel makes an impression on the stress distribution in the vertical dimension and the degree of polymer cross-linking in the polyacrylamide gel. Mechanical compensations will be made, however this fact drastically affected the test displacement maps as the correlation generated displacement maps were a reflection of plane stress and not taking this into account will result in a poor statistical analysis and inappropriate stress approximations [71].

Briefly, by using Equation 2, test continuous stress images were generated that had a high likelihood of representing the finite displacement maps generated with Correlation-Based Optical Flow.

$$\mathbf{T}(\mathbf{f}) = \sum_{k=1}^{N} \mathbf{w}^k \left(S^k(\mathbf{f}) - \frac{A^k}{A_T} \right), \mathbf{f} \in \Omega \qquad \text{Eq2}$$

These test images were then converted into test displacement maps using Equation 3:

$$d_\alpha(\mathbf{x}) = \frac{1}{E_s} \iint [g_{\alpha 1}(\mathbf{x},\mathbf{f}) T_1(\mathbf{f}) + g_{\alpha 2}(\mathbf{x},\mathbf{f}) T_2(\mathbf{f})] d\mathbf{f} \qquad \text{Eq3}$$

where, g is Green's function. Equation 2 produces traction fields $\mathbf{T}(\mathbf{f})$ based on Shape functions and uses them in Equation 3 to produce test displacement data $d_\alpha(\mathbf{x})$. A system of these test displacement maps were generated and then tested against the finite displacement map generated by the Optical Flow [87].

Hypothesis testing is a statistical method used to predict the likelihood that a certain value or set of values will generate a desired result, assuming that the desired result is the correct result [91]. In the case of this experiment, hypothesis testing was performed to assess the likelihood that the continuous displacement fields generated through continuum mechanics and finite element analysis were identical to the finite displacement fields generated through image analysis through correlation-based optical flow. This method will take a myriad of continuous displacement maps generated through Equation 2 and find the one map that has the highest probability of generating the finite displacement map using Equation 3:

$$P(H \mid X) = P(X \mid H) P(H) S_x^{-1}. \qquad \text{Eq4}$$

where

$$P(X \mid H) \propto \exp(-\mathrm{X}^2) \quad \text{Eq5}$$

and

$$P(H) \propto \exp(-\zeta^2) \quad \text{Eq6}$$

In Equation 4, X^2 is the familiar chi-squared statistic and ζ^2 is the complexity of the system.

After the best match is found, it can be decisively concluded that the stress map with the highest probability is the best representation of the traction applied by the locomoting fibroblast onto its substrate [71, 87].

Traction Force Microscopy as defined by Dembo and Wang is a powerful tool. By building off older mechanical studies and modifying those using polyacrylamide gels, fluorescent beads, Correlation-Based Optical Flow, Finite Element Analysis and Bayesian Hypothesis Testing, Traction Force Microscopy is capable of creating an accurate representation of the tractions that cells exert during locomotion or during any other actions that generate stresses. After being published in 1999, Traction Force Microscopy has been referenced and applied to many other applications including but not limited to actin cytoskeleton remodeling, tumor cell mechanics and cardiac mechanics [92-94].

For the purposes of the current study, Traction Force Microscopy was used to develop a tool capable of characterizing the mechanical environment of cells with the potential of fine control over cell position and gauging cell mechanical responses to defined biologic and chemical cues. The details of this system for the purpose of this

study and will be outlined in the following section and bring together topics from the previous chapters on maladaptive cardiac hypertrophy and mechanical traction analysis.

4.II. Refining of Traction Force Microscopy

Based on the previous discussions, techniques are always being modified and created to produce a mechanical analysis tool capable of generating results that would better mimic the mechanical environments in vivo. This progression is fueled by the need to have a system capable of reproducing mechanical environments before, during and after a dysfunctional event in order to fully characterize the causes and prevent any permanent damage. The current study proposes a system capable of providing quantitative measurements of the cellular environment while concurrently allowing the same environment to be spatially controlled through collagen deposition and alignment. In this section, the details of our system will be outlined as well as the main areas of modification: polyacrylamide gel preparation and traction force analysis.

First it must be clarified that this system is capable of being used with various cell types for the purpose of mechanical study. Any cell capable of forming mechanical interfaces can be used in this system provided that the proper linking molecule is present on the surface of the polyacrylamide gel. Also, using techniques that will be discussed in the appendices allow for fine control of cell position using Laser Micropatterning and protein deposition techniques [95-98]. For the purposes of the current discussion the cell environment will be conducive for cardiac myocytes in the study of maladaptive

hypertrophy through quantitative identification of the mechanical environment during contraction.

Understanding the contractile mechanism in under both normal and dysfunctional as discussed in Chapter 2 is a complex undertaking. Of particular interest with maladaptive hypertrophy is the mechanical effect that cardiac myocytes create either in response to other mechanical cues they may receive from other myocytes or biological cues from other cells or the ECM. We feel that an important step in understanding the progression of maladaptive hypertrophy is to gauge the mechanical reactions of cardiac myocytes to their environment. Thus, the current modified traction force microscopy was designed to focus on creating controlled environments capable of being quantitatively analyzed for the purpose of understanding the mechanical nature of hypertrophy.

Our procedure is outlined as follows. First, polyacrylamide substrates were generated with specific defined physical properties including a Young's modulus of 75kPa, 30kPa or 7kPa as defined by the protocol and tested using AFM compression testing (Results in Section 6.I). These gels were fabricated using a protocol similar to the one outlined in 4.I with modifications that are the subject of the following section. Briefly, these gels were created with one of the previously mentioned stiffnesses. The surface of these gels had collagen I bound to the surface in either a random orientation or an aligned orientation. Examples of myocytes seeded onto aligned and unaligned collagen can be seen in Figures 16 and 17. Having aligned collagen provided the cells with ECM contacts that more closely mimic in vivo protein layouts and helped to provide a normal physiologic response. By seeding cardiac myocytes onto gels with these varying stiffnesses and varying collagen alignment six distinct environments were created for the

cells to interact with. It was our expectation that myocytes would respond differently to each of these environments and that their mechanical responses will reflect the biologic adaptation as the myocytes initiate a hypertrophic response. By taking fluorescent bead images of the substrates of these gels, we created representative stress maps illustrating

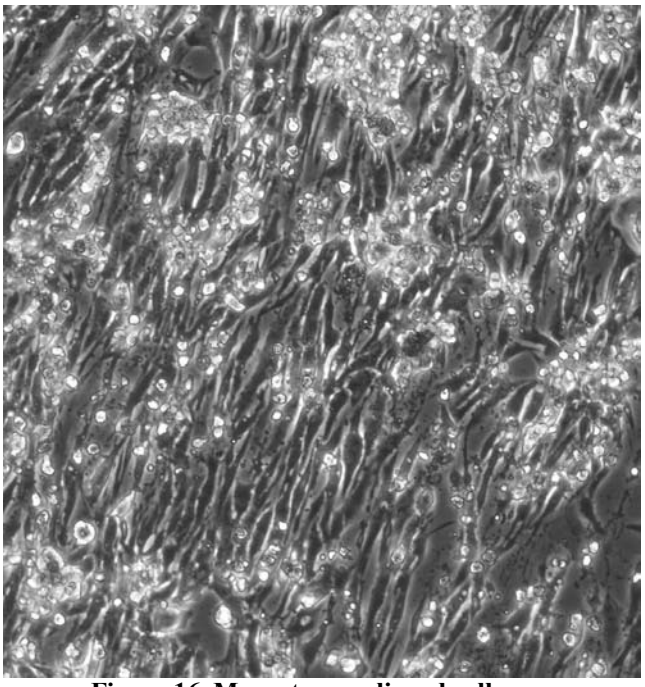

Figure 16. Myocytes on aligned collagen.
10x image of day 3 neonatal myocytes seeded onto an acrylamide gel with aligned collagen.

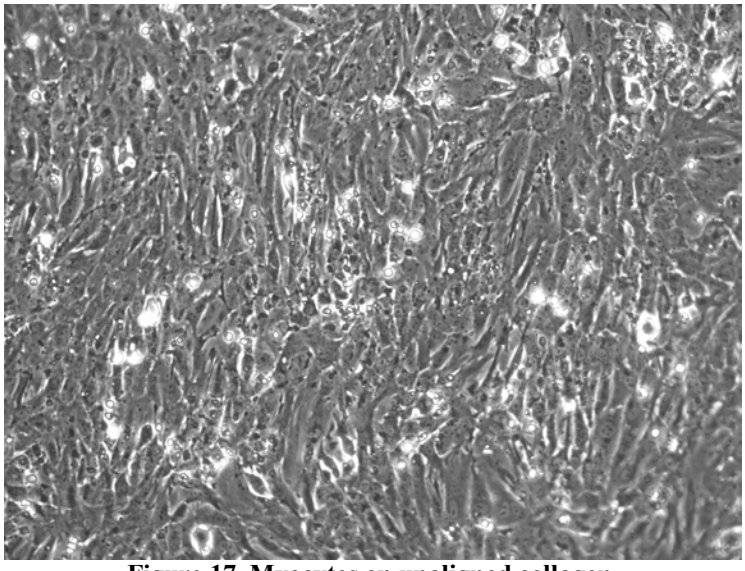

Figure 17. Myocytes on unaligned collagen.
10x image of day 3 neonatal myocytes seeded onto an acrylamide gel with unaligned collagen.

the mechanical responses of these cells as well as generated quantitative measurements of these stresses. It is our goal to demonstrate that progressively less in vivo like stress maps are generated as the gels also become less in vivo like, characterized by lower stiffness and unaligned collagen. That is to say, we predicted that as the gels become less stiff and less aligned, the cells will cease to create the typical end-to-end contractile force distributions and will begin to show anisotropic contractions as cell morphology changes to the hypertrophic phenotype. Other considerations dealing with modifications made with the traction force analysis will be outlined in the following sections.

4.II.A. Acrylamide Modifications

For a full outline of the modified protocol used for creating polyacrylamide gels in this study please refer to section 5.II. In order to accommodate to the needs of the current study, modifications to the previous acrylamide gel protocol summarized in section 4.I (and detailed in Appendix A) needed to be made: the timing and method of introducing the fluorescent microspheres, the concentration and composition of the collagen mixture and aligning the collagen on the gel. In this section each of these modifications will be described and their benefits shown.

One modification that had a large effect on how the images were processed was changing how the fluorescent beads were introduced to the acrylamide gels. In the previous protocol, during the mixing of acrylamide monomer, bis-acrylamide and 1M Hepes the 0.2μm rhodamine fluorescent beads were added at a concentration of 1:100 beads to 50mM Hepes. The solution was mixed together and after the initiator and catalyst were added the gel was sandwiched with another coverslip to flatten the gel and

the whole unit is flipped such that gravity will pull the beads towards the cell surface while the gel is polymerizing. This is done because out-of-plane beads will not be in focus and will generate artifacts that may not be subject to the same traction forces as the beads on the surface plane. The result of such a situation is a high level of noise in the images which translates to error during generation of displacement maps (as seen in Figure 147 in section 5 of Appendix A). However, problems occured with this procedure as the rate of polymerization varies between acrylamide mixtures and as such, the concentration of beads in focal planes of the fluorescent images cannot be assured, resulting in errors. An example of a gel with out-of-plane beads can be seen in Figure 18:

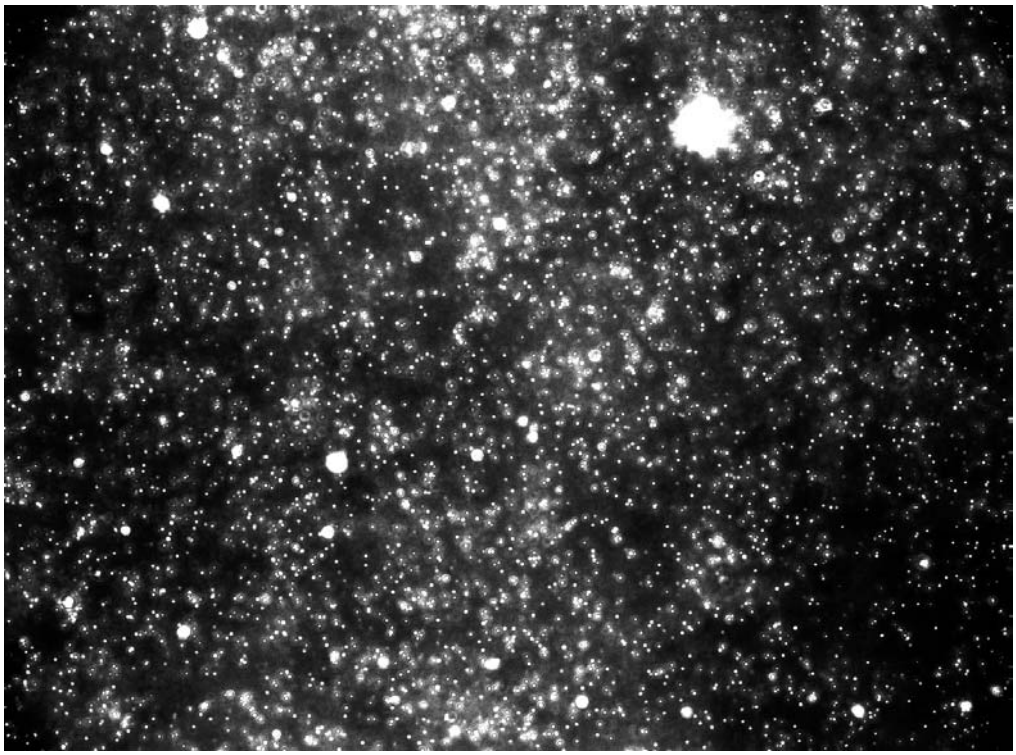

Figure 18. Image of fluorescent beads containing out-of-plane beads.
In this figure, out-of-plane beads generate image artifacts that make sections blurry and hold potential to introduce error. Bead concentration of 1:200.

In order to incorporate the fluorescent beads in a way that did not introduce this error, we introduced the beads after the acrylamide gel was polymerized. This was done by making a mixture of the fluorescent beads and 50mM Hepes and coating the gel

overnight at 4ºC. The result was a smooth layer of fluorescent beads that was limited to one focal plane (Figure 19). As seen in Figure 19, the image is smoother, containing little to no out-of-plane error artifacts which made generating image intensity profiles more accurate during optical flow processing. With the reduced error from covering the gels with the bead solution, it was possible and desirable to increase the bead concentration resulting in a denser bead image with maintained resolution due to the absence of out-of-plane errors. In the current study, the bead solution used on all gels was increased to 1:10 of beads to 50mM Hepes.

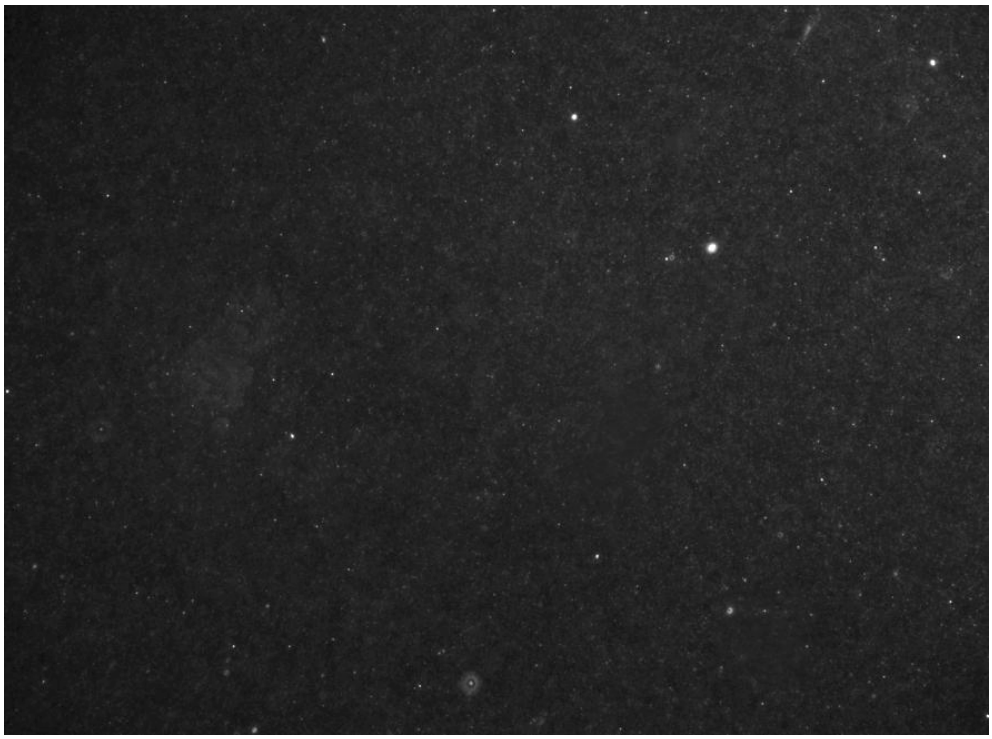

Figure 19. Image of fluorescent beads containing little to no out-of-plane beads.
In this image, out-of-plane beads are minimized and accuracy of calculations and resolution are improved. Bead concentration of 1:10.

The next gel modification made for the purposes of this study was a change in the collagen concentration. In the previous protocol, the concentration of collagen that was bonded to the acrylamide gel was 0.2 mg/mL. This concentration was acceptable for robust cells such as fibroblasts but not suggested for cardiac myocytes which required a

denser collagen matrix [99-101]. As suggested in the referred studies, a collagen concentration that is more supportive of cardiac myocytes is 2.9 mg/mL, which was the concentration used in this study. This increased collagen solution was made using one part 1x MEM, one part 0.2M Hepes and eight parts Vitrogen 100 collagen (3mg/mL). In previous experiments, changing the collagen concentration from 0.2 mg/mL to 2.9 mg/mL drastically improved cardiac myocyte viability.

The last gel modification was aligning the collagen. Many previous studies have shown the importance of aligning collagen for the purpose of creating a more in vivo like environment [32, 102, 103]. Cardiac myocytes align themselves using collagen fibers in vivo making aligned collagen the natural choice for generating an in vivo like environment. Doing so also improves cell function and viability for reasons discussed in Chapter 2 including regulation of normal cell processes like contractile orientation and normal cell phenotype. A popular method of producing regions of aligned collagen has been to use a cell scraper to slowly allow a collagen solution to flow down a cell culture dish. This process becomes tedious when using acrylamide gels as the lower stiffness gels were extremely sensitive to the pressure and drag of moving a cell scraper across the surface making this method undesirable for the current study. Another successful method of aligning cells has been to use photolithographic stencils to restrict cell attachment area (Figure 20).

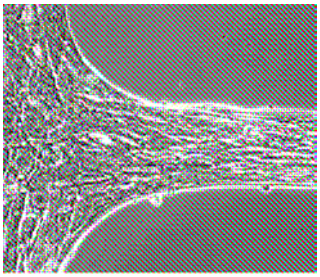

Figure 20. Cardiac myocytes patterned using a photolithographic stencil [96]

One problem with this process was that the stencil would not align the collagen but only impose an orientation on the cells. As such the connections between the cells and collagen do not support the cell's orientation as the collagen was uncontrolled relative to the cell alignment. Another problem with this process was that in order to keep cells in the stencil during attachment, the stencil needed to be flush with the surface of the gel. Because of the pressure exerted to keep the stencil down, the removal of the stencil resulted in the acrylamide gel becoming attached and be pulled up as well. Thus, for the current study collagen was applied by dipping the edge of a #1 coverslip (~0.15mm) in a collagen solution. This edge is then dabbed on the bottom of a cell culture dish to remove excessive collagen and then the edge is pressed slowly from on side of the coverslip edge to the other. This process allowed for the generation of many striations of collagen on each gel and cells align on these striations in the direction in which the edge was pressed (Figure 21).

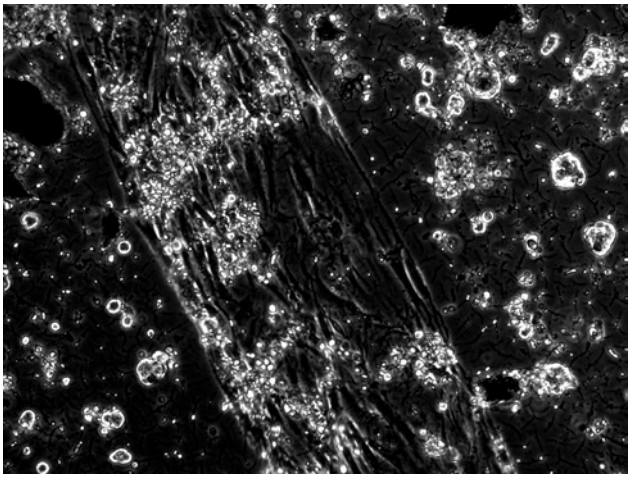

Figure 21. Cardiac myocytes aligned with coverslip edge

With the previous modifications to the polyacrylamide gel protocol the fluorescent images taken are more resolute containing fewer errors, the collagen concentration is more conducive for cardiac myocyte culture and collagen alignment produces a more in

vivo like environment for a more physiologic cell culture. In addition to these modifications, changes in the traction force analysis also permit the analysis of cardiac myocyte contraction.

4.II.B. Traction Force Modifications

The method used in this research to generate stress and strain maps utilizes techniques discussed previously by Dembo *et al* [71, 87] as well as a dynamic simulation technique based on molecular dynamics. Molecular Dynamics (MD) is a powerful simulation tool used to study the physical and chemical properties of solids, liquids, amorphous materials and biological molecules. MD is based on Newton's laws and focuses on bulk properties, which do not depend on quantum level behaviors. Classic applications of MD are done to predict the collisions of gas particles, and when done with individual gas particles are relatively simple; however, solving simple Newtonian equations for 10^{23} particles becomes arduous. When the mass of these particles are known, their net force imposed on these particles can be determined using Newton's second law:

$$m\frac{d^2\mathbf{r}_i}{dt^2} = F_i(\mathbf{r}_0,...,\mathbf{r}_{N-1}) \qquad \text{Eq7.}$$

Also, we assume that the force on molecule i is derived from a sum of central molecule-molecule potential:

$$\mathbf{f}_{ij} = -\frac{du(r_{ij})}{dr_{ij}} \qquad \text{Eq8}$$

where $r_{ij} = |\ \mathbf{r}_i - \mathbf{r}_j\ | = r_{ji}$ is the distance between the centers of molecules i and j. When this system is allowed to react and impose elastic forces onto other particles, the particles

will undergo displacement until their energy dissipates and they approach rest as their net forces $\mathbf{f}_{ij}$ approach zero. As the system progresses, the energy is released into the surroundings and the forces diminish until the particles approach their final positions at a defined time point, which can be measured and the final displacement of particles can be determined [104]. In order to use MD in our application we need to assume that each particle can only be affected by its adjacent neighboring particles along the *x, y* and *z* directions. Also, we need to assume that our material is isotropic and that forces are exerted evenly along the substrate.

A brief summary of our dynamic simulation technique is as follows. A time lapse series of images were taken of myocytes undergoing contraction on an acrylamide substrate with defined physical properties. Two consecutive images in these series were analyzed using a Correlation-Based Optical Flow system similar to Marganski *et al* [90] , which generated a finite displacement map and data for the motion between the chosen images (Figure 22).

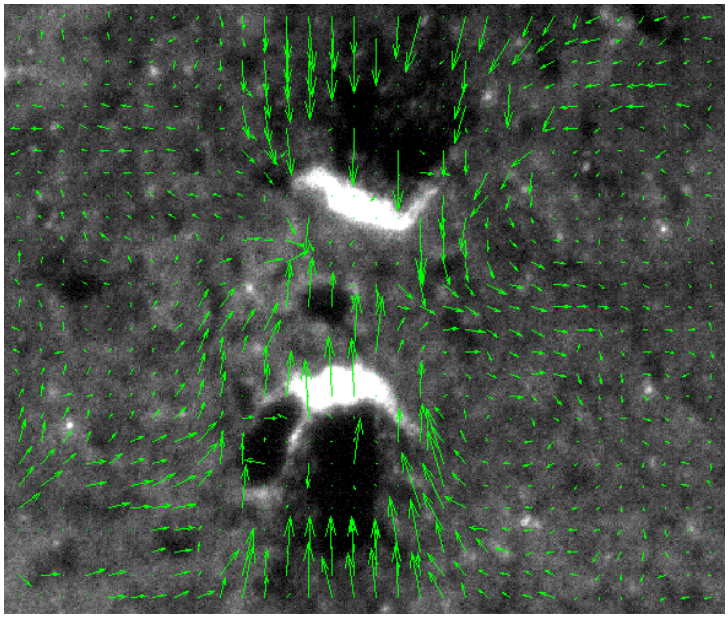

Figure 22. Displacement map generated through Optical Flow

Instead of using these Optical Flow data as a comparison for the most likely continuous stress field as in Dembo *et al* [71, 87], our technique created a dynamic simulation where we used the Optical Flow data to recreate the displacements caused by myocyte contraction. Consider the acrylamide substrate consisting of finite elements in three dimensions as seen in figure 23:

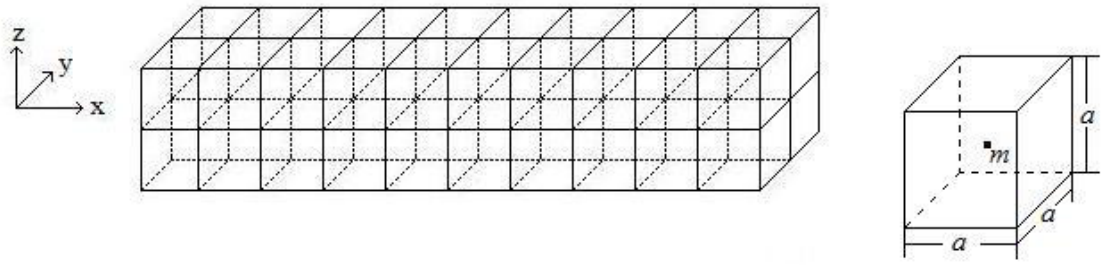

Figure 23. Acrylamide substrate divided into finite elements

where each element is of a size $a \times a \times a$. In order to simplify the assumptions for these calculations, we assume that the mass *m* of each element is represented at a single point at the center of each element. This assumption reduces the complexity of these calculations significantly; however it also excludes the continuous strains imposed along the entire element and is discussed later in Appendix A.

The interaction between the node-*i* and node-*j* can be described by the following relation,

$$F_{ij} = -\frac{E \cdot a}{1-2\nu}(S_{ij} - a), \qquad \text{Eq9}$$

where *E* is Young's Modulus and *v* is Poisson's Ratio, obtained from the gel's physical properties, and S_{ij} is the distance between the two nodes [105]. Basing on Eq.6, we use classic dynamic simulation to calculate the system status of the node-discretized substrate (Figure 23). Using the dynamic simulation, we can obtain the equilibrium state of the

system after the surface traction exerted by the cells. During the calculation, only the neighboring interactions were considered.

First, we discretized the substrate in equilibrium state into particle nodes of specific mass, then imposed position data onto the top layer. In the current research, the substrate was divided into 10 layers in the z-direction (layer 0 – layer 9) and then we set the initial positions of layer 9 to those positions obtained from the Optical Flow technique. During the calculation, the displacements of the nodes in layer-9 were locked causing the system to be under stress which was released during the dynamic simulation. At the boundary layers in x and y direction, the energy of the system released from the stress was adsorbed by setting the velocities of the nodes to zero after each simulation step, until the system arrived at the equilibrium state. Here the system is considered to be arriving equilibrium state when the long time average of the force exerted on a single node is smaller than 10^{-14}N. We calculated the Cauchy stress based on the structure information of the substrate obtained from its equilibrium state. Using the method described above, we were able to create a three dimensional stress map for the substrate at a defined z layer. These stress figures as well as relative magnitudes are recorded for cell patters on 75 kPa, 30 kPa and 7 kPa acrylamide gels in both a random and aligned cell orientation.

Chapter 5: Experimental Procedure

5.I Cell Culture Technique

For full dissection protocol see Appendix C. Briefly, cardiac myocytes are harvested from day three neonatal Sprague-Dawley rats. Hearts were extracted, progressively digested using Collagenase type 1 (120 units/mL) and filtered with a 0.22μm filter to remove clumps of ECM tissue remaining. Cell suspension was collected and allowed to sit in a T75 flask for 30 minutes. In this time fibroblasts will adhere but cardiac myocytes will not, thus by collecting the media off the flask the cell suspension will be mostly myocytes. Fibroblast media is then added to the flask and it is stored in at 37ºC and 5% CO_2. The myocyte rich cell suspension is then filtered using percoll gradients, which contain three density layers (1.06 g/mL, 1.08 g/mL and 1.10 g/mL) with the heaviest on the bottom and then the less dense layers are added on top. By adding 1 mL of myocyte rich suspension to each gradient and centrifuging at 2000 rpm for 20 minutes, the cell types are separated as fibroblasts are larger than myocytes which are yet larger than platelets and red blood cells. The result is a gradient with three distinct bands of cells. From this point, the myocyte layer can be extracted, counted and seeded onto substrates. Myocytes are kept in Myocyte media and fibroblasts are kept in Fibroblast media both described in Appendix B. Media was changed the first day after dissection and then every other day. For myocyte cultures, 3-4 days were allowed for the cells to adhere, align to the substrate and express contraction.

After being imaged for traction force analysis, cells were stained for either F-Actin or Connexin 43. Both stains were limited to FITC (475nm-490nm excitation; 515 emission) due to the fluorescent beads fluorescing using a Rhodamine stain (570 excitation, 590 emission). Confocal images of stained cells were taken on all three gel stiffnesses and either aligned or unaligned. Procedure for taking fluorescent stained images is detailed in Section 5.III.

5.II. Polyacrylamide Gel Preparation

For full gel protocol see Appendix B. A 22 x 22 #1 glass coverslips are cleaned using 0.1M NaOH. The coverslips are washed and then are covered with 3-aminopropyltrimethoxy silane and allowed to sit for 5 minutes. It is important to fully wash the coverslips with distilled water after this 5 minute period as the silane and gluteraldehyde in the following steps combine to form a toxic yellow substance that will kill any cells seeded onto that coverslip. As such, the coverslips are rinsed with water and then put into a container filled with distilled water and placed on a shaker for 15 minutes. The coverslips are shaken three times for 15 minutes to ensure that all the free silane is removed. After this time, the coverslips are completely dried and 0.5% gluteraldehyde is added to cover the entire surface and allowed to sit for 30 minutes. After this time, the coverslips are rinsed and shaken in water again for 15 minute intervals and completely dried. After this step, the coverslips are able to bind to polyacrylamide through a gluteraldehyde linkage. Preparation of the polyacrylamide gel solution is done according to Table 2:

Final Acryl/Bis	40%Acrylamide	2%Bis	1M HEPES	H_20	Young's Modulus
8%/0.1%	1000 ul	250 ul	50 ul	3700 ul	?? kN/m2
8/0.08	1000	200	50	3750	75
8/0.06	1000	150	50	3800	30
8/0.05	1000	125	50	3825	23
8/0.04	1000	100	50	3850	17
8/0.03	1000	75	50	3875	14
8/0.02	1000	50	50	3900	10
5/0.12	625	300	50	4025	33
5/0.10	625	250	50	4075	28
5/0.08	625	200	50	4125	24
5/0.06	625	150	50	4175	15
5/0.025	625	63	50	4262	7

Table 2. Acrylamide preparation and corresponding Young's Modulus

Each gel solution consists of acrylamide monomer (40% Acrylamide, Bio Rad) bis acrylamide (2% Bis Acrylamide, Bio Rad) and 1M Hepes. By combining these components at differing concentrations, different stiffnesses can be achieved. The three stiffnessess used for this study are 75kPa, 30kPa and 7kPa. The monomer, bis and Hepes are added first and this solution is degassed in a vacuum to remove excess air present. This is done as air bubbles may form in the gel during polymerization and result in surface irregularities. After being degassed, the solutions have distilled water added to bring the volume to 5 mL. At this point, 30 µL of the activator ammonium persulfate (0.1 mg/mL) is added. After this step 20 µL of the catalyst TEMED (Bio Rad) is added and then 20 µL of the solution is place in the center of each coverslip and is sandwiched using another 22 x 22 #1 coverslip in order to spread the acrylamide and ensure an even surface. To ensure that all of acrylamide on the activated coverslip has polymerized, check to see if the remaining acrylamide solution has polymerized. Once it has, cover the coverslip with 50mM Hepes and gently remove the top coverslip. The next step is to add a 1:10 solution of 0.2µm rhodamine fluorescent beads to the coverslips. This solution is

kept on the coverslips overnight at 4ºC. After this time, the bead solution is washed off carefully and the gels can be stored in 50mM Hepes for up to 2 weeks.

The acrylamide gels have polymerized but are not capable of binding collagen for cell attachment. In order to do so, the gels are treated with a solution of 0.5 mg/ml sulfo-SANPAH. When activated this solution will bind to the gel and provide a disulfide linkage for collagen to attach to. Sulfo-SANPAH is light activated and is handled in the dark. Each gel is covered with sulfo-SANPAH and exposed to UV light for 6 minutes and then rinsed with 50mM Hepes. This step is done twice before adding collagen. A collagen mixture is made 1:1:8 of 0.2M Hepes, 1x MEM and Vitrogen 100 Collagen type I. The collagen mixture is put in a 35mm cell culture dish and spread out. A #1 coverslip is taken and the thin edge is dipped in the collagen mixture. Excess collagen is wiped off and the thin edge is pressed on the gel, top first and slowly rolled down to induce an orientation of the collagen column. The gel is then tilted along the orientation of the collagen columns and placed in 4ºC overnight. After this time, the coverslips are washes in 50 mM Hepes and exposed to UV light for 15 minutes in order to ensure all the acrylamide is polymerized and to ensure that no exposed sulfo-SANPAH will harm the cells. The Hepes is washed and myocyte media is added to the coverslips and they are placed at 37ºC and 5% CO_2 for an hour to allow the media to enter into the gel and warm up the surface for cell attachment.

5.III. Imaging

All images were taken on a Zeiss Axiovert 200M inverted light microscope. The microscope is fit with an XL-3 on-stage incubator. The incubator generates a constant

37ºC temperature and 5% CO_2 for extended imaging without exposing the cells to an unfavorable environment. Images were taken using the following: Zeiss A-Plan 10x (*NA* = 0.25), Zeiss Plan-Neofluar 40x oil immersion (*NA* = 0.75), Zeiss Achroplan 40x long distance (*NA* = 0.65) and an AxioCam HS (High speed) CCD camera. Confocal fluorescent images of stained cells were taken on a Zeiss LSM510 Laser Confocal Microscope using a Cobalt laser. Pre-traction image processing was done with Zeiss AxioVision image processing software.

The process for taking fluorescent bead images is as follows. Dishes containing cells were placed in the on-stage incubator such that the collagen columns were vertical in the field of view. A region with well defined bead intensity is found that overlaps with contracting myocytes. Still images were taken at 10x, and 40x using both phase and rhodamine filters with minimum exposure time (typically ~0 ms) to ensure the fastest image rate (maximum of 200 fps). Time lapse images were taken at 40x using a rhodamine filter with an exposure of 0ms for 10sec per batch. These time lapse images were individually processed through adjustment of histogram intensities to filter out the necessary bead intensities from unnecessary noise. At this point, images were saved for traction force analysis.

5.IV. Generation of Stress Maps

Traction stress maps were created by choosing two images at a time from time lapse sets. These two images are then input to a program that uses Optical Flow to generate a displacement image as well as two output files containing the displacement between the chosen images (Figure 24).

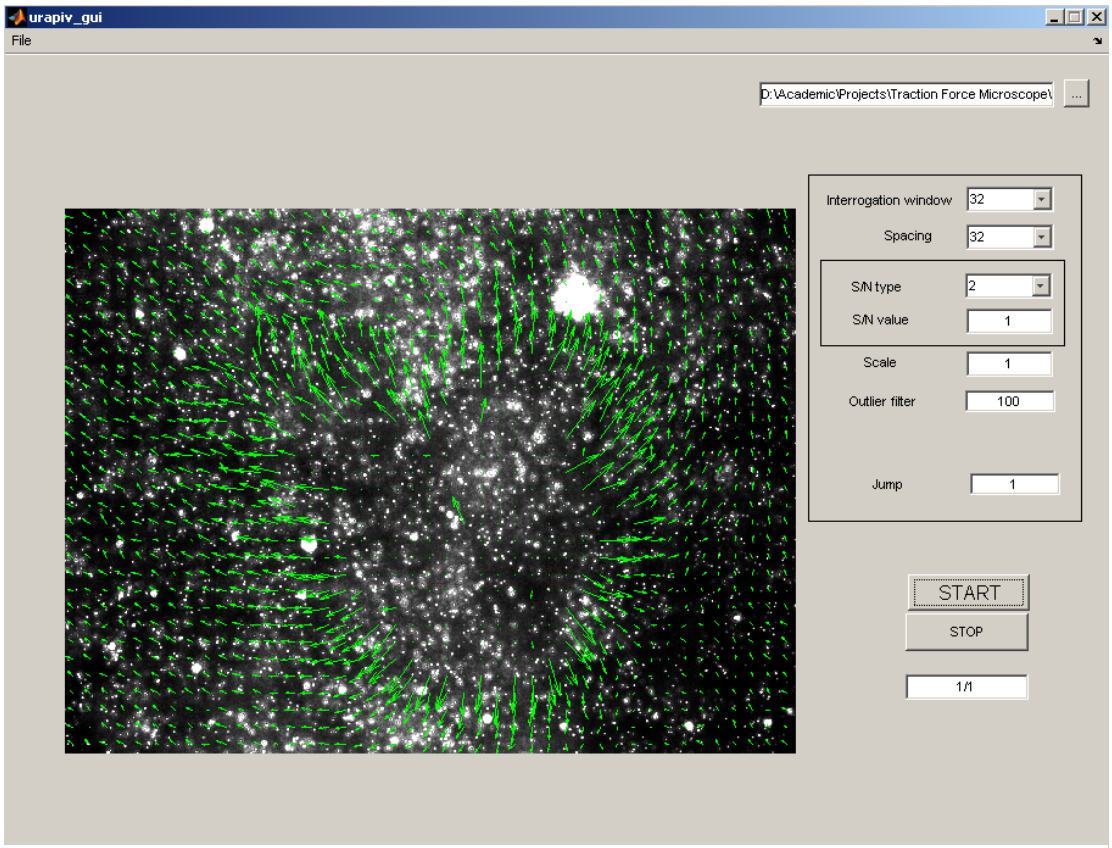

Figure 24. Image of the GUI for the Optical Flow program

In this program, we can define the size of the interrogation window as well as the spacing between nodes. Adjusting the interrogation size will affect how sure we are of the final displacements but resulting in an increased processing time. Similarly, by changing the distance between nodes, we can generate a more dense displacement map but again at a cost of processing time. The output files contain all of the displacement data for the two chosen images.

Next, we used a program that defines the substrate mechanics according to Section 4.II.B. This program takes in the Optical Flow data and sets it to the surface layer of the simulated substrate. Prior to processing, we input values for the element size

(determined in the Optical Flow program), the number of layers in the simulated substrate, the pixel size, the simulated mass of each node, Young's Modulus, Poisson's Ratio, the minimum force prior to equilibrium and the simulated time between data sampling. The outputs are data files containing the final equilibrium displacements for each node in the *x, y,* and *z* directions.

Next we isolated the data we needed by selecting the desired plane of the substrate, illustrated in Figure 25.

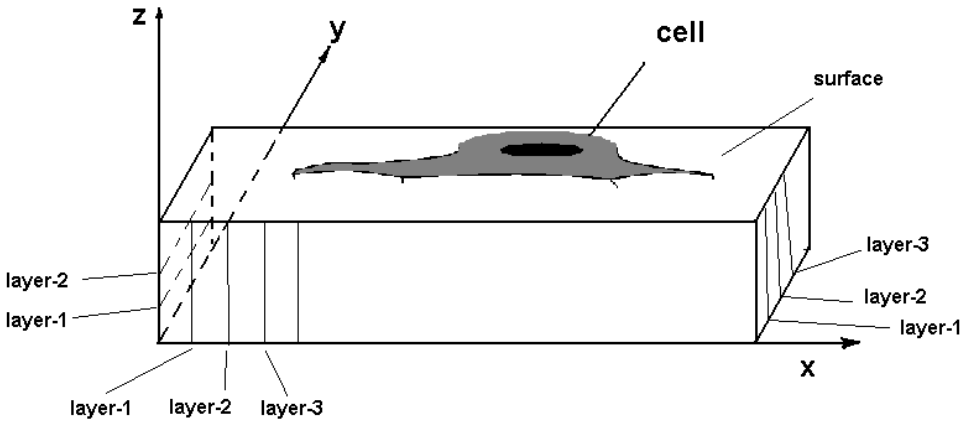

Figure 25. Three dimensional representation of the simulated substrate
Layers along each axis identify the planes in which data can be sampled. The lower numbered layers are those closer to the defined axes

Data can be sampled along any plane (*xy, yz, zx*), however for the purposes of examining the stresses of myocyte contraction, we looked at data along the *xy* plane. The specific layers used for this study were layers 8 & 4 to provide data near the surface and data in the middle that contains less noise.

We used another program to select the data along the desired layer and isolate it into data files. We then use MATLAB to translate these displacement data into the final stress maps.

Chapter 6: Results

6.I. Gel Stiffness Confirmation

The following graph illustrates the results of AFM indentation testing performed on 75 kPa, 30 kPa and 7 kPa acrylamide gels:

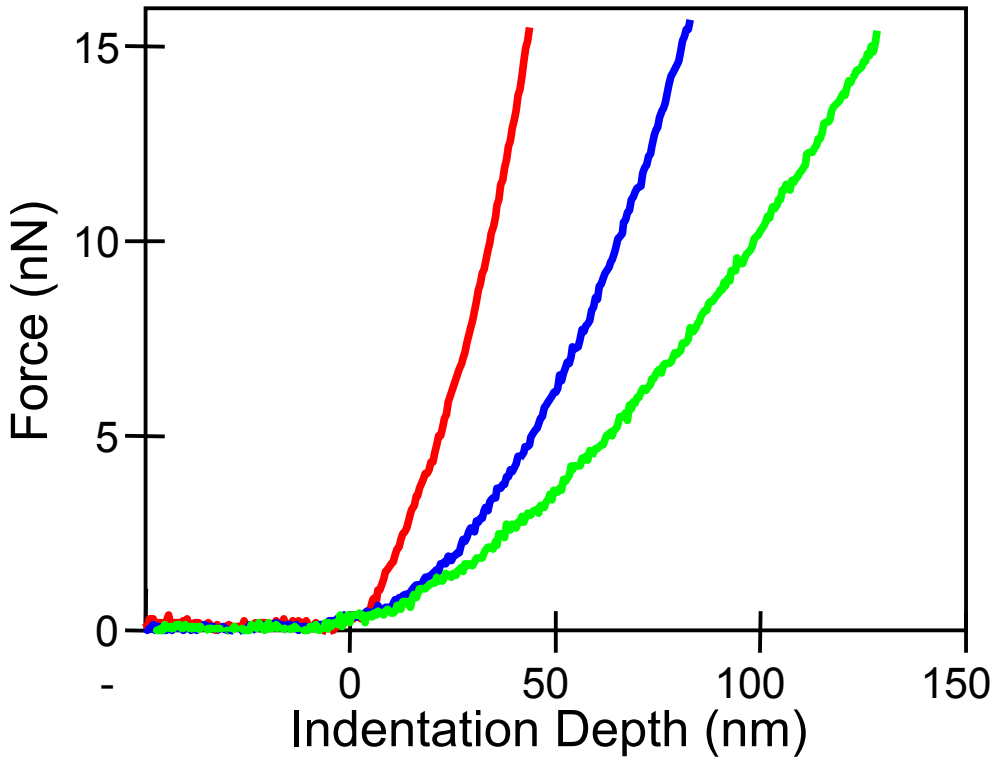

Graph 1. AFM indentation curves on acrylamide gels
Red = 75 kPa, Blue = 30 kPa, Green = 7 kPa

Gels in PBS were indented to a maximum force of 15nN with a 2.5um radius borosilicate spherical probe with spring constant ~0.58N/m. Red was 75kPa, Blue was 30kPa, and Green was 7kPa. Measurements of 68.4 kPa were obtained for the 75 kPa gel, 36.1 kPa for the 30 kPa gel and 7.6 kPa for the 7 kPa gel. There was very little hysteresis for these curves (the indenting and retracting curves overlapped almost entirely) which is

why they are not seen in Graph 1. Also, there was little variation in the modulus at different locations.

6.II. Stress Maps

All of the following data sets contain stress maps for substrates at 75 kPa, 30 kPa and 7 kPa. Each set of results with the same Young's Modulus contains phase images of the contracting cells, 2D and 3D stress maps at layer-8 in the *x* and *y* directions, and 2D and 3D stress maps at layer-8 in the *x* and *y* directions. It is observed that the figures in layer-8 consistently contain more noise than those in layer-4. The cause of this is assumed to be due to the numerous cell contact sites to the substrate and as such generate random displacements on the surface. However, the larger stresses resulting from contraction are still apparent. This topic will be discussed further in Chapter 7. Lastly, remember that due to the simplification of the elements in the dynamic simulation to nodes of mass *m*, the absolute magnitudes of stress can not be assured to be accurate. However, the relative trends between sets of data are still representative of the actual stresses applied during myocyte contraction.

6.II.A. 75 kPa Acrylamide Gels

6.II.A.1. Aligned Data Set 1

Figure 26 shows the two phase images of aligned cells under contraction. All images are taken with a 40x objective and are 220 μm *x* 166 μm in size. Figure 27 shows the displacement map generated through Optical Flow. Figure 28 shows the stress in the *x* direction on layer-8. Figure 29 shows the stress in the *y* direction on layer-8. Figure 30

shows the stress in the *x* direction on layer-4. Figure 31 shows the stress in the *y* direction on layer-4. The maximum and minimum stresses in the *x* direction were 445 kPa and -353 kPa. The maximum and minimum stress in the *y* direction were 395 kPa and -280 kPa.

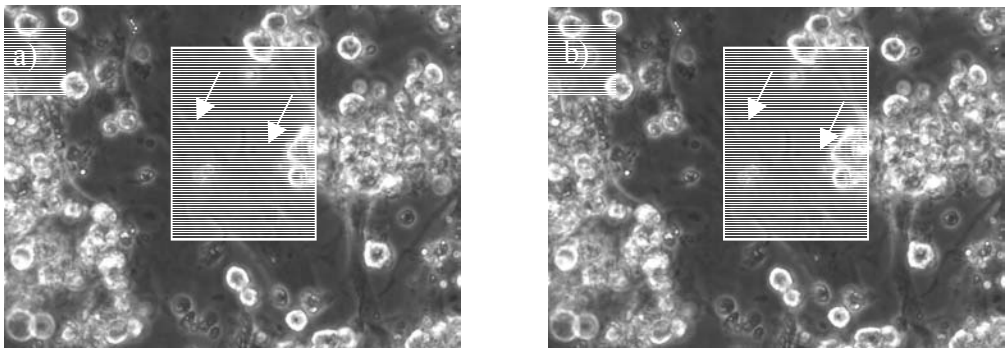

Figure 26. 40x Phase images of aligned myocytes undergoing contraction
Two consecutive images taken from a time lapse with <1ms between images. Debris can be seen on top of the cell culture; however, myocytes are aligned underneath. Arrows indicate the cells in consideration in the enclosed area of interest

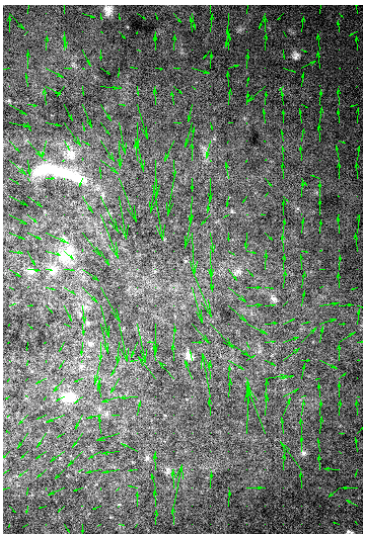

Figure 27. Fluorescent bead image masked with displacement data
The fluorescent image corresponds to the enclosed area in Figure 26a and uses green arrows to indicate the displacement of each node as defined in the program.

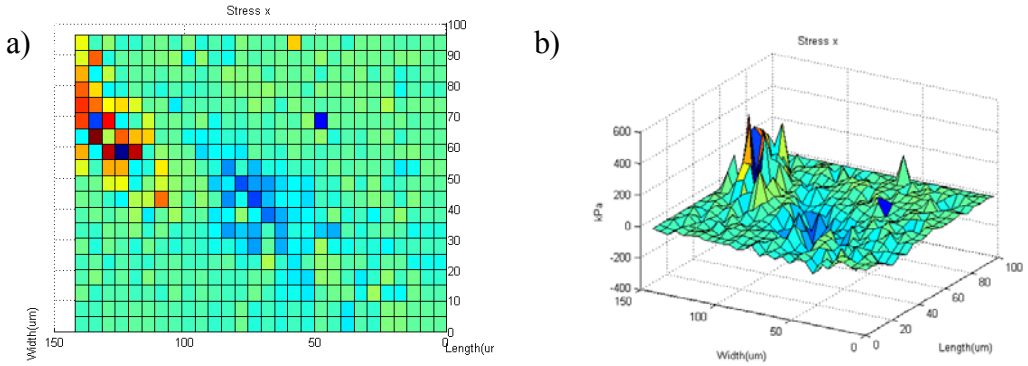

Figure 28. Stress maps of the stress in the *x* direction on layer-8
a) shows the 2D stress along layer-8 and b) shows the 3D stress along layer-8. The positive values indicate stress in the positive *x* direction and negative values indicate stress in the negative *x* direction.

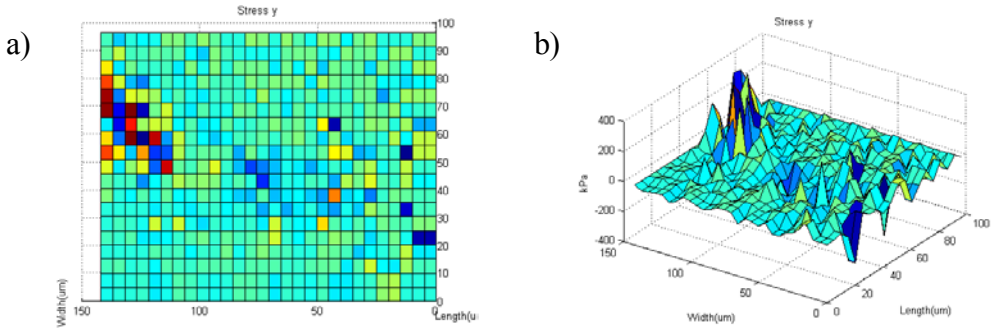

Figure 29. Stress maps of the stress in the *y* direction on layer-8
a) shows the 2D stress along layer-8 and b) shows the 3D stress along layer-8. The positive values indicate stress in the positive *y* direction and negative values indicate stress in the negative *y* direction.

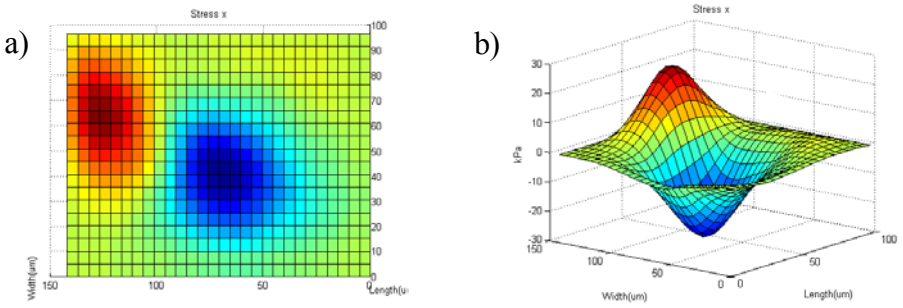

Figure 30. Stress maps of the stress in the *x* direction on layer-4
a) shows the 2D stress along layer-4 and b) shows the 3D stress along layer-4. The positive values indicate stress in the positive *x* direction and negative values indicate stress in the negative *x* direction.

a) b)

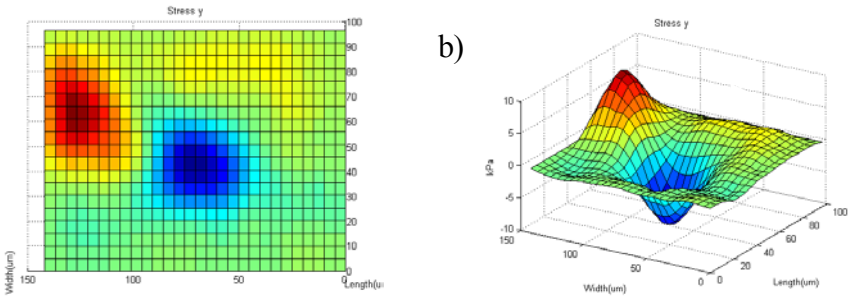

Figure 31. Stress maps of the stress in the *y* direction on layer-4
a) shows the 2D stress along layer-4 and b) shows the 3D stress along layer-4. The positive values indicate stress in the positive *y* direction and negative values indicate stress in the negative *y* direction.

6.II.A.2. Aligned Data Set 2

Figure 32 shows the two phase images of aligned cells under contraction (similar to Figure 26 but different time points in time lapse set). For the following images, consider them to be mirrored across the *y* axis. Figure 33 shows the displacement map generated through Optical Flow. Figure 34 shows the stress in the *x* direction on layer-8. Figure 35 shows the stress in the *y* direction on layer-8. Figure 36 shows the stress in the *x* direction on layer-4. Figure 37 shows the stress in the *y* direction on layer-4. The maximum and minimum stresses in the *x* direction were 460 kPa and -360 kPa. The maximum and minimum stress in the *y* direction were 450 kPa and -280 kPa.

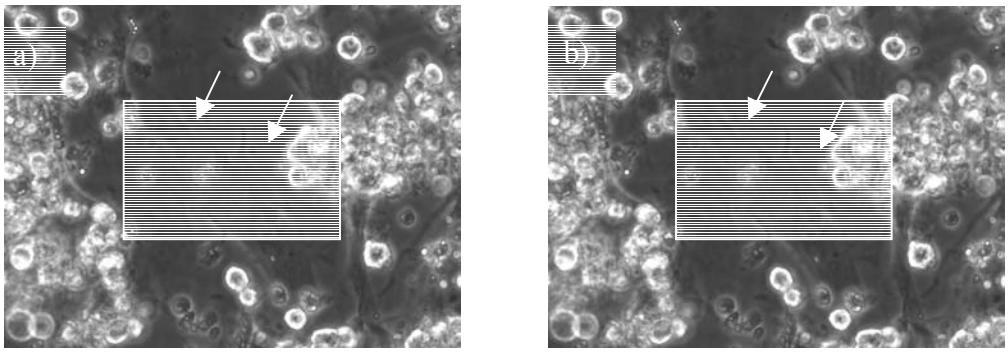

Figure 32. 40x Phase images of aligned myocytes undergoing contraction
Two consecutive images taken from a time lapse with <1ms between images. Debris can be seen on top of the cell culture; however, myocytes are aligned underneath. Arrows indicate the cells in consideration in the enclosed area of interest

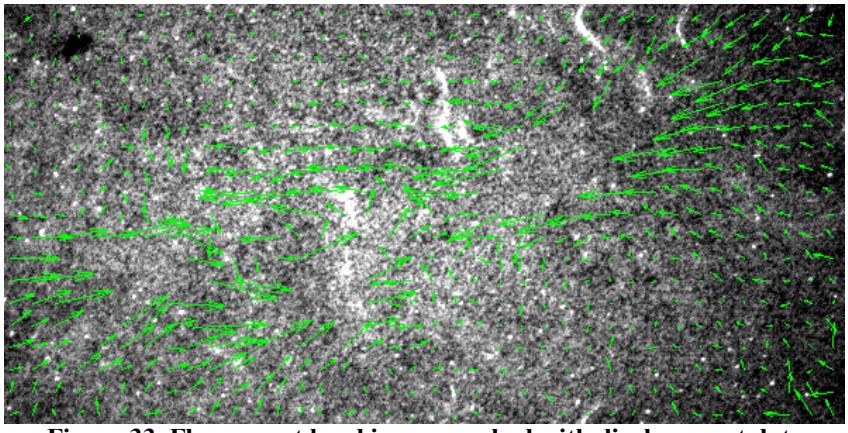

Figure 33. Fluorescent bead image masked with displacement data
The fluorescent image corresponds to the enclosed area in Figure 32a and uses green arrows to indicate the displacement of each node as defined in the program.

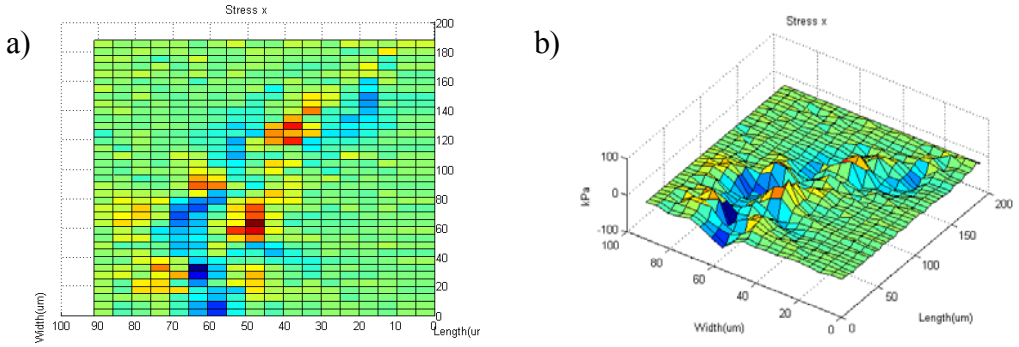

Figure 34. Stress maps of the stress in the *x* direction on layer-8
a) shows the 2D stress along layer-8 and b) shows the 3D stress along layer-8. The positive values indicate stress in the positive *x* direction and negative values indicate stress in the negative *x* direction.

a) b)

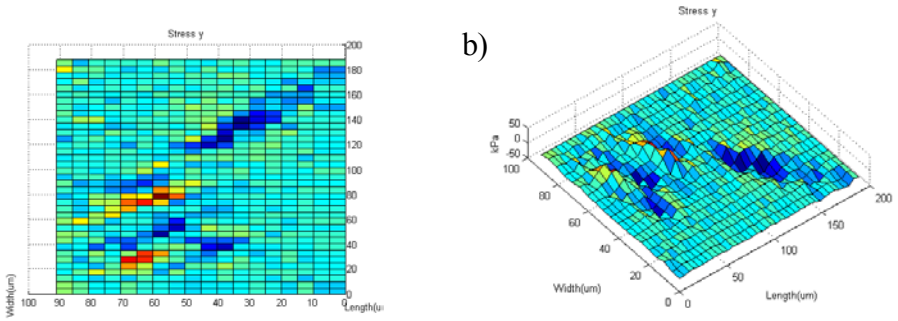

Figure 35. Stress maps of the stress in the *y* direction on layer-8
a) shows the 2D stress along layer-8 and b) shows the 3D stress along layer-8. The positive values indicate stress in the positive *y* direction and negative values indicate stress in the negative *y* direction.

a) b)

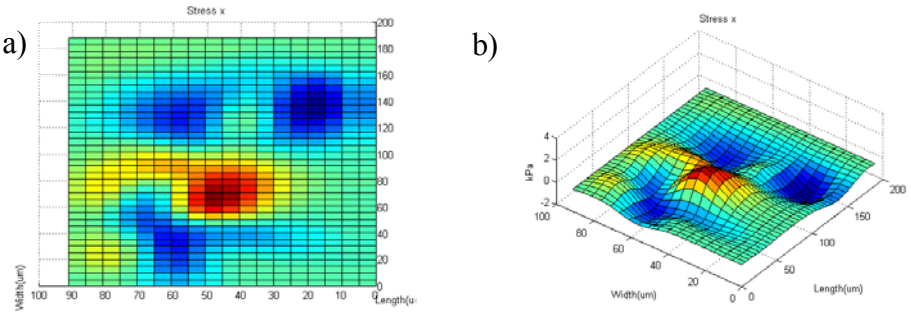

Figure 36. Stress maps of the stress in the *x* direction on layer-4
a) shows the 2D stress along layer-4 and b) shows the 3D stress along layer-4. The positive values indicate stress in the positive *x* direction and negative values indicate stress in the negative *x* direction.

a) b)

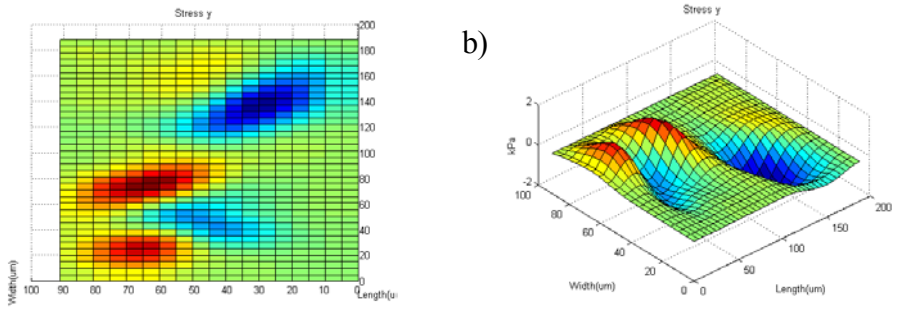

Figure 37. Stress maps of the stress in the *y* direction on layer-4
a) shows the 2D stress along layer-4 and b) shows the 3D stress along layer-4. The positive values indicate stress in the positive *y* direction and negative values indicate stress in the negative *y* direction.

6.II.A.3. Aligned Data Set 3

Figure 38 shows the two phase images of aligned cells under contraction (similar to Figure 26 but different time points in time lapse set). For the following images, consider them to be mirrored across the *y* axis. Figure 39 shows the displacement map generated through Optical Flow. Figure 49 shows the stress in the *x* direction on layer-8. Figure 41 shows the stress in the *y* direction on layer-8. Figure 42 shows the stress in the *x* direction on layer-4. Figure 43 shows the stress in the *y* direction on layer-4. The maximum and minimum stresses in the *x* direction were 460 kPa and -570 kPa. The maximum and minimum stress in the *y* direction were 430 kPa and -260 kPa.

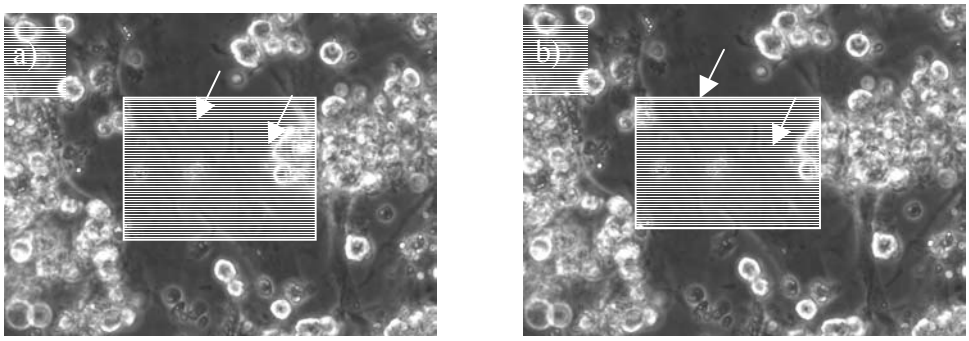

Figure 38. 40x Phase images of aligned myocytes undergoing contraction
Two consecutive images taken from a time lapse with <1ms between images. Debris can be seen on top of the cell culture; however, myocytes are aligned underneath. Arrows indicate the cells in consideration in the enclosed area of interest

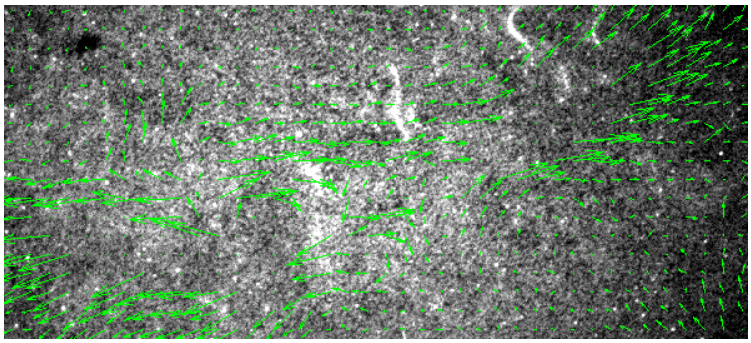

Figure 39. Fluorescent bead image masked with displacement data
The fluorescent image corresponds to the enclosed area in Figure 38a and uses green arrows to indicate the displacement of each node as defined in the program.

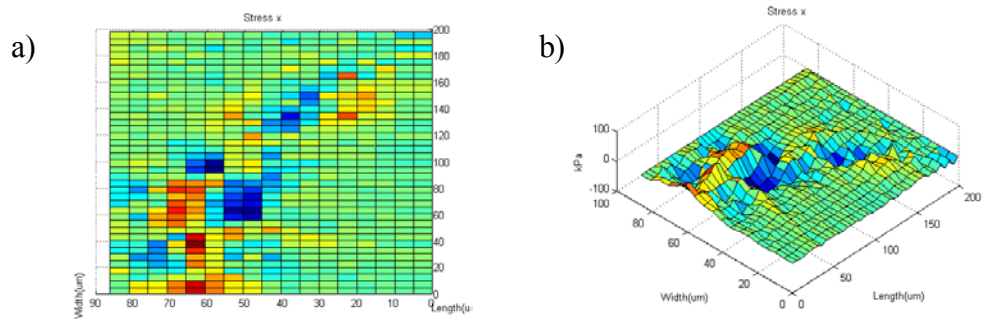

Figure 40. Stress maps of the stress in the *x* direction on layer-8
a) shows the 2D stress along layer-8 and b) shows the 3D stress along layer-8. The positive values indicate stress in the positive *x* direction and negative values indicate stress in the negative *x* direction.

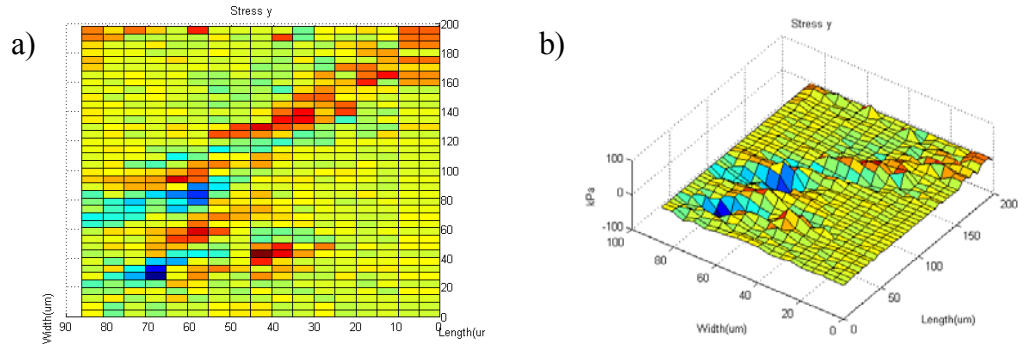

Figure 41. Stress maps of the stress in the *y* direction on layer-8
a) shows the 2D stress along layer-8 and b) shows the 3D stress along layer-8. The positive values indicate stress in the positive *y* direction and negative values indicate stress in the negative *y* direction.

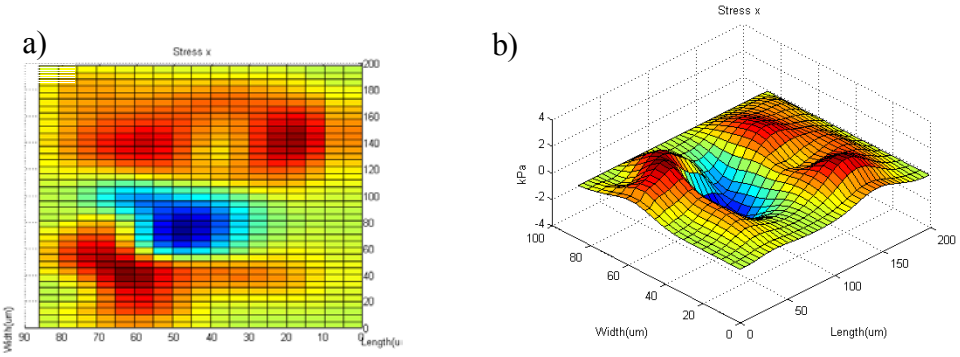

Figure 42. Stress maps of the stress in the *x* direction on layer-4
a) shows the 2D stress along layer-4 and b) shows the 3D stress along layer-4. The positive values indicate stress in the positive *x* direction and negative values indicate stress in the negative *x* direction.

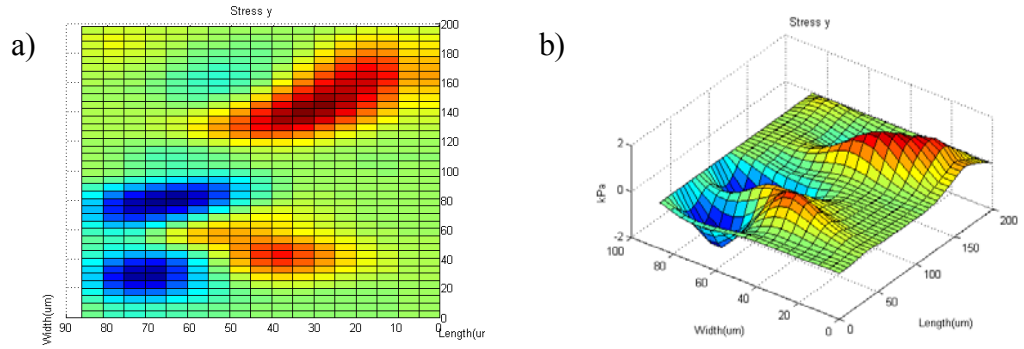

Figure 43. Stress maps of the stress in the *y* direction on layer-4
a) shows the 2D stress along layer-4 and b) shows the 3D stress along layer-4. The positive values indicate stress in the positive *y* direction and negative values indicate stress in the negative *y* direction.

6.II.A.4. Random Data Set 1

Figure 44 shows the two phase images of random cells under contraction. Figure 45 shows the displacement map generated through Optical Flow. Figure 46 shows the stress in the *x* direction on layer-8. Figure 47 shows the stress in the *y* direction on layer-8. Figure 48 shows the stress in the *x* direction on layer-4. Figure 49 shows the stress in the *y* direction on layer-4. The maximum and minimum stresses in the *x* direction were 80 kPa and -100 kPa. The maximum and minimum stress in the *y* direction were 183 kPa and -81 kPa.

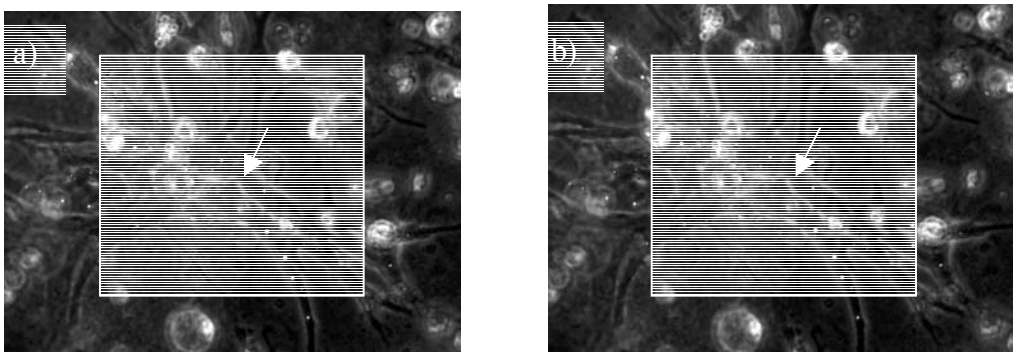

Figure 44. 40x Phase images of unaligned myocytes undergoing contraction
Two consecutive images taken from a time lapse with <1ms between images. Arrows indicate the cell in consideration in the enclosed area of interest. The cell morphology is less phenotypic (rod-like) than cells in the aligned data sets (Figures 26, 32 and 38)

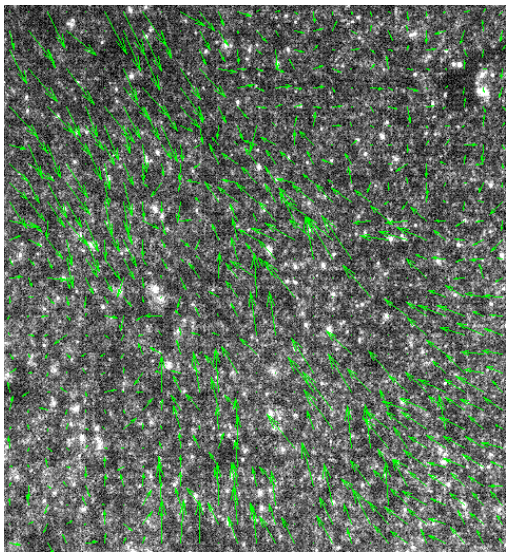

Figure 45. Fluorescent bead image masked with displacement data
The fluorescent image corresponds to the enclosed area in Figure 44a and uses green arrows to indicate the displacement of each node as defined in the program.

a)

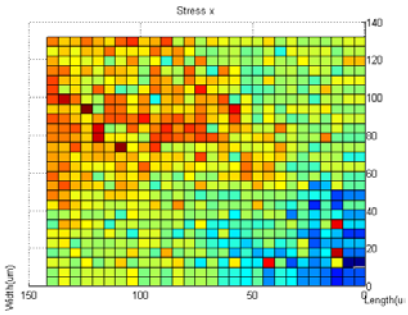

b)

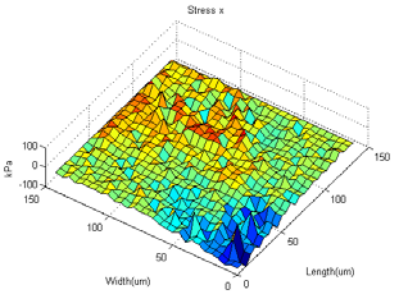

Figure 46. Stress maps of the stress in the *x* direction on layer-8
a) shows the 2D stress along layer-8 and b) shows the 3D stress along layer-8. The positive values indicate stress in the positive *x* direction and negative values indicate stress in the negative *x* direction.

a)

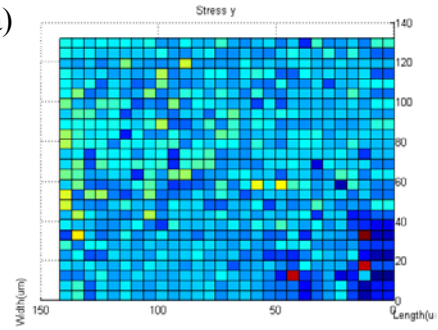

b)

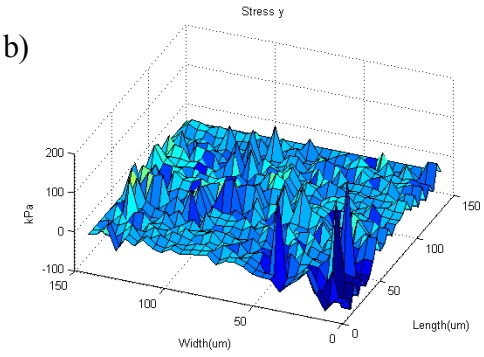

Figure 47. Stress maps of the stress in the *y* direction on layer-8
a) shows the 2D stress along layer-8 and b) shows the 3D stress along layer-8. The positive values indicate stress in the positive *y* direction and negative values indicate stress in the negative *y* direction.

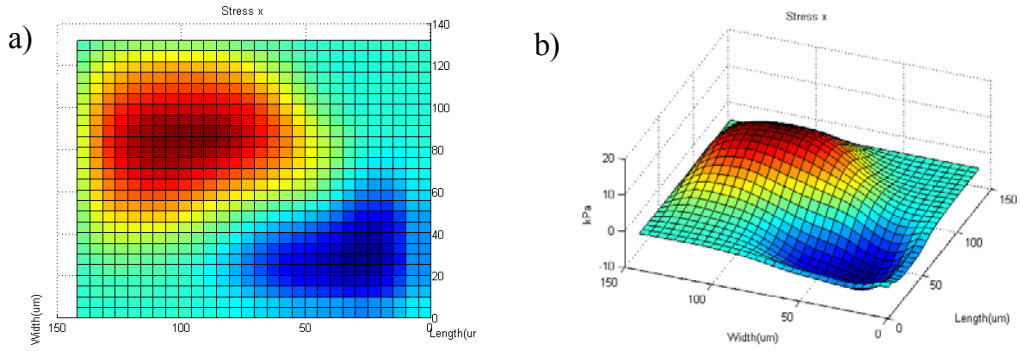

Figure 48. Stress maps of the stress in the *x* direction on layer-4
a) shows the 2D stress along layer-4 and b) shows the 3D stress along layer-4. The positive values indicate stress in the positive *x* direction and negative values indicate stress in the negative *x* direction.

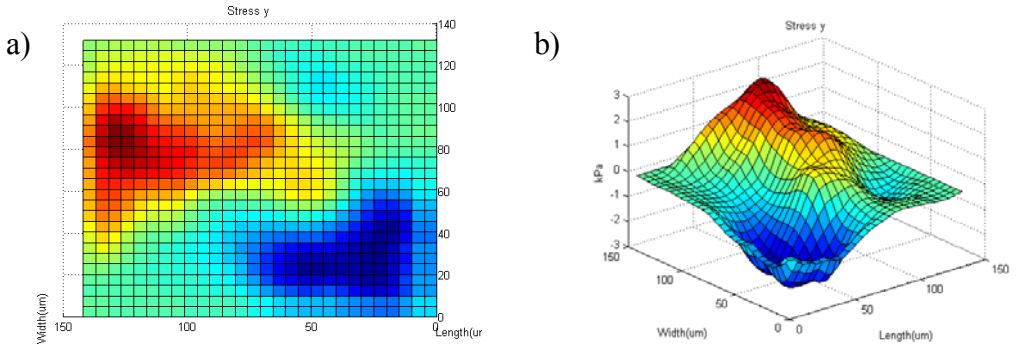

Figure 49. Stress maps of the stress in the *y* direction on layer-4
a) shows the 2D stress along layer-4 and b) shows the 3D stress along layer-4. The positive values indicate stress in the positive *y* direction and negative values indicate stress in the negative *y* direction.

6.II.A.5. Random Data Set 2

Figure 50 shows the two phase images of random cells under contraction. Figure 51 shows the displacement map generated through Optical Flow. Figure 52 shows the stress in the *x* direction on layer-8. Figure 53 shows the stress in the *y* direction on layer-8. Figure 54 shows the stress in the *x* direction on layer-4. Figure 55 shows the stress in the *y* direction on layer-4. The maximum and minimum stresses in the *x* direction were 1700 kPa and -700 kPa. The maximum and minimum stress in the *y* direction were 2200 kPa and -2500 kPa. Each of these measurements contained large point stresses that

indicate a strong contraction; however, the strength of these points was not consistently represented along the edge of the cell.

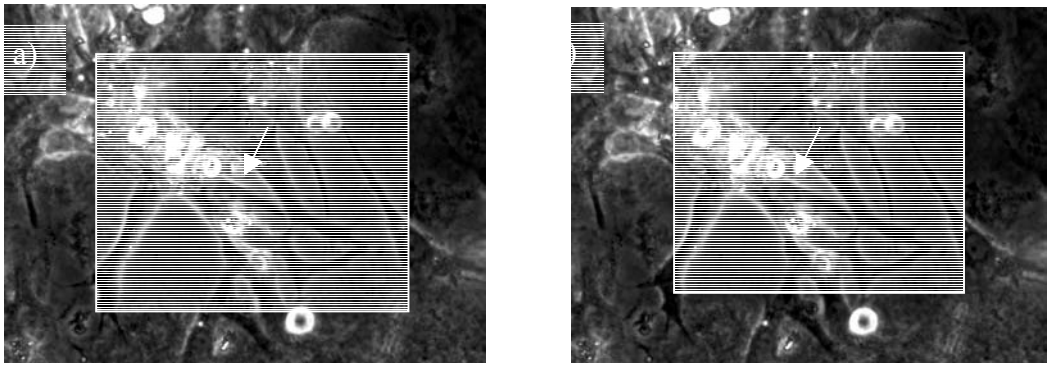

Figure 50. 40x Phase images of unaligned myocytes undergoing contraction
Two consecutive images taken from a time lapse with <1ms between images. Arrows indicate the cell in consideration in the enclosed area of interest. The cell morphology is less phenotypic (rod-like) than cells in the aligned data sets (Figures 26, 43 and 38)

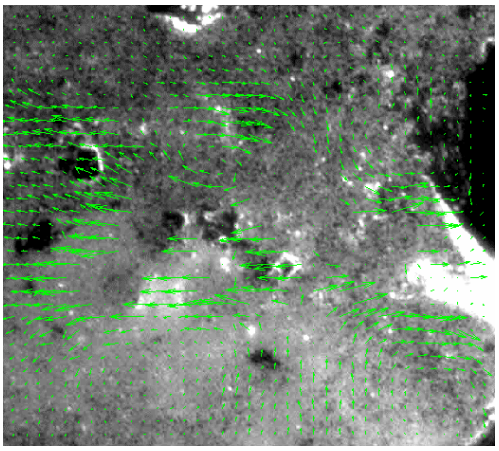

Figure 51. Fluorescent bead image masked with displacement data
The fluorescent image corresponds to the enclosed area in Figure 50a and uses green arrows to indicate the displacement of each node as defined in the program.

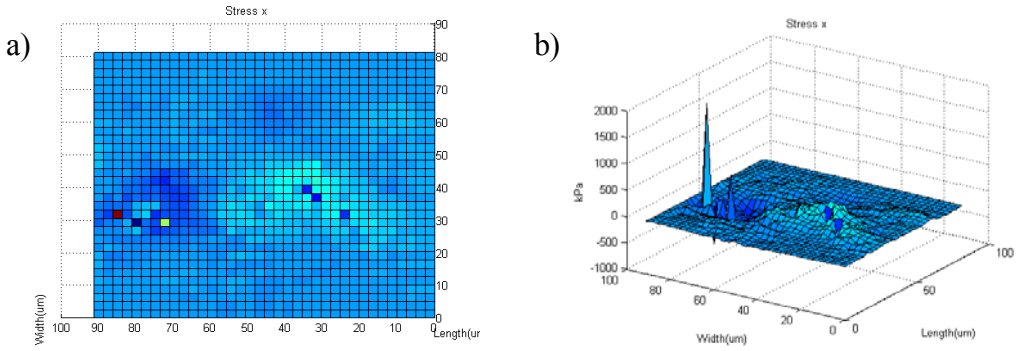

Figure 52. Stress maps of the stress in the *x* direction on layer-8
a) shows the 2D stress along layer-8 and b) shows the 3D stress along layer-8. The positive values indicate stress in the positive *x* direction and negative values indicate stress in the negative *x* direction. Notice the large point stresses along the left side of the graphs

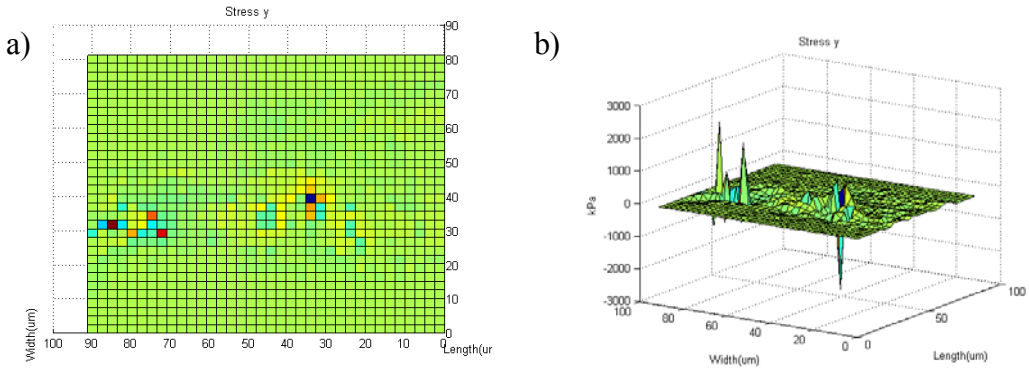

Figure 53. Stress maps of the stress in the *y* direction on layer-8
a) shows the 2D stress along layer-8 and b) shows the 3D stress along layer-8. The positive values indicate stress in the positive *y* direction and negative values indicate stress in the negative *y* direction. Notice the large point stresses along the left side of the graphs

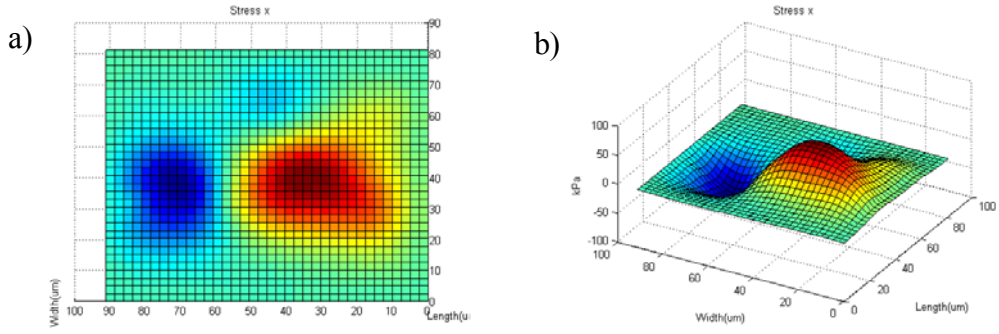

Figure 54. Stress maps of the stress in the *x* direction on layer-4
a) shows the 2D stress along layer-4 and b) shows the 3D stress along layer-4. The positive values indicate stress in the positive *x* direction and negative values indicate stress in the negative *x* direction.

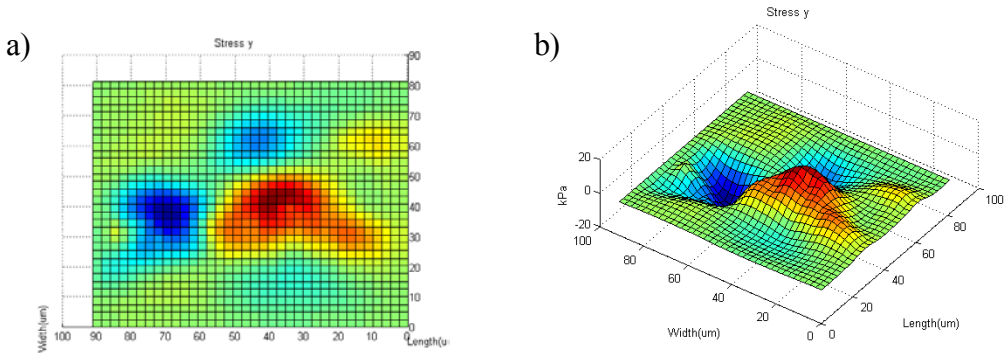

Figure 55. Stress maps of the stress in the *y* direction on layer-4
a) shows the 2D stress along layer-4 and b) shows the 3D stress along layer-4. The positive values indicate stress in the positive *y* direction and negative values indicate stress in the negative *y* direction.

6.II.A.6. Random Data Set 3

Figure 56 shows the two phase images of random cells under contraction. Figure 57 shows the displacement map generated through Optical Flow. Figure 58 shows the stress in the *x* direction on layer-8. Figure 59 shows the stress in the *y* direction on layer-8. Figure 60 shows the stress in the *x* direction on layer-4. Figure 61 shows the stress in the *y* direction on layer-4. The maximum and minimum stresses in the *x* direction were 1200 kPa and -415 kPa. The maximum and minimum stress in the *y* direction were 700 kPa and -2350 kPa. Each of these measurements contained large point stresses that indicate a strong contraction; however, the strength of these points was not consistently represented along the edge of the cell.

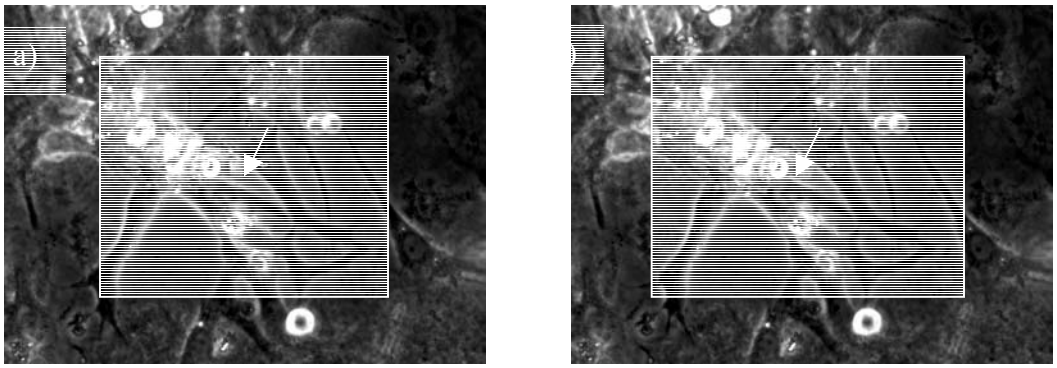

Figure 56. 40x Phase images of unaligned myocytes undergoing contraction
Two consecutive images taken from a time lapse with <1ms between images. Arrows indicate the cell in consideration in the enclosed area of interest. The cell morphology is less phenotypic (rod-like) than cells in the aligned data sets (Figures 26,32 and 38)

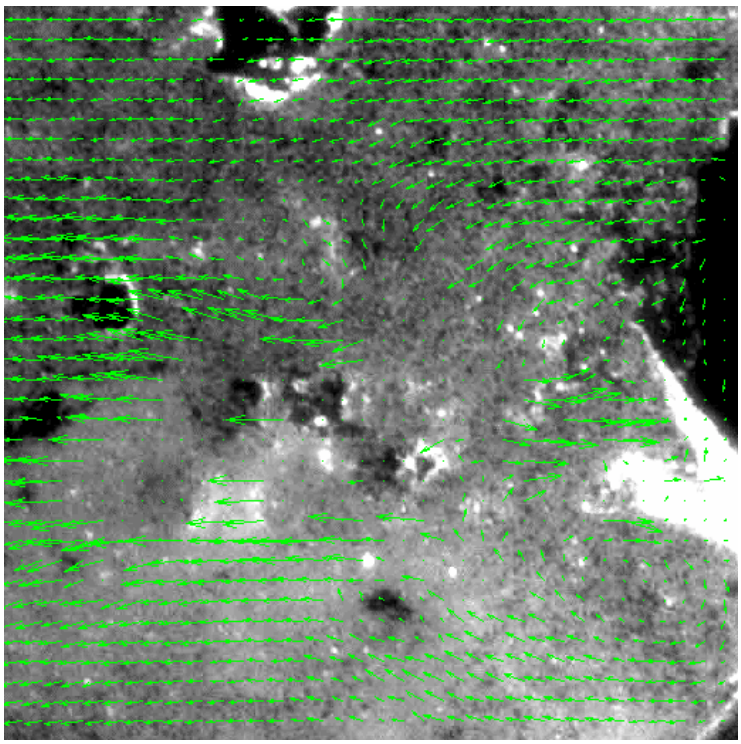

Figure 57. Fluorescent bead image masked with displacement data
The fluorescent image corresponds to the enclosed area in Figure 56a and uses green arrows to indicate the displacement of each node as defined in the program.

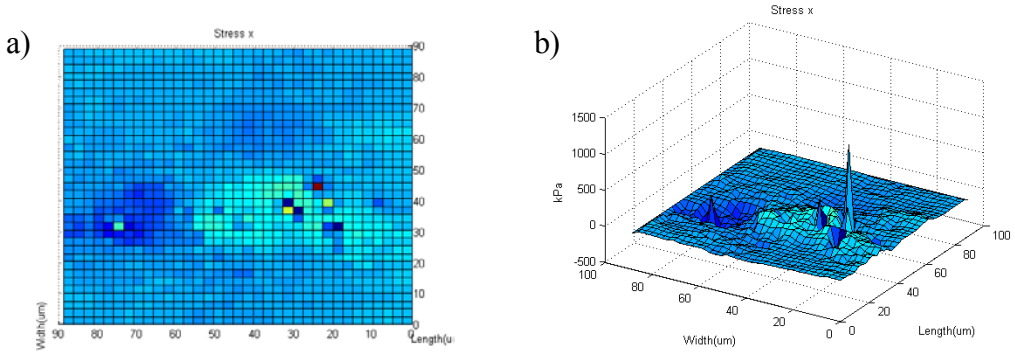

Figure 58. Stress maps of the stress in the *x* direction on layer-8
a) shows the 2D stress along layer-8 and b) shows the 3D stress along layer-8. The positive values indicate stress in the positive *x* direction and negative values indicate stress in the negative *x* direction. Notice the large point stresses.

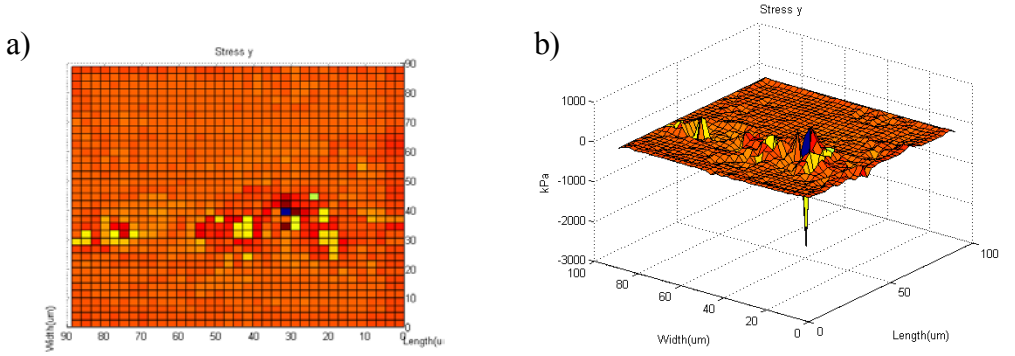

Figure 59 Stress maps of the stress in the *y* direction on layer-8
a) shows the 2D stress along layer-8 and b) shows the 3D stress along layer-8. The positive values indicate stress in the positive *y* direction and negative values indicate stress in the negative *y* direction. Notice the large point stresses.

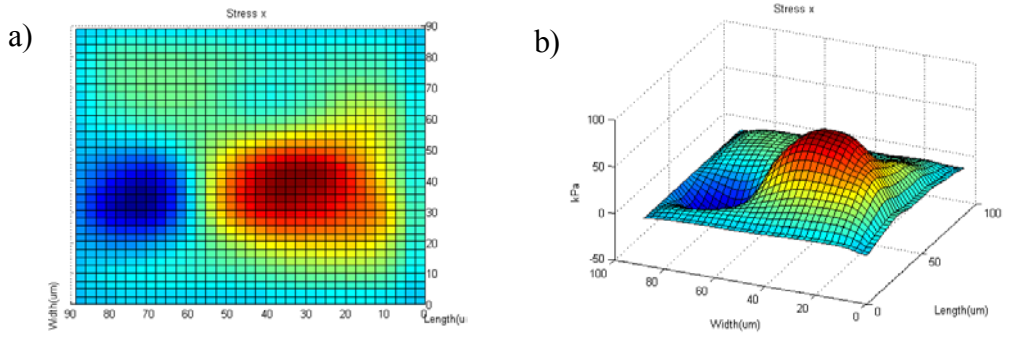

Figure 60. Stress maps of the stress in the *x* direction on layer-4
a) shows the 2D stress along layer-4 and b) shows the 3D stress along layer-4. The positive values indicate stress in the positive *x* direction and negative values indicate stress in the negative *x* direction.

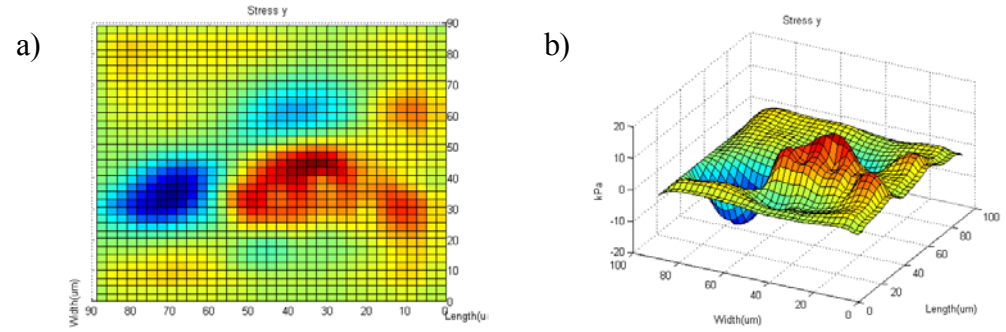

Figure 61. Stress maps of the stress in the *y* direction on layer-4
a) shows the 2D stress along layer-4 and b) shows the 3D stress along layer-4. The positive values indicate stress in the positive *y* direction and negative values indicate stress in the negative *y* direction.

6.II.B. 30 kPa Acrylamide Gels

6.II.B.1. Aligned Data Set 1

Figure 62 shows the two phase images of aligned cells under contraction. All images are taken with a 40x objective and are 220 µm *x* 166 µm in size. Figure 63 shows the displacement map generated through Optical Flow. Figure 64 shows the stress in the *x* direction on layer-8. Figure 65 shows the stress in the *y* direction on layer-8. Figure 66 shows the stress in the *x* direction on layer-4. Figure 67 shows the stress in the *y* direction on layer-4. The maximum and minimum stresses in the *x* direction were 150 kPa and -460 kPa. The maximum and minimum stress in the *y* direction were 430 kPa and -55 kPa.

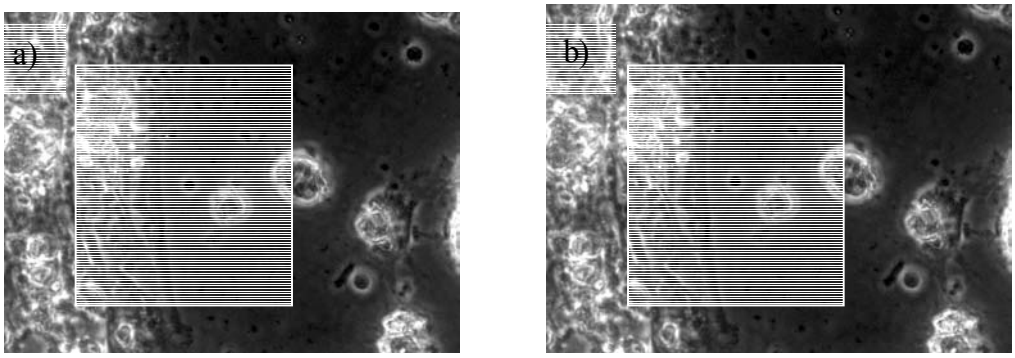

Figure 62. 40x Phase images of aligned myocytes undergoing contraction
Two consecutive images taken from a time lapse with <1ms between images.

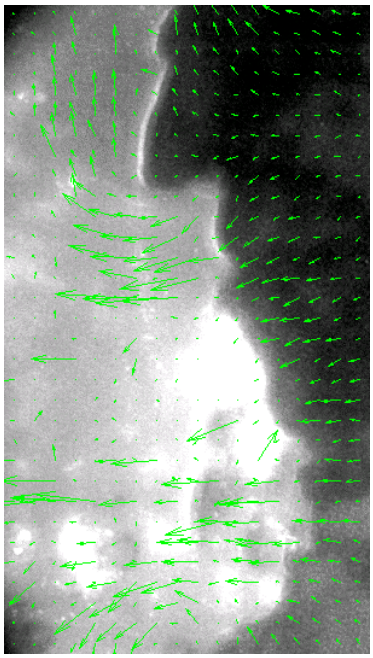

Figure 63. Fluorescent bead image masked with displacement data
The fluorescent image corresponds to the enclosed area in Figure 62a and uses green arrows to indicate the displacement of each node as defined in the program.

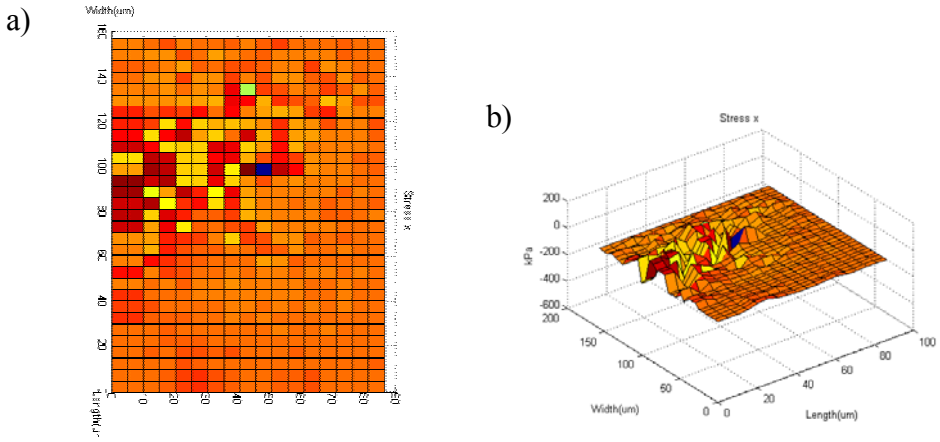

Figure 64. Stress maps of the stress in the *x* direction on layer-8
a) shows the 2D stress along layer-8 and b) shows the 3D stress along layer-8. The positive values indicate stress in the positive *x* direction and negative values indicate stress in the negative *x* direction.

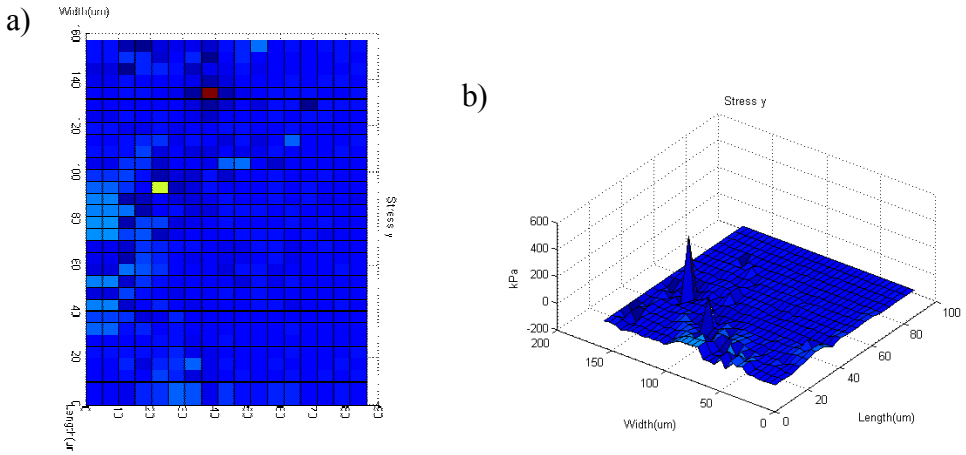

Figure 65. Stress maps of the stress in the *y* direction on layer-8
a) shows the 2D stress along layer-8 and b) shows the 3D stress along layer-8. The positive values indicate stress in the positive *y* direction and negative values indicate stress in the negative *y* direction.

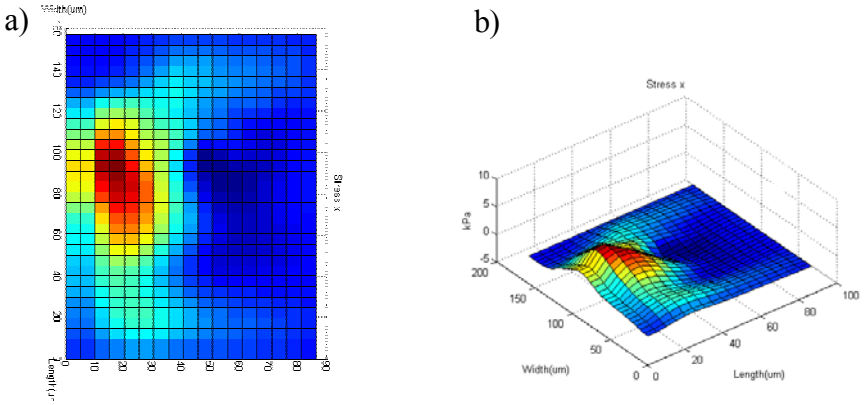

Figure 66. Stress maps of the stress in the *x* direction on layer-4
a) shows the 2D stress along layer-4 and b) shows the 3D stress along layer-4. The positive values indicate stress in the positive *x* direction and negative values indicate stress in the negative *x* direction.

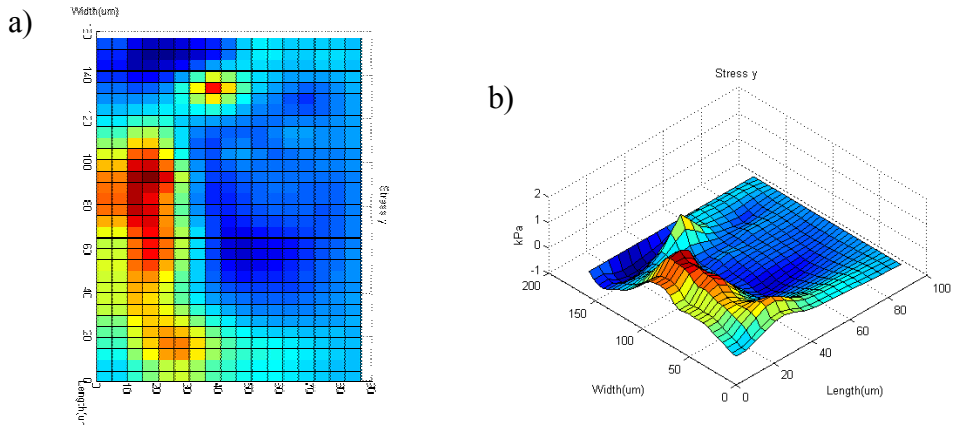

Figure 67. Stress maps of the stress in the *y* direction on layer-4
a) shows the 2D stress along layer-4 and b) shows the 3D stress along layer-4. The positive values indicate stress in the positive *y* direction and negative values indicate stress in the negative *y* direction.

6.II.B.2. Aligned Data Set 2

Figure 68 shows the two phase images of aligned cells under contraction (similar to Figure 62 but different time points in time lapse set). For the following images, consider them to be mirrored across the *y* axis. Figure 69 shows the displacement map generated through Optical Flow. Figure 70 shows the stress in the *x* direction on layer-8. Figure 71 shows the stress in the *y* direction on layer-8. Figure 72 shows the stress in the *x* direction on layer-4. Figure 73 shows the stress in the *y* direction on layer-4. The maximum and minimum stresses in the *x* direction were 77 kPa and -86 kPa. The maximum and minimum stress in the *y* direction were 78 kPa and -240 kPa.

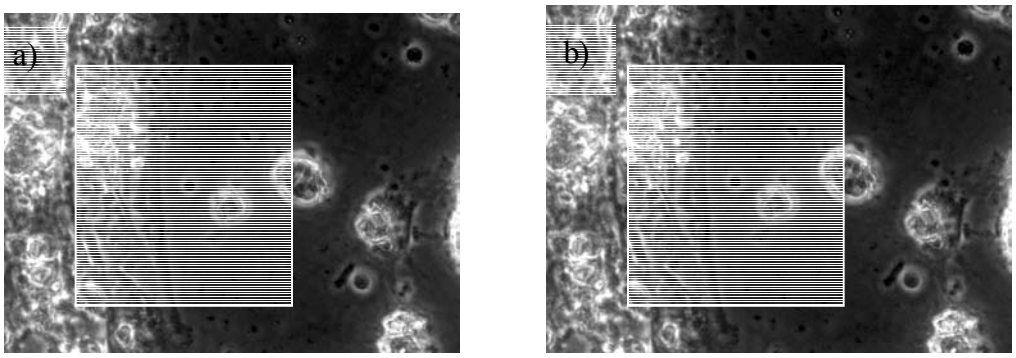

Figure 68. 40x Phase images of aligned myocytes undergoing contraction
Two consecutive images taken from a time lapse with <1ms between images.

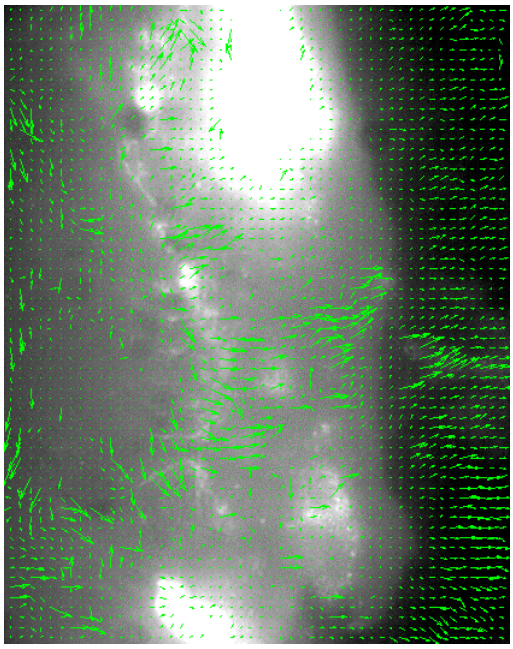

Figure 69. Fluorescent bead image masked with displacement data
The fluorescent image corresponds to the enclosed area in Figure 68a and uses green arrows to indicate the displacement of each node as defined in the program.

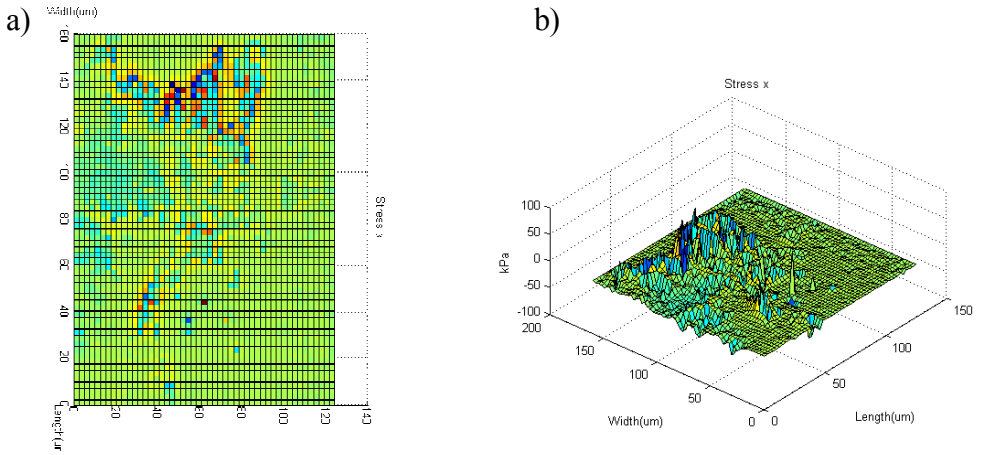

Figure 70. Stress maps of the stress in the *x* direction on layer-8
a) shows the 2D stress along layer-8 and b) shows the 3D stress along layer-8. The positive values indicate stress in the positive *x* direction and negative values indicate stress in the negative *x* direction.

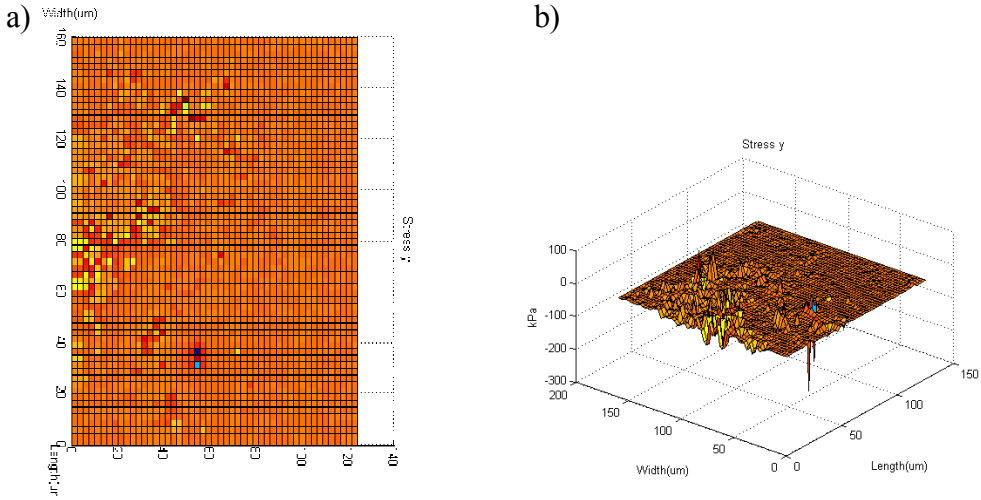

Figure 71. Stress maps of the stress in the *y* direction on layer-8
a) shows the 2D stress along layer-8 and b) shows the 3D stress along layer-8. The positive values indicate stress in the positive *y* direction and negative values indicate stress in the negative *y* direction.

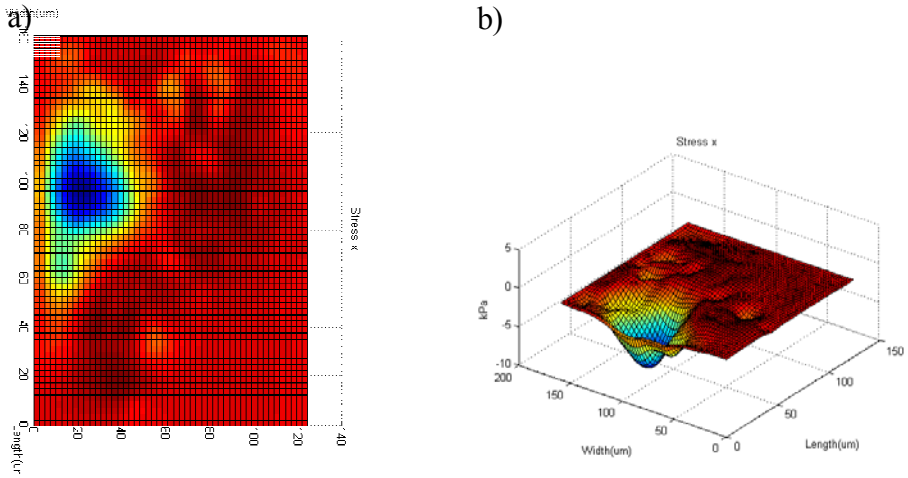

Figure 72. Stress maps of the stress in the *x* direction on layer-4
a) shows the 2D stress along layer-4 and b) shows the 3D stress along layer-4. The positive values indicate stress in the positive *x* direction and negative values indicate stress in the negative *x* direction.

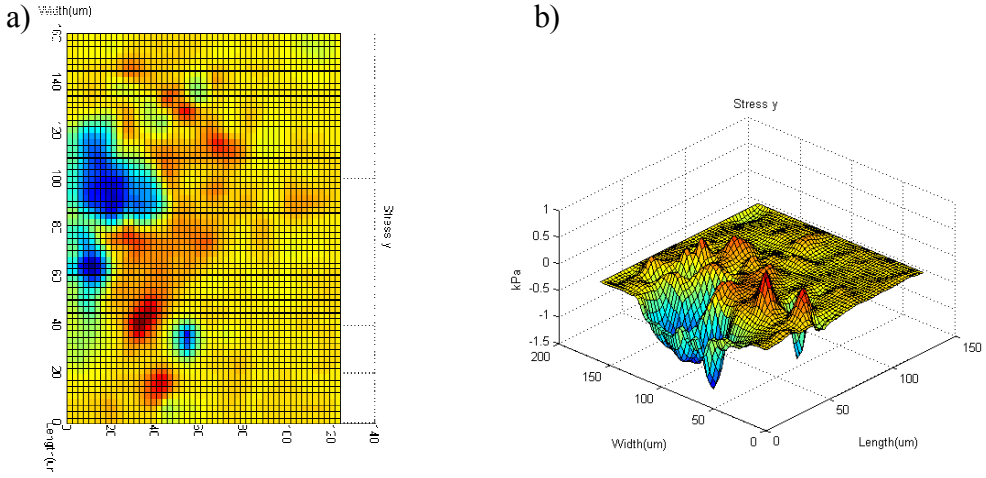

Figure 73. Stress maps of the stress in the *y* direction on layer-4
a) shows the 2D stress along layer-4 and b) shows the 3D stress along layer-4. The positive values indicate stress in the positive *y* direction and negative values indicate stress in the negative *y* direction.

6.II.B.3. Aligned Data Set 3

Figure 74 shows the two phase images of aligned cells under contraction (similar to Figure 62 but different time points in time lapse set). For the following images, consider them to be mirrored across the *y* axis. Figure 75 shows the displacement map

generated through Optical Flow. Figure 76 shows the stress in the *x* direction on layer-8. Figure 77 shows the stress in the *y* direction on layer-8. Figure 78 shows the stress in the *x* direction on layer-4. Figure 79 shows the stress in the *y* direction on layer-4. The maximum and minimum stresses in the *x* direction were 460 kPa and -570 kPa. The maximum and minimum stress in the *y* direction were 430 kPa and -260 kPa.

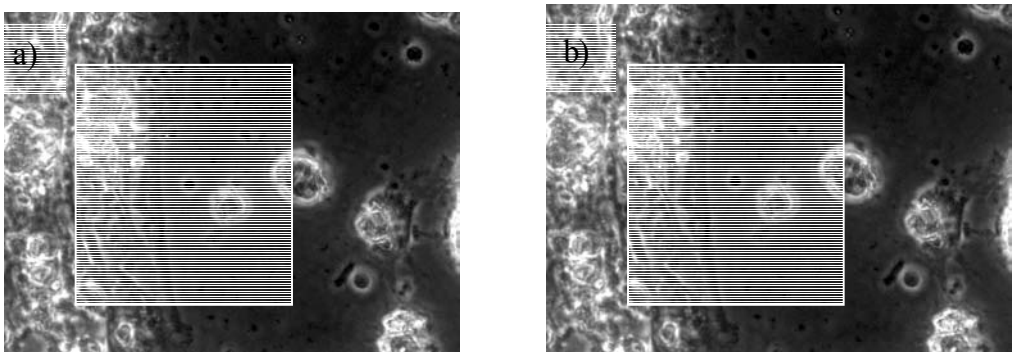

Figure 74. 40x Phase images of aligned myocytes undergoing contraction
Two consecutive images taken from a time lapse with <1ms between images.

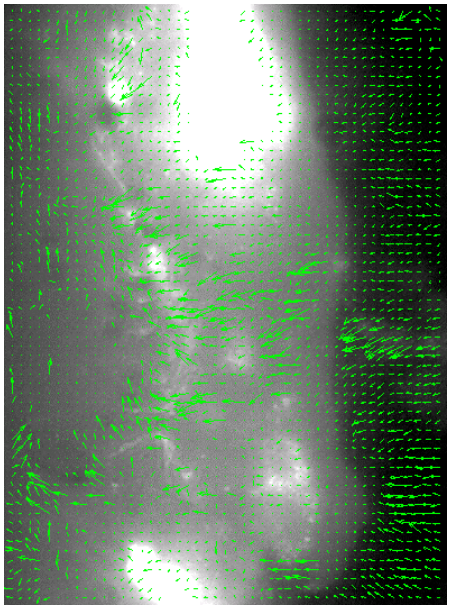

Figure 75. Fluorescent bead image masked with displacement data
The fluorescent image corresponds to the enclosed area in Figure 74a and uses green arrows to indicate the displacement of each node as defined in the program.

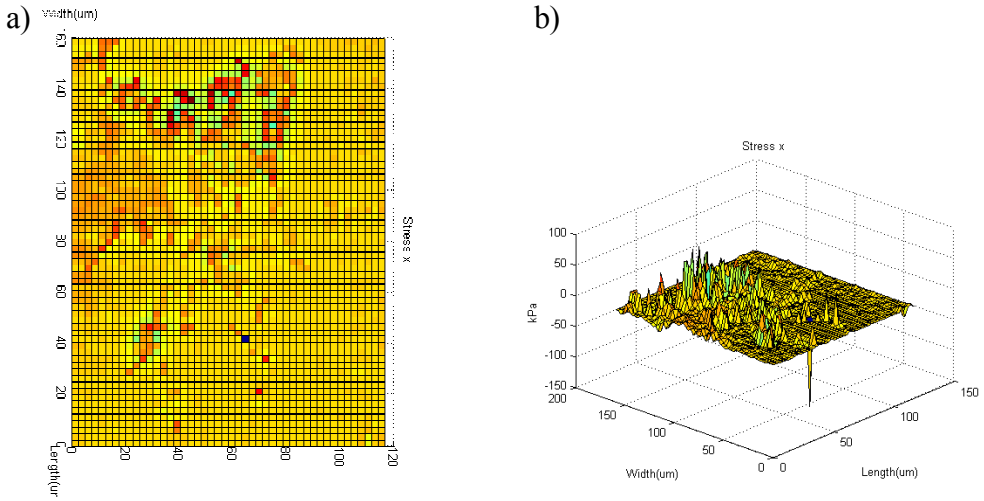

Figure 76. Stress maps of the stress in the *x* direction on layer-8
a) shows the 2D stress along layer-8 and b) shows the 3D stress along layer-8. The positive values indicate stress in the positive *x* direction and negative values indicate stress in the negative *x* direction.

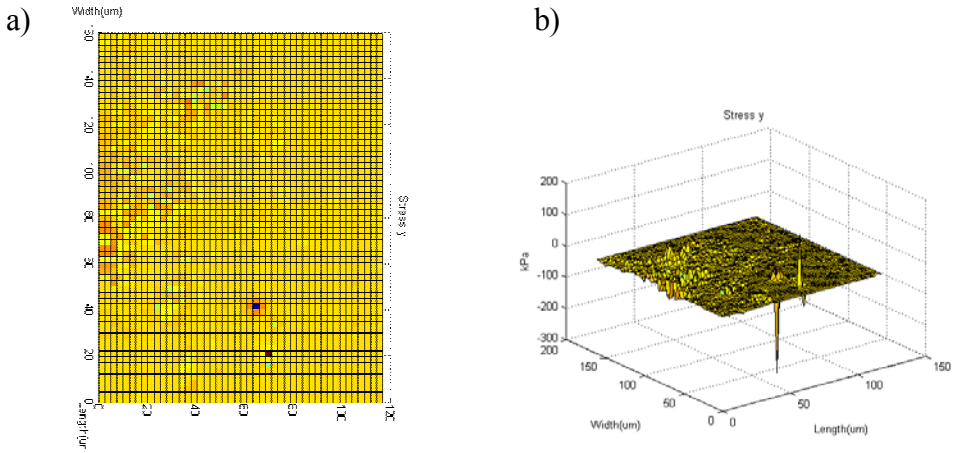

Figure 77. Stress maps of the stress in the *y* direction on layer-8
a) shows the 2D stress along layer-8 and b) shows the 3D stress along layer-8. The positive values indicate stress in the positive *y* direction and negative values indicate stress in the negative *y* direction.

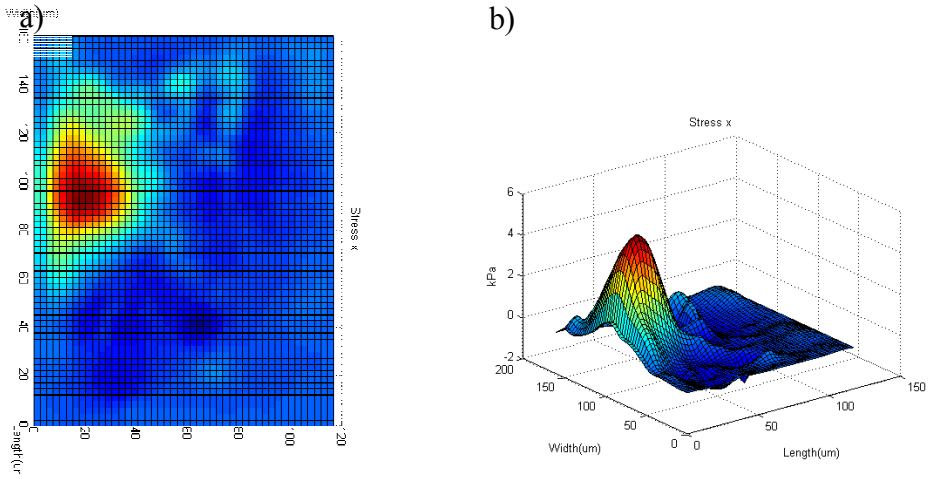

Figure 78. Stress maps of the stress in the *x* direction on layer-4
a) shows the 2D stress along layer-4 and b) shows the 3D stress along layer-4. The positive values indicate stress in the positive *x* direction and negative values indicate stress in the negative *x* direction.

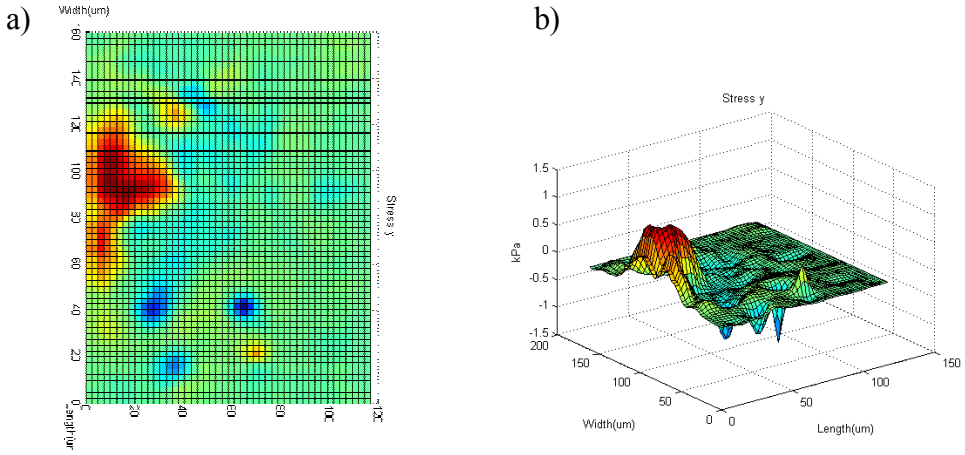

Figure 79. Stress maps of the stress in the *y* direction on layer-4
a) shows the 2D stress along layer-4 and b) shows the 3D stress along layer-4. The positive values indicate stress in the positive *y* direction and negative values indicate stress in the negative *y* direction.

6.II.B.4. Random Data Set 1

Figure 80 shows the two phase images of random cells under contraction. Figure 81 shows the displacement map generated through Optical Flow. Figure 82 shows the stress in the *x* direction on layer-8. Figure 83 shows the stress in the *y* direction on layer-

8. Figure 84 shows the stress in the *x* direction on layer-4. Figure 85 shows the stress in the *y* direction on layer-4. The maximum and minimum stresses in the *x* direction were 5.6 kPa and -6.1 kPa. The maximum and minimum stress in the *y* direction were 5.6 kPa and -4.2 kPa.

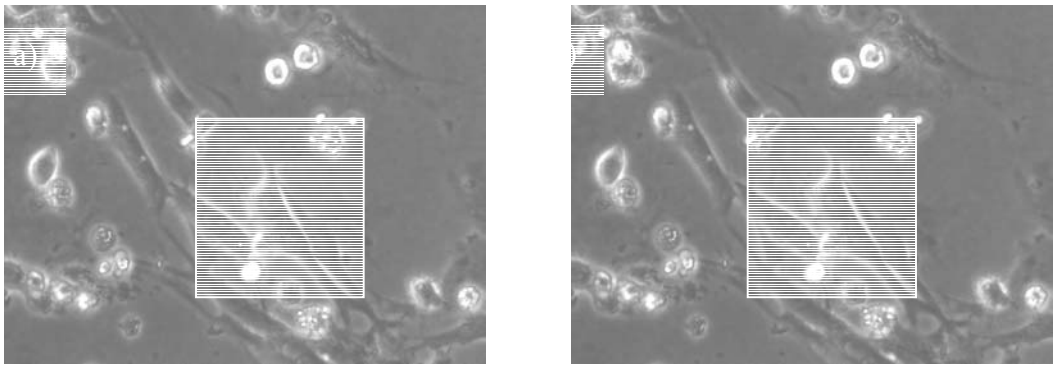

Figure 80. 40x Phase images of unaligned myocytes undergoing contraction
Two consecutive images taken from a time lapse with <1ms between images. The cell morphology is less phenotypic (rod-like) than cells in the aligned data sets (Figures 62, 68 and 74)

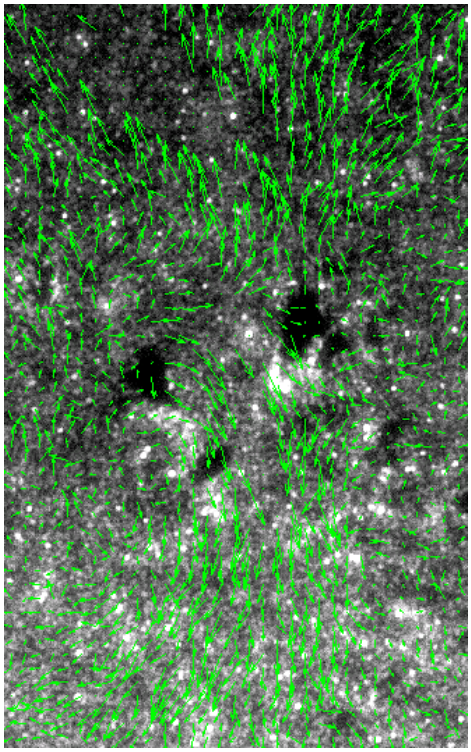

Figure 81. Fluorescent bead image masked with displacement data
The fluorescent image corresponds to the enclosed area in Figure 80a and uses green arrows to indicate the displacement of each node as defined in the program.

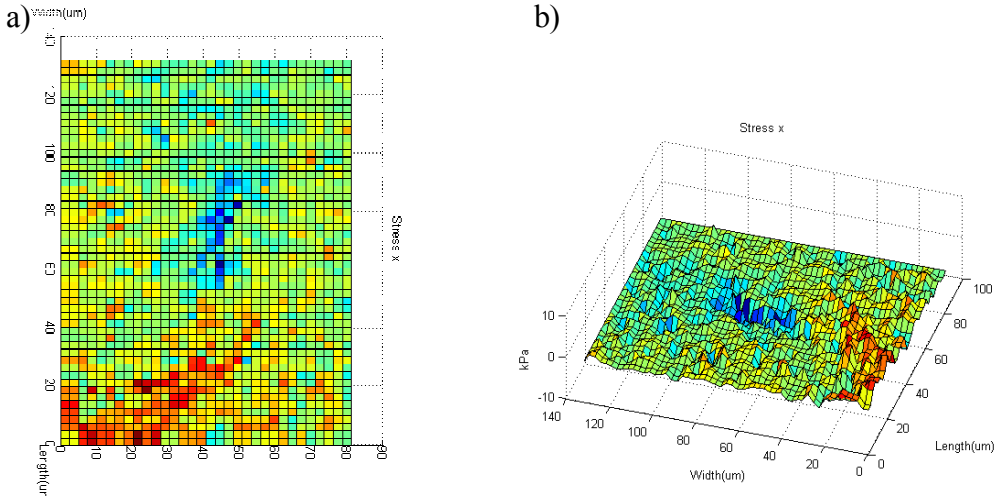

Figure 82. Stress maps of the stress in the *x* direction on layer-8
a) shows the 2D stress along layer-8 and b) shows the 3D stress along layer-8. The positive values indicate stress in the positive *x* direction and negative values indicate stress in the negative *x* direction.

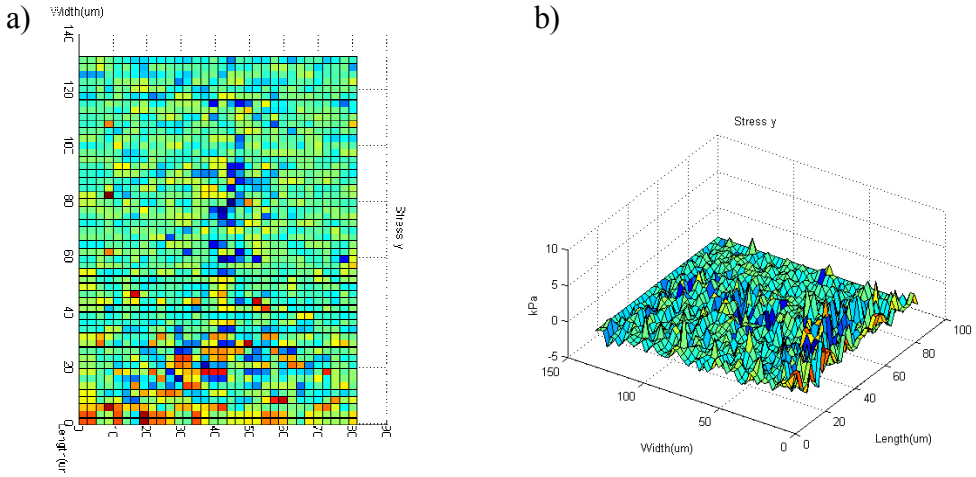

Figure 83. Stress maps of the stress in the *y* direction on layer-8
a) shows the 2D stress along layer-8 and b) shows the 3D stress along layer-8. The positive values indicate stress in the positive *y* direction and negative values indicate stress in the negative *y* direction.

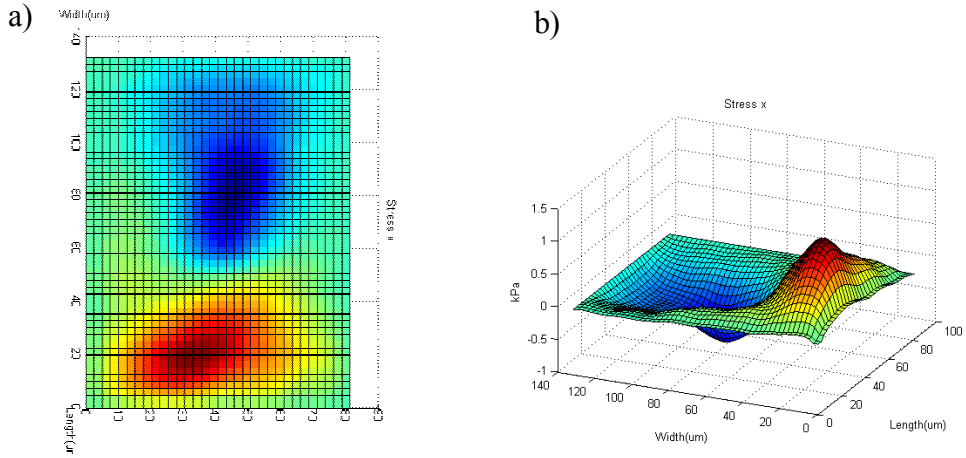

Figure 84. Stress maps of the stress in the *x* direction on layer-4
a) shows the 2D stress along layer-4 and b) shows the 3D stress along layer-4. The positive values indicate stress in the positive *x* direction and negative values indicate stress in the negative *x* direction.

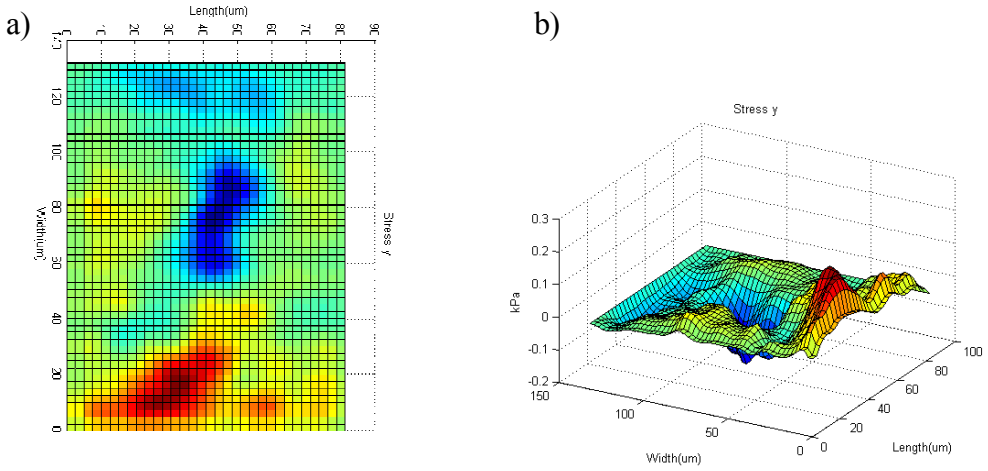

Figure 85. Stress maps of the stress in the *y* direction on layer-4
a) shows the 2D stress along layer-4 and b) shows the 3D stress along layer-4. The positive values indicate stress in the positive *y* direction and negative values indicate stress in the negative *y* direction.

6.II.B.5. Random Data Set 2

Figure 86 shows the two phase images of random cells under contraction. Figure 87 shows the displacement map generated through Optical Flow. Figure 88 shows the stress in the *x* direction on layer-8. Figure 89 shows the stress in the *y* direction on layer-8. Figure 90 shows the stress in the *x* direction on layer-4. Figure 91 shows the stress in

the *y* direction on layer-4. The maximum and minimum stresses in the *x* direction were 1230 kPa and -800 kPa. The maximum and minimum stress in the *y* direction were 1000 kPa and -565 kPa. Each of these measurements contained large point stresses that indicate a strong contraction; however, the strength of these points was not consistently represented along the edge of the cell.

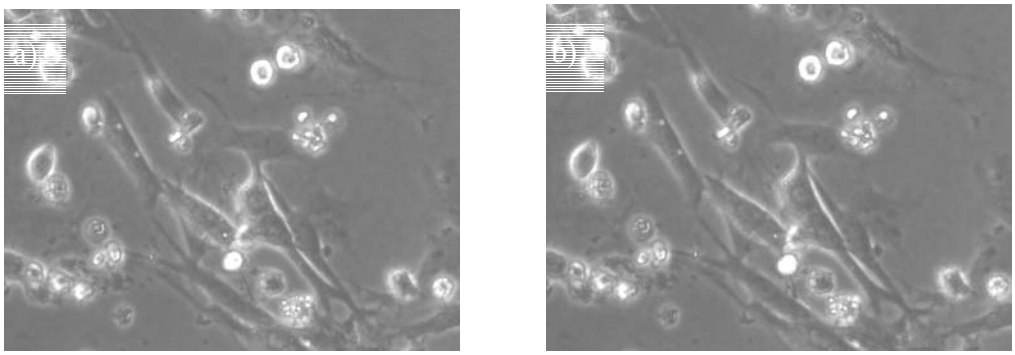

Figure 86. 40x Phase images of unaligned myocytes undergoing contraction
Two consecutive images taken from a time lapse with <1ms between images. The cell morphology is less phenotypic (rod-like) than cells in the aligned data sets (Figures 62, 68 and 74)

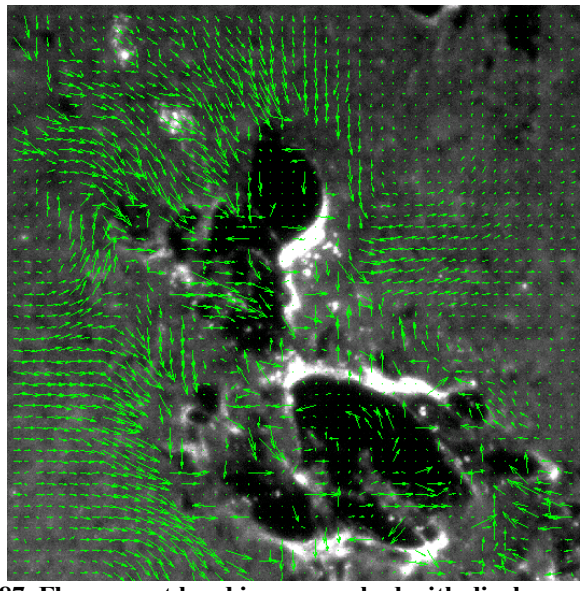

Figure 87. Fluorescent bead image masked with displacement data
The fluorescent image corresponds to the enclosed area in Figure 86a and uses green arrows to indicate the displacement of each node as defined in the program.

a)

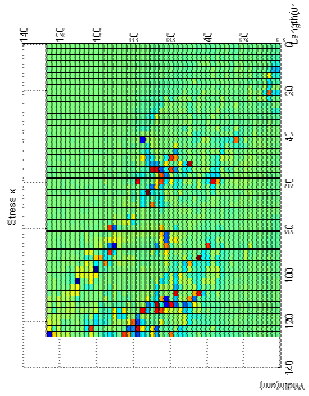

b)

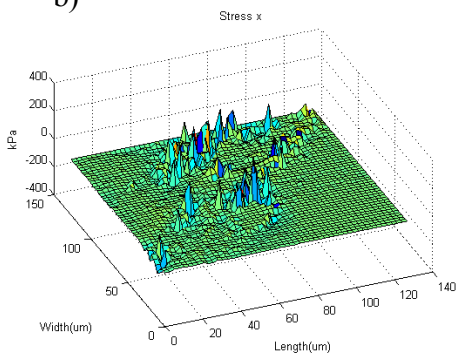

Figure 88. Stress maps of the stress in the *x* direction on layer-8
a) shows the 2D stress along layer-8 and b) shows the 3D stress along layer-8. The positive values indicate stress in the positive *x* direction and negative values indicate stress in the negative *x* direction. Notice the large point stresses along the left side of the graphs

a)

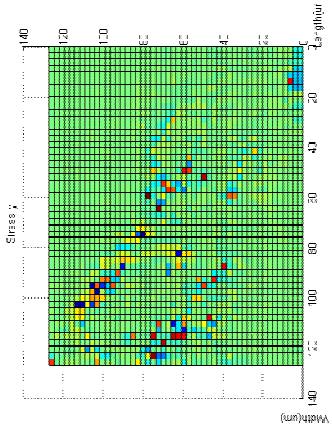

b)

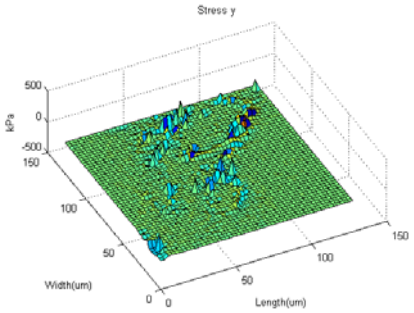

Figure 89. Stress maps of the stress in the *y* direction on layer-8
a) shows the 2D stress along layer-8 and b) shows the 3D stress along layer-8. The positive values indicate stress in the positive *y* direction and negative values indicate stress in the negative *y* direction. Notice the large point stresses along the left side of the graphs

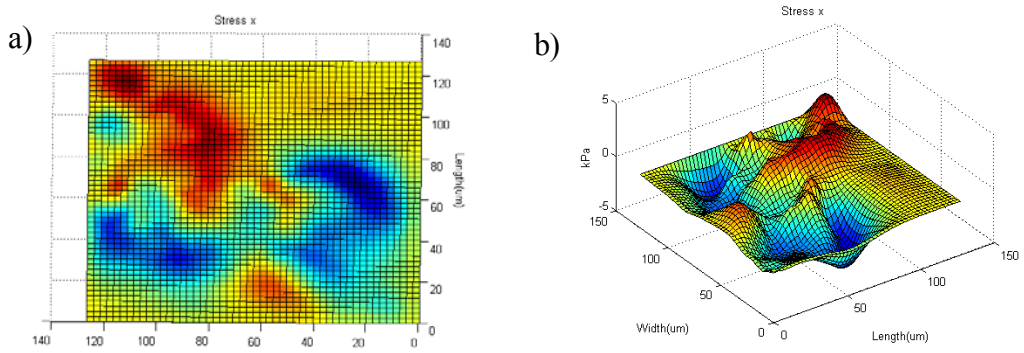

Figure 90. Stress maps of the stress in the *x* direction on layer-4
a) shows the 2D stress along layer-4 and b) shows the 3D stress along layer-4. The positive values indicate stress in the positive *x* direction and negative values indicate stress in the negative *x* direction.

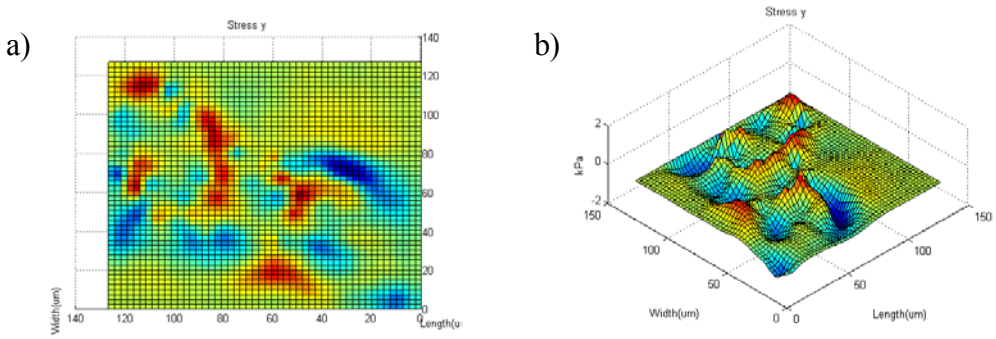

Figure 91. Stress maps of the stress in the *y* direction on layer-4
a) shows the 2D stress along layer-4 and b) shows the 3D stress along layer-4. The positive values indicate stress in the positive *y* direction and negative values indicate stress in the negative *y* direction.

6.II.B.6. Random Data Set 3

Figure 92 shows the two phase images of random cells under contraction. Figure 93 shows the displacement map generated through Optical Flow. Figure 94 shows the stress in the *x* direction on layer-8. Figure 95 shows the stress in the *y* direction on layer-8. Figure 96 shows the stress in the *x* direction on layer-4. Figure 97 shows the stress in the *y* direction on layer-4. The maximum and minimum stresses in the *x* direction were 420 kPa and -395 kPa. The maximum and minimum stress in the *y* direction were 345 kPa and -335 kPa.

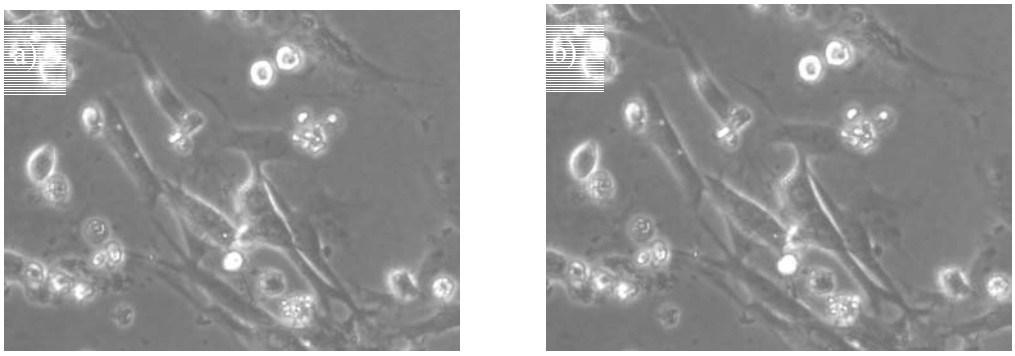

Figure 92. 40x Phase images of unaligned myocytes undergoing contraction
Two consecutive images taken from a time lapse with <1ms between images. The cell morphology is less phenotypic (rod-like) than cells in the aligned data sets (Figures 62, 68 and 74)

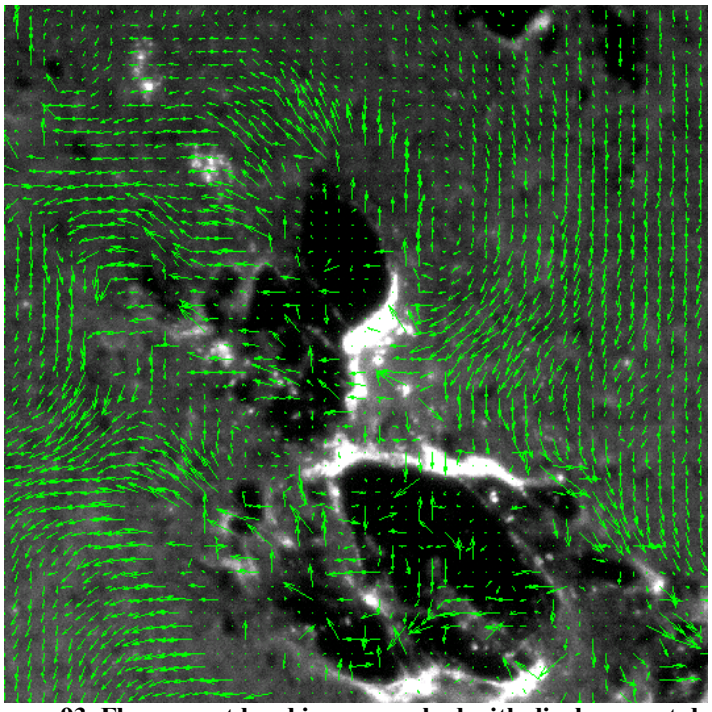

Figure 93. Fluorescent bead image masked with displacement data
The fluorescent image corresponds to the enclosed area in Figure 92a and uses green arrows to indicate the displacement of each node as defined in the program.

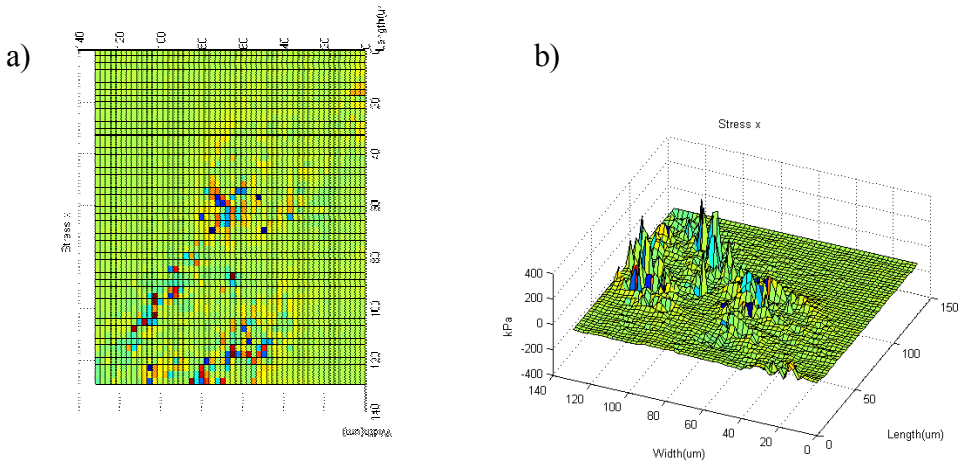

Figure 94. Stress maps of the stress in the *x* direction on layer-8
a) shows the 2D stress along layer-8 and b) shows the 3D stress along layer-8. The positive values indicate stress in the positive *x* direction and negative values indicate stress in the negative *x* direction. Notice the large point stresses.

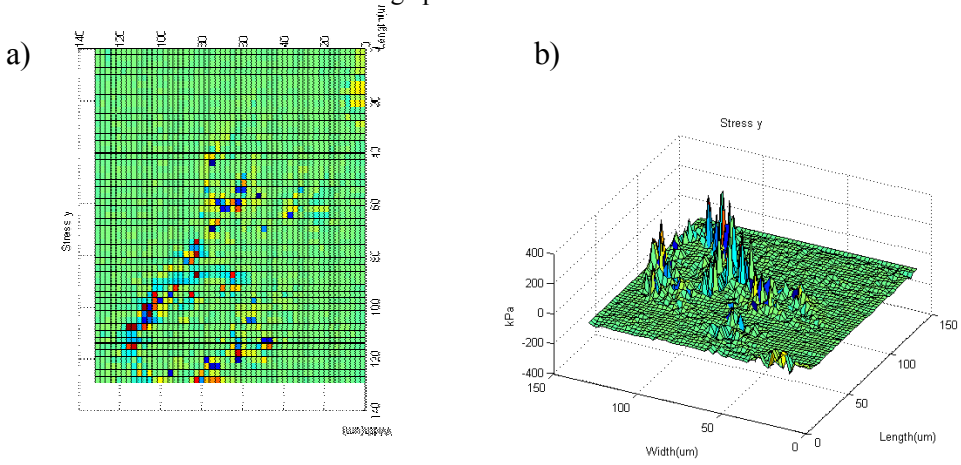

Figure 95. Stress maps of the stress in the *y* direction on layer-8
a) shows the 2D stress along layer-8 and b) shows the 3D stress along layer-8. The positive values indicate stress in the positive *y* direction and negative values indicate stress in the negative *y* direction. Notice the large point stresses.

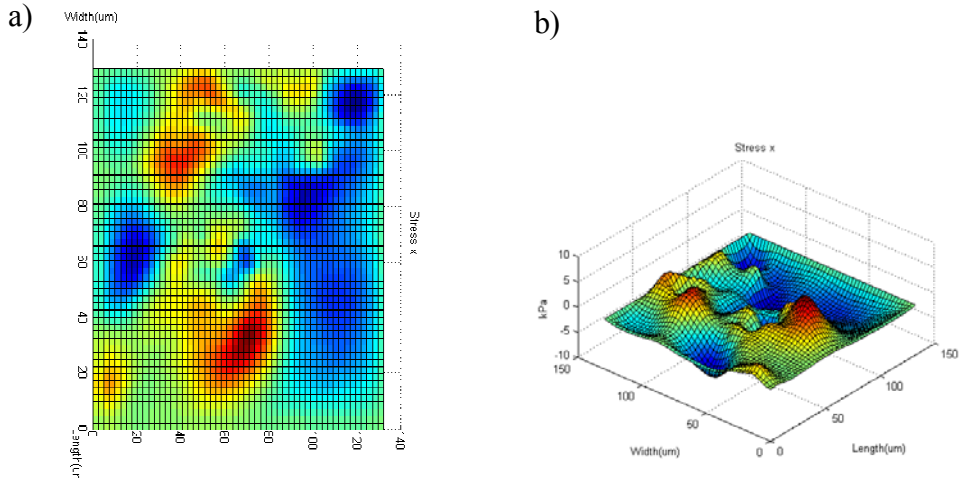

Figure 96. Stress maps of the stress in the *x* direction on layer-4
a) shows the 2D stress along layer-4 and b) shows the 3D stress along layer-4. The positive values indicate stress in the positive *x* direction and negative values indicate stress in the negative *x* direction.

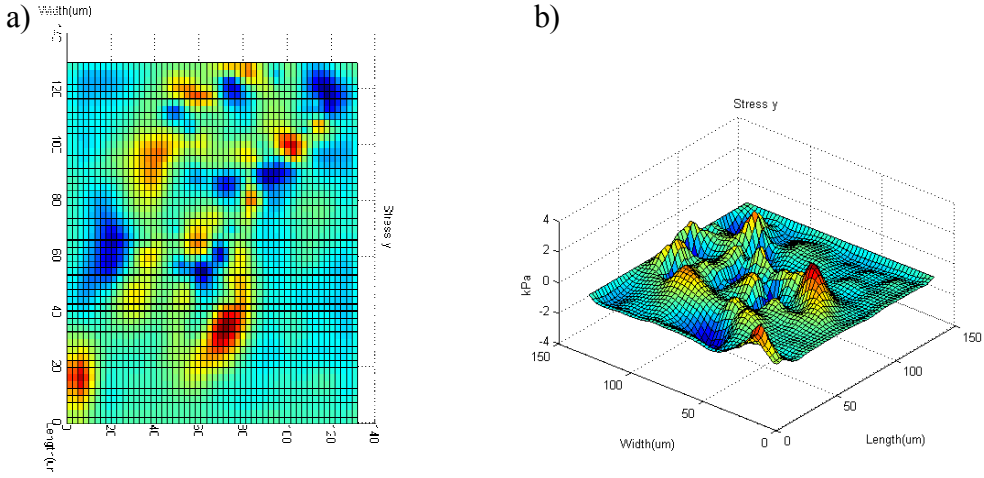

Figure 97. Stress maps of the stress in the *y* direction on layer-4
a) shows the 2D stress along layer-4 and b) shows the 3D stress along layer-4. The positive values indicate stress in the positive *y* direction and negative values indicate stress in the negative *y* direction.

6.II.C. 7 kPa Acrylamide Gels

6.II.C.1. Aligned Data Set 1

Figure 98 shows the two phase images of aligned cells under contraction. All images are taken with a 40x objective and are 220 μm *x* 166 μm in size. Figure 99 shows the displacement map generated through Optical Flow. Figure 100 shows the stress in the *x* direction on layer-8. Figure 101 shows the stress in the *y* direction on layer-8. Figure 102 shows the stress in the *x* direction on layer-4. Figure 103 shows the stress in the *y* direction on layer-4. The maximum and minimum stresses in the *x* direction were 100 kPa and -107 kPa. The maximum and minimum stress in the *y* direction were 100 kPa and -85 kPa.

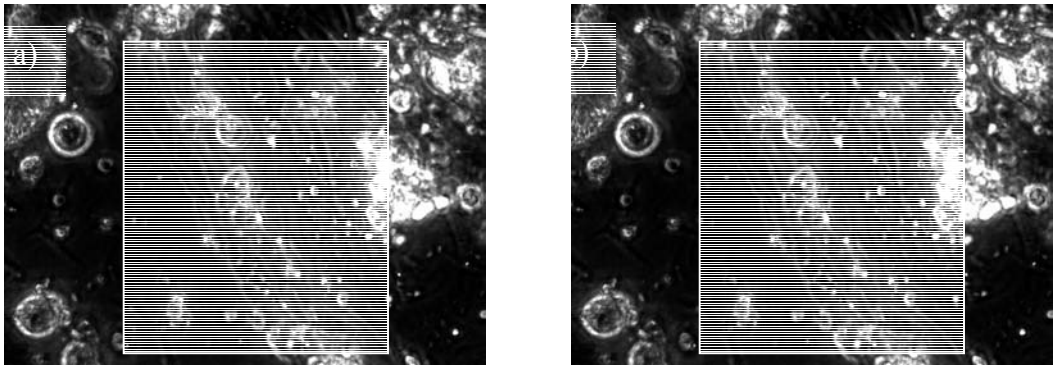

Figure 98. 40x Phase images of aligned myocytes undergoing contraction
Two consecutive images taken from a time lapse with <1ms between images. Debris can be seen on top of the cell culture; however, myocytes are aligned underneath.

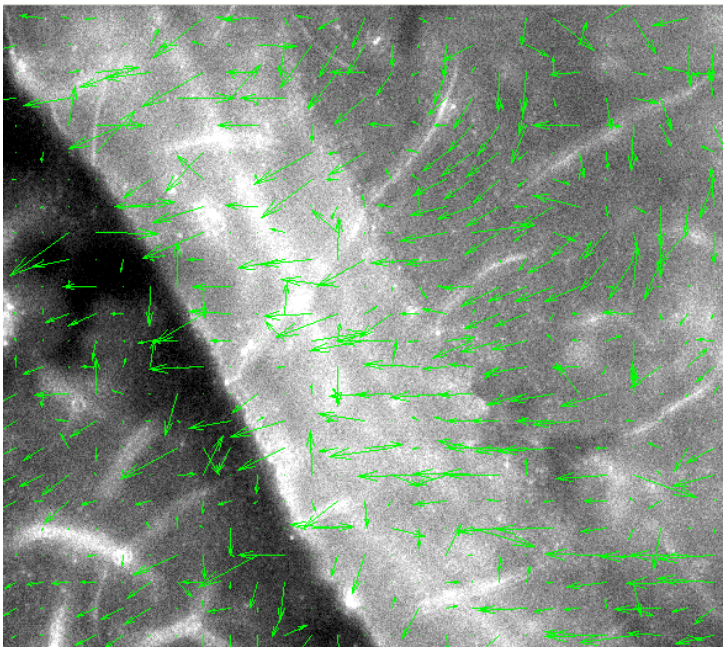

Figure 99. Fluorescent bead image masked with displacement data
The fluorescent image corresponds to the enclosed area in Figure 98a and uses green arrows to indicate the displacement of each node as defined in the program.

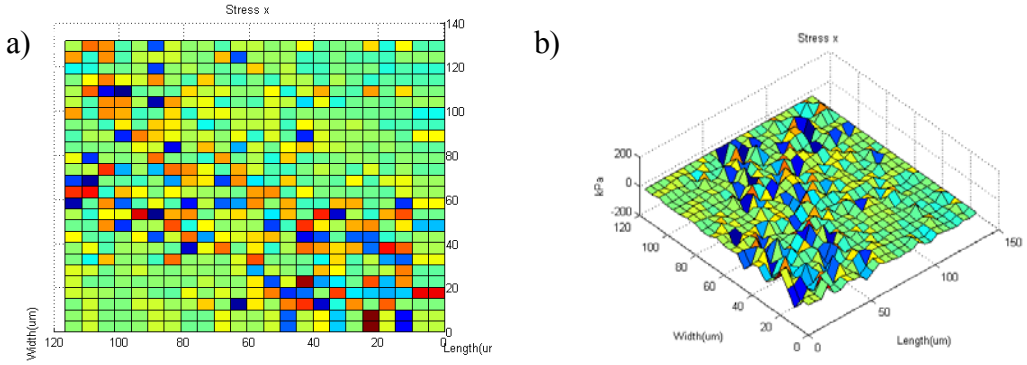

Figure 100. Stress maps of the stress in the *x* direction on layer-8
a) shows the 2D stress along layer-8 and b) shows the 3D stress along layer-8. The positive values indicate stress in the positive *x* direction and negative values indicate stress in the negative *x* direction.

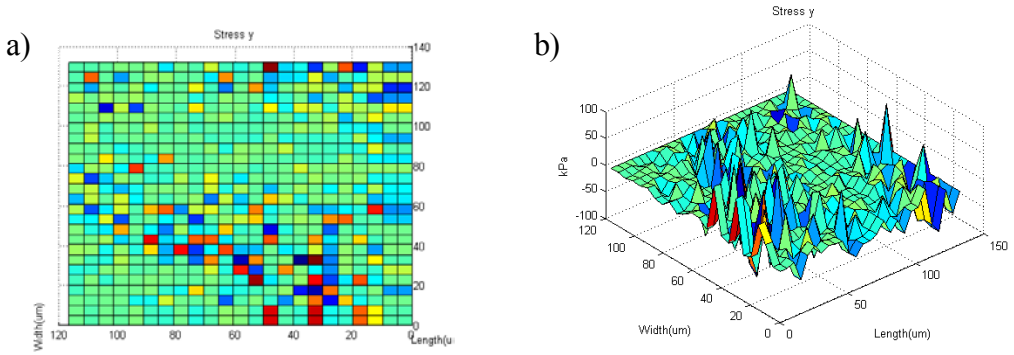

Figure 101. Stress maps of the stress in the *y* direction on layer-8
a) shows the 2D stress along layer-8 and b) shows the 3D stress along layer-8. The positive values indicate stress in the positive *y* direction and negative values indicate stress in the negative *y* direction.

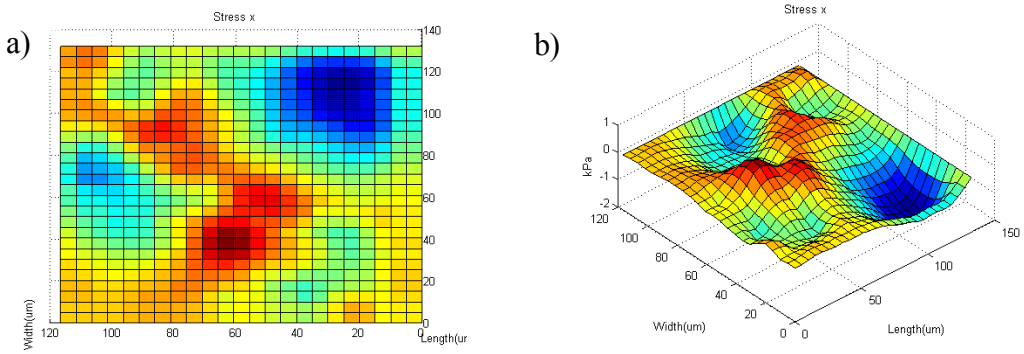

Figure 102. Stress maps of the stress in the *x* direction on layer-4
a) shows the 2D stress along layer-4 and b) shows the 3D stress along layer-4. The positive values indicate stress in the positive *x* direction and negative values indicate stress in the negative *x* direction.

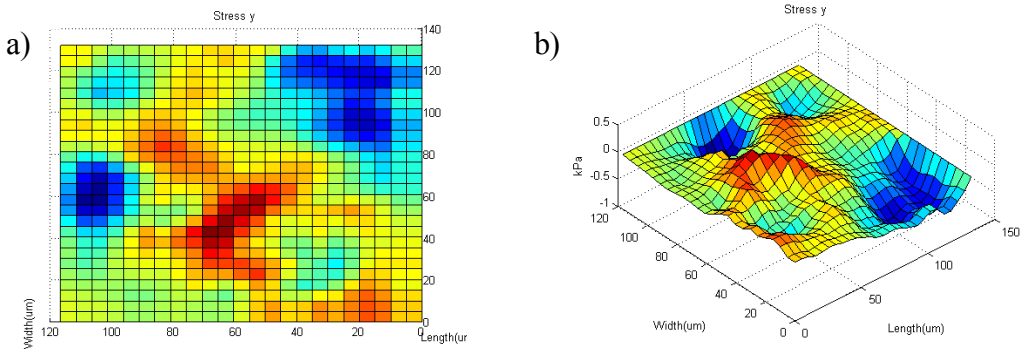

Figure 103. Stress maps of the stress in the *y* direction on layer-4
a) shows the 2D stress along layer-4 and b) shows the 3D stress along layer-4. The positive values indicate stress in the positive *y* direction and negative values indicate stress in the negative *y* direction.

6.II.C.2. Aligned Data Set 2

Figure 104 shows the two phase images of aligned cells under contraction (similar to Figure 98 but different time points in time lapse set). For the following images, consider them to be mirrored across the *y* axis. Figure 105 shows the displacement map generated through Optical Flow. Figure 106 shows the stress in the *x* direction on layer-8. Figure 107 shows the stress in the *y* direction on layer-8. Figure 108 shows the stress in the *x* direction on layer-4. Figure 109 shows the stress in the *y* direction on layer-4. The maximum and minimum stresses in the *x* direction were 80 kPa and -43 kPa. The maximum and minimum stress in the *y* direction were 50 kPa and -91 kPa.

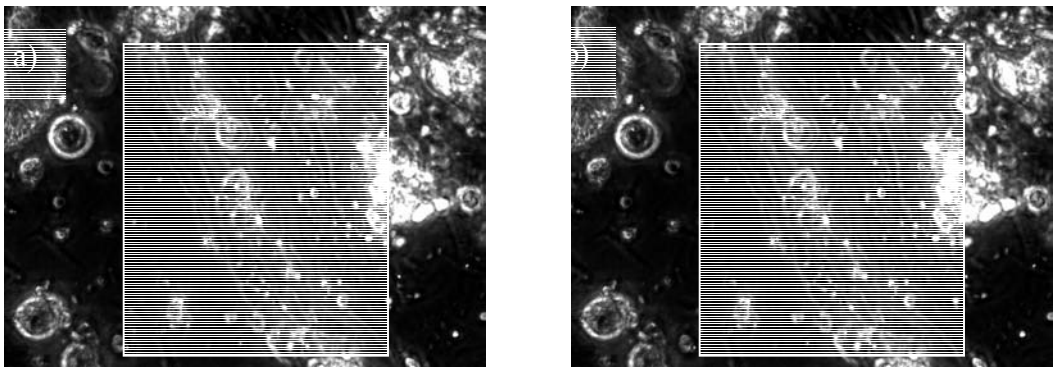

Figure 104. 40x Phase images of aligned myocytes undergoing contraction
Two consecutive images taken from a time lapse with <1ms between images. Debris can be seen on top of the cell culture; however, myocytes are aligned underneath.

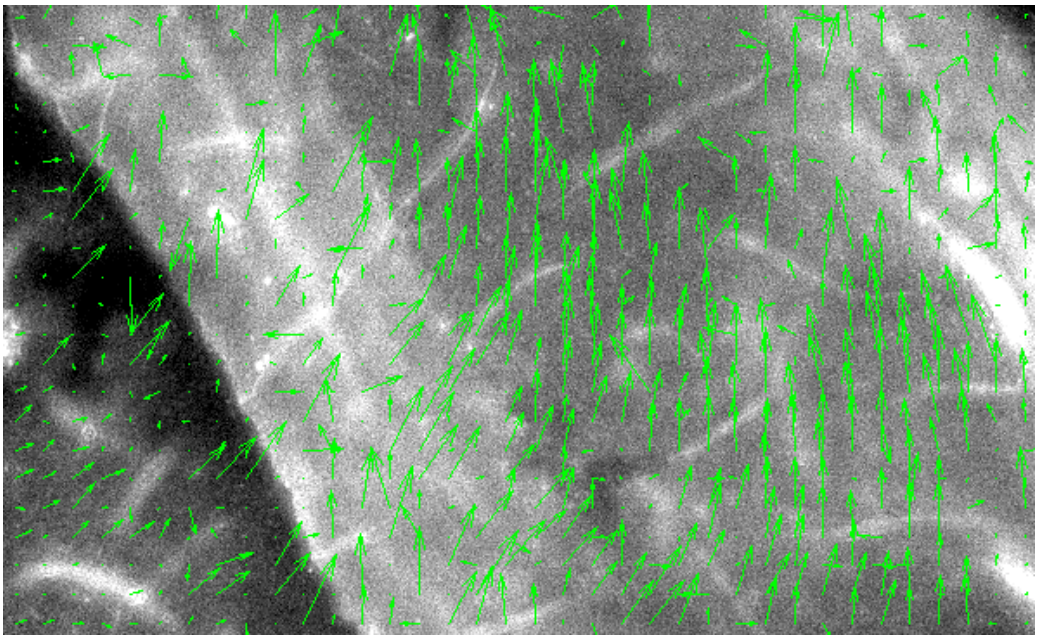

Figure 105. Fluorescent bead image masked with displacement data
The fluorescent image corresponds to the enclosed area in Figure 104a and uses green arrows to indicate the displacement of each node as defined in the program.

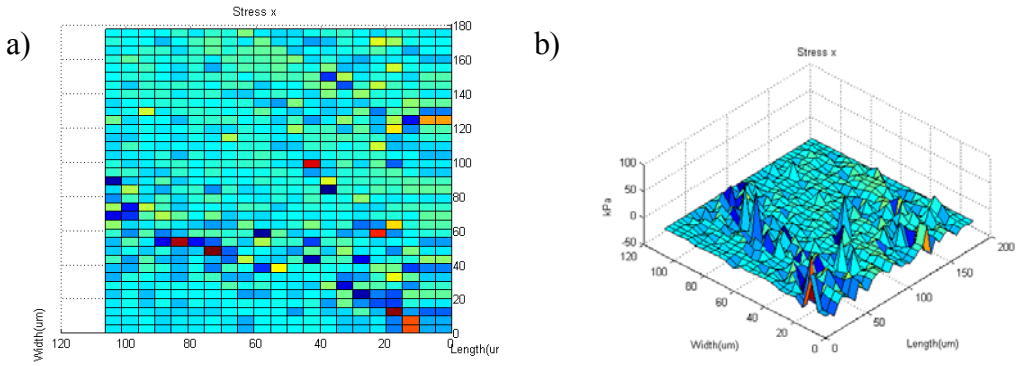

Figure 106. Stress maps of the stress in the *x* direction on layer-8
a) shows the 2D stress along layer-8 and b) shows the 3D stress along layer-8. The positive values indicate stress in the positive *x* direction and negative values indicate stress in the negative *x* direction.

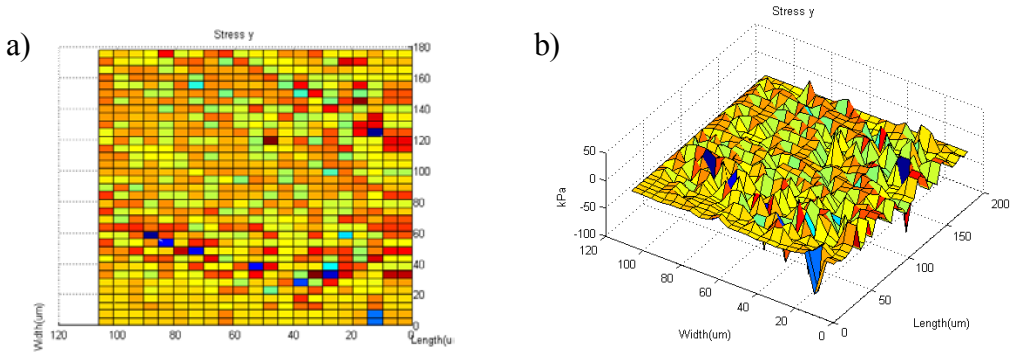

Figure 107. Stress maps of the stress in the *y* direction on layer-8
a) shows the 2D stress along layer-8 and b) shows the 3D stress along layer-8. The positive values indicate stress in the positive *y* direction and negative values indicate stress in the negative *y* direction.

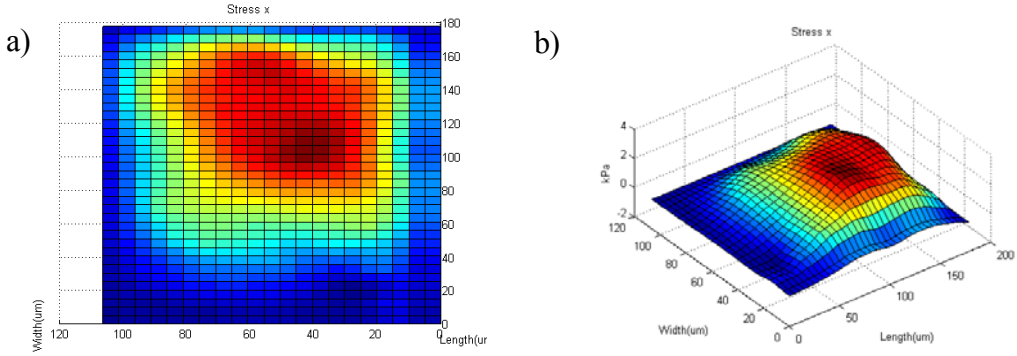

Figure 108. Stress maps of the stress in the *x* direction on layer-4
a) shows the 2D stress along layer-4 and b) shows the 3D stress along layer-4. The positive values indicate stress in the positive *x* direction and negative values indicate stress in the negative *x* direction.

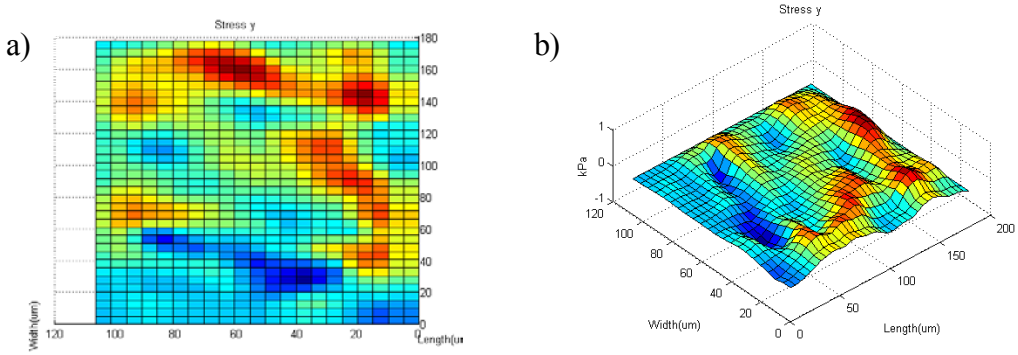

Figure 109. Stress maps of the stress in the *y* direction on layer-4
a) shows the 2D stress along layer-4 and b) shows the 3D stress along layer-4. The positive values indicate stress in the positive *y* direction and negative values indicate stress in the negative *y* direction.

6.II.C.3. Aligned Data Set 3

Figure 110 shows the two phase images of aligned cells under contraction (similar to Figure 98 but different time points in time lapse set). For the following images, consider them to be mirrored across the *y* axis. Figure 111 shows the displacement map generated through Optical Flow. Figure 112 shows the stress in the *x* direction on layer-8. Figure 113 shows the stress in the *y* direction on layer-8. Figure 114 shows the stress in the *x* direction on layer-4. Figure 115 shows the stress in the *y* direction on layer-4. The maximum and minimum stresses in the *x* direction were 210 kPa and -205 kPa. The maximum and minimum stress in the *y* direction were 197 kPa and -249 kPa.

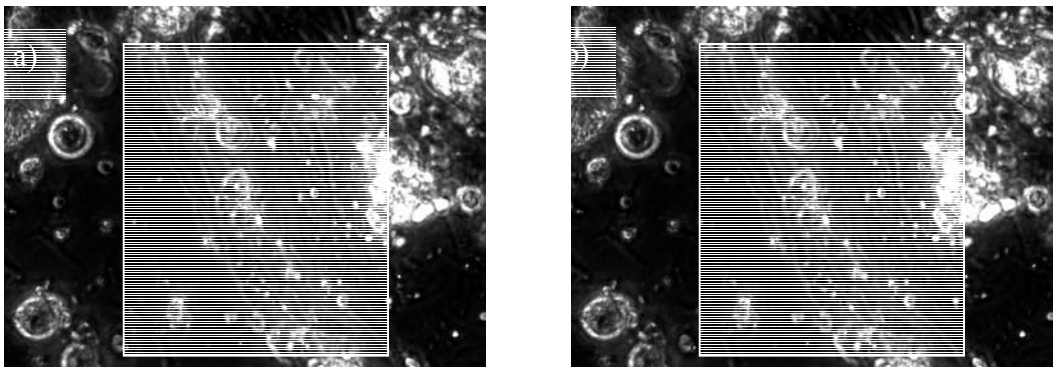

Figure 110. 40x Phase images of aligned myocytes undergoing contraction
Two consecutive images taken from a time lapse with <1ms between images. Debris can be seen on top of the cell culture; however, myocytes are aligned underneath.

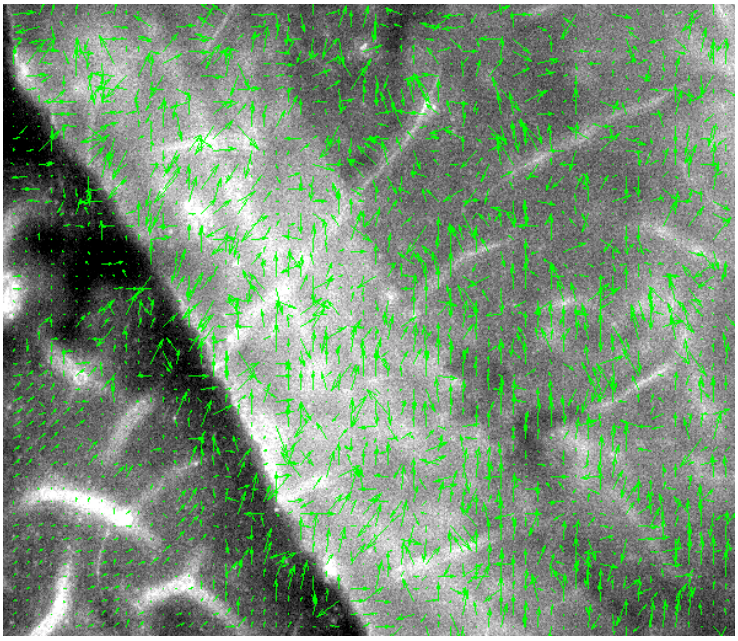

Figure 111. Fluorescent bead image masked with displacement data
The fluorescent image corresponds to the enclosed area in Figure 112a and uses green arrows to indicate the displacement of each node as defined in the program.

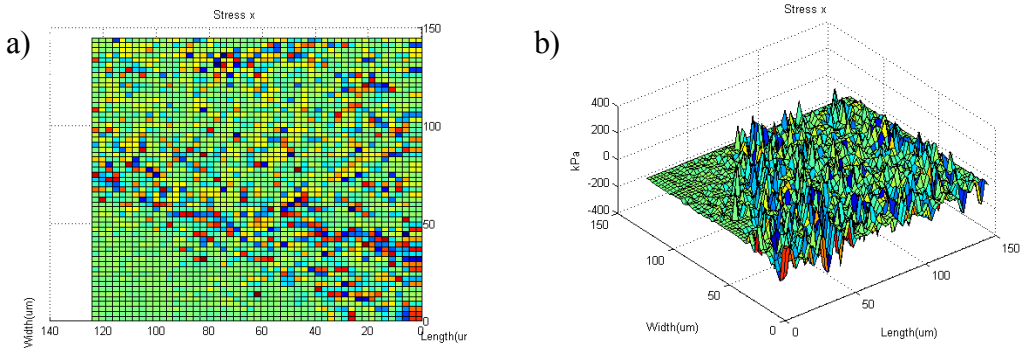

Figure 112. Stress maps of the stress in the *x* direction on layer-8
a) shows the 2D stress along layer-8 and b) shows the 3D stress along layer-8. The positive values indicate stress in the positive *x* direction and negative values indicate stress in the negative *x* direction.

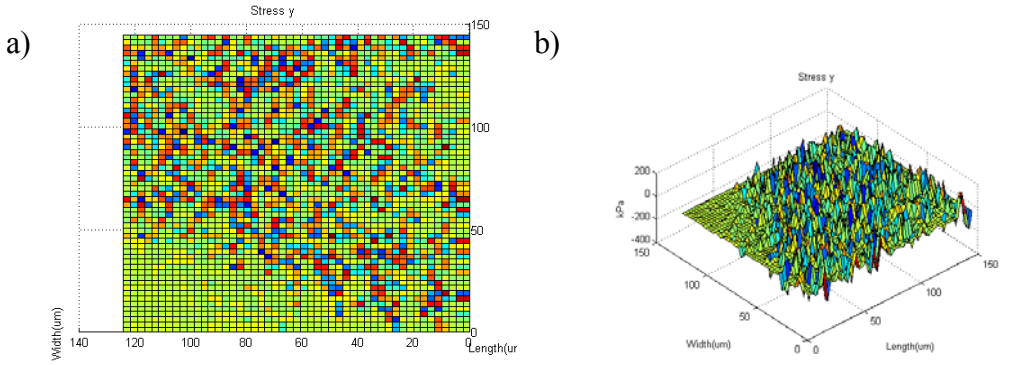

Figure 113. Stress maps of the stress in the *y* direction on layer-8
a) shows the 2D stress along layer-8 and b) shows the 3D stress along layer-8. The positive values indicate stress in the positive *y* direction and negative values indicate stress in the negative *y* direction.

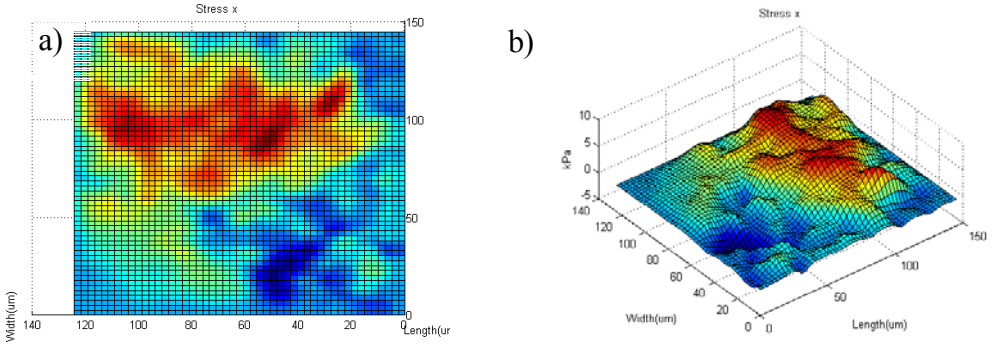

Figure 114. Stress maps of the stress in the *x* direction on layer-4
a) shows the 2D stress along layer-4 and b) shows the 3D stress along layer-4. The positive values indicate stress in the positive *x* direction and negative values indicate stress in the negative *x* direction.

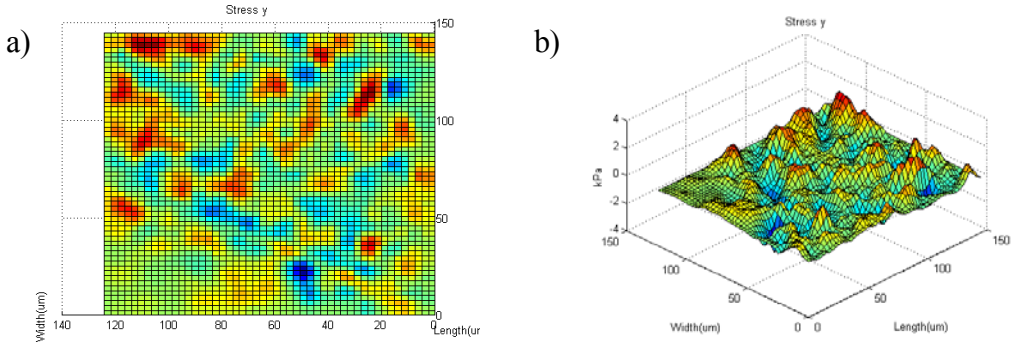

Figure 115. Stress maps of the stress in the *y* direction on layer-4
a) shows the 2D stress along layer-4 and b) shows the 3D stress along layer-4. The positive values indicate stress in the positive *y* direction and negative values indicate stress in the negative *y* direction.

6.II.C.4. Random Data Set 1

Figure 116 shows the two phase images of random cells under contraction. Figure 117 shows the displacement map generated through Optical Flow. Figure 118 shows the stress in the *x* direction on layer-8. Figure 119 shows the stress in the *y* direction on layer-8. Figure 120 shows the stress in the *x* direction on layer-4. Figure 121 shows the stress in the *y* direction on layer-4. The maximum and minimum stresses in the *x* direction were 75 kPa and -150 kPa. The maximum and minimum stress in the *y* direction were 185 kPa and -205 kPa.

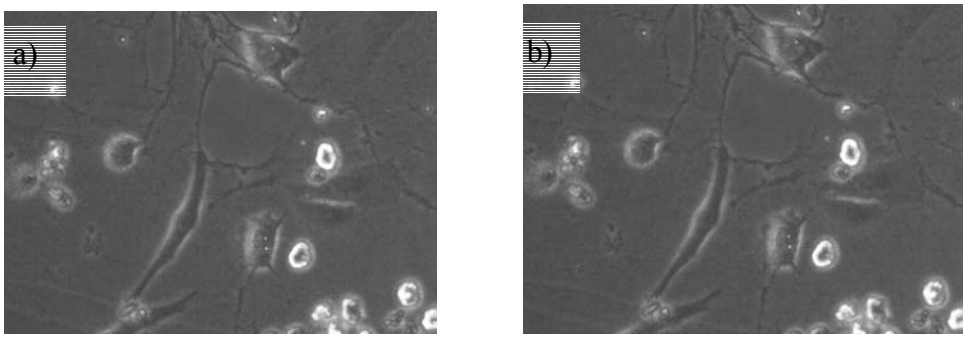

Figure 116. 40x Phase images of unaligned myocytes undergoing contraction
Two consecutive images taken from a time lapse with <1ms between images. The cell morphology is less phenotypic (rod-like) than cells in the aligned data sets (Figures 98, 104 and 110)

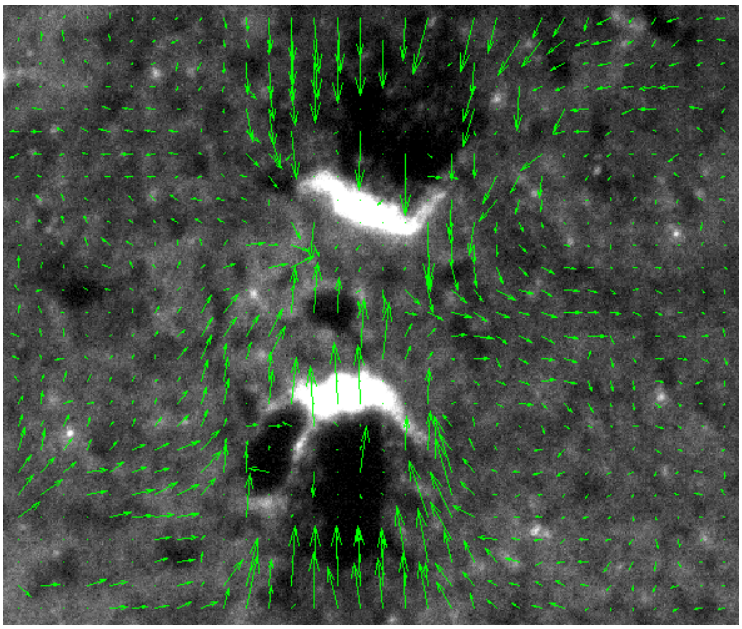

Figure 117. Fluorescent bead image masked with displacement data
The fluorescent image corresponds to the enclosed area in Figure 118a and uses green arrows to indicate the displacement of each node as defined in the program.

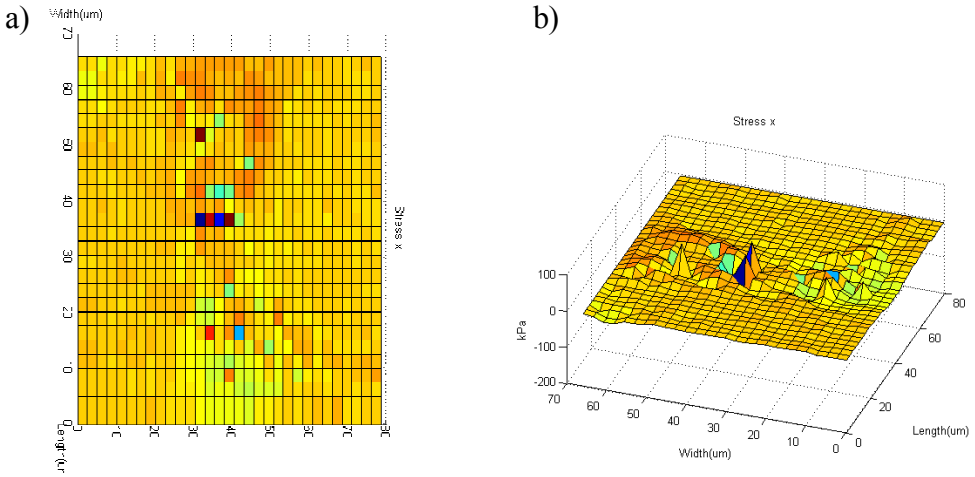

Figure 118. Stress maps of the stress in the *x* direction on layer-8
a) shows the 2D stress along layer-8 and b) shows the 3D stress along layer-8. The positive values indicate stress in the positive *x* direction and negative values indicate stress in the negative *x* direction.

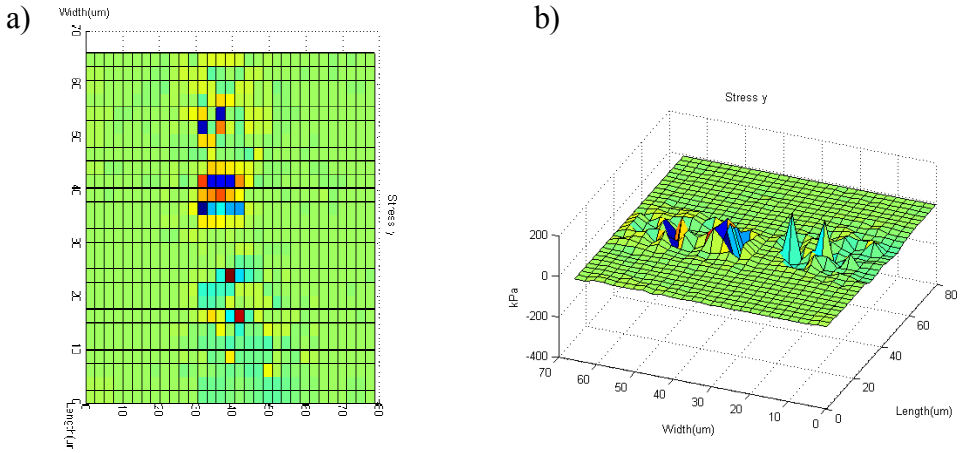

Figure 119. Stress maps of the stress in the *y* direction on layer-8
a) shows the 2D stress along layer-8 and b) shows the 3D stress along layer-8. The positive values indicate stress in the positive *y* direction and negative values indicate stress in the negative *y* direction.

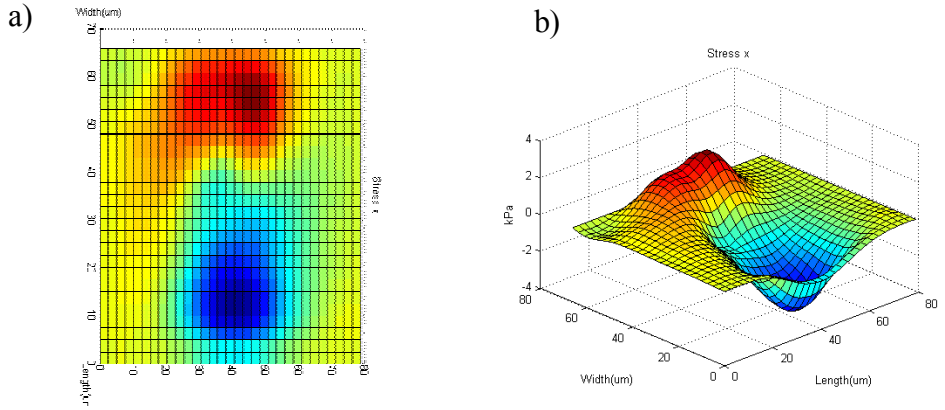

Figure 120. Stress maps of the stress in the *x* direction on layer-4
a) shows the 2D stress along layer-4 and b) shows the 3D stress along layer-4. The positive values indicate stress in the positive *x* direction and negative values indicate stress in the negative *x* direction.

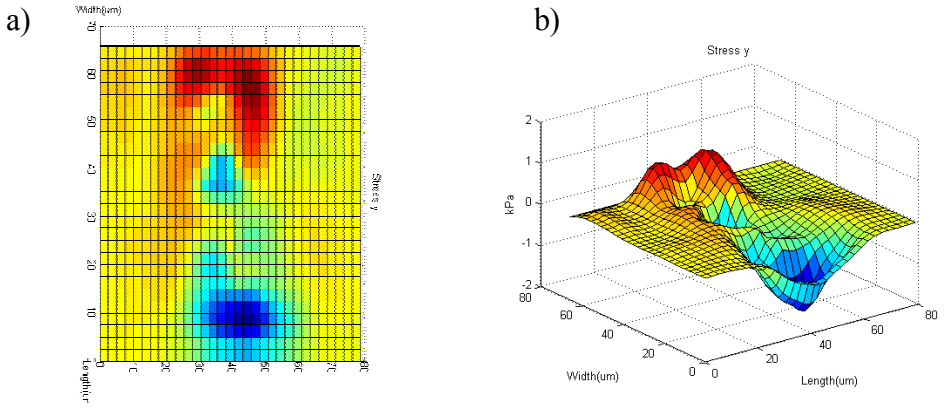

Figure 121. Stress maps of the stress in the *y* direction on layer-4
a) shows the 2D stress along layer-4 and b) shows the 3D stress along layer-4. The positive values indicate stress in the positive *y* direction and negative values indicate stress in the negative *y* direction.

6.II.C.5. Random Data Set 2

Figure 122 shows the two phase images of random cells under contraction. Figure 123 shows the displacement map generated through Optical Flow. Figure 124 shows the stress in the *x* direction on layer-8. Figure 125 shows the stress in the *y* direction on layer-8. Figure 126 shows the stress in the *x* direction on layer-4. Figure 127 shows the stress in the *y* direction on layer-4. The maximum and minimum stresses in the *x* direction were 190 kPa and -190 kPa. The maximum and minimum stress in the *y* direction were 57 kPa and -125 kPa.

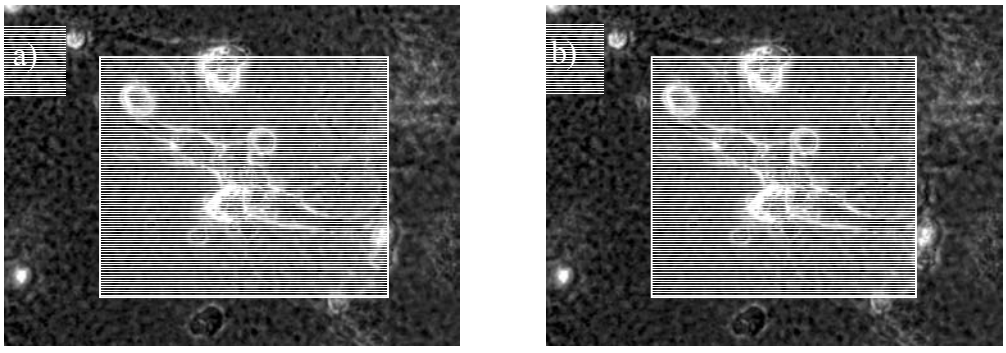

Figure 122. 40x Phase images of unaligned myocytes undergoing contraction
Two consecutive images taken from a time lapse with <1ms between images. The cell morphology is less phenotypic (rod-like) than cells in the aligned data sets (Figures 98, 104 and 110)

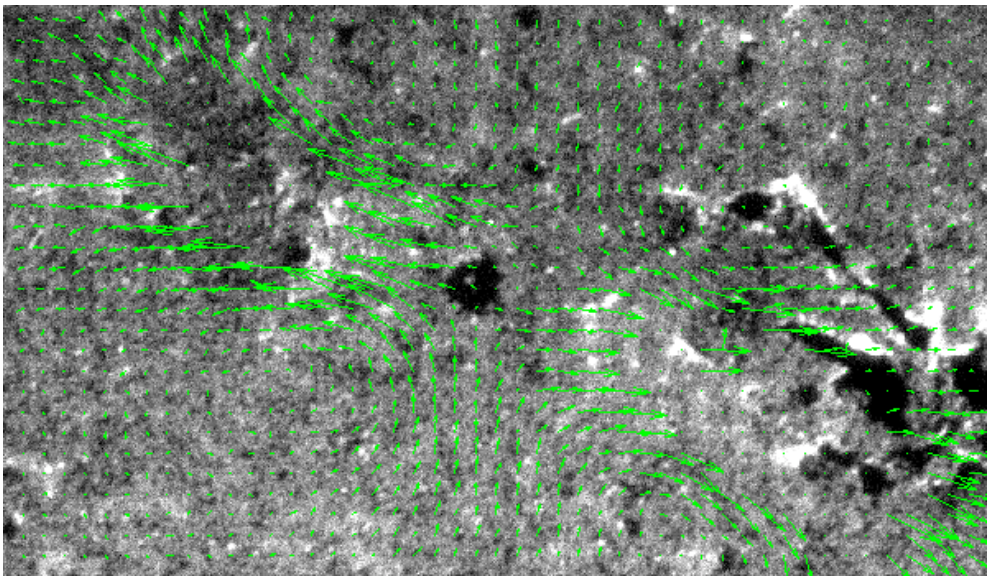

Figure 123. Fluorescent bead image masked with displacement data
The fluorescent image corresponds to the enclosed area in Figure 122a and uses green arrows to indicate the displacement of each node as defined in the program.

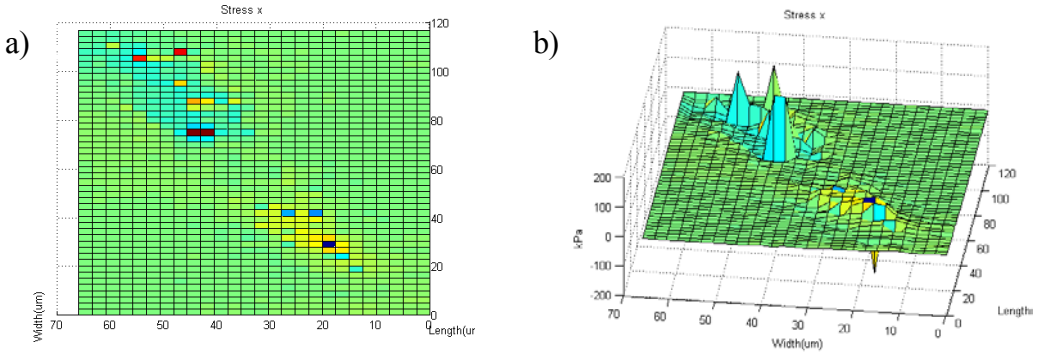

Figure 124. Stress maps of the stress in the *x* direction on layer-8
a) shows the 2D stress along layer-8 and b) shows the 3D stress along layer-8. The positive values indicate stress in the positive *x* direction and negative values indicate stress in the negative *x* direction. Notice the large point stresses along the left side of the graphs

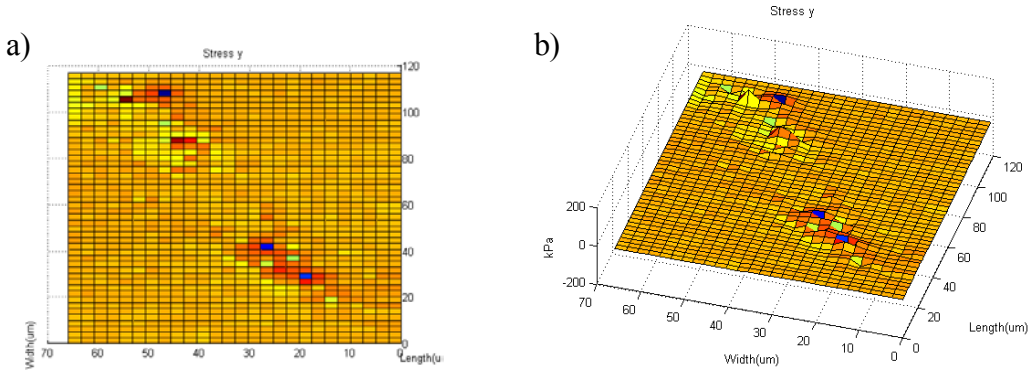

Figure 125. Stress maps of the stress in the *y* direction on layer-8
a) shows the 2D stress along layer-8 and b) shows the 3D stress along layer-8. The positive values indicate stress in the positive *y* direction and negative values indicate stress in the negative *y* direction. Notice the large point stresses along the left side of the graphs

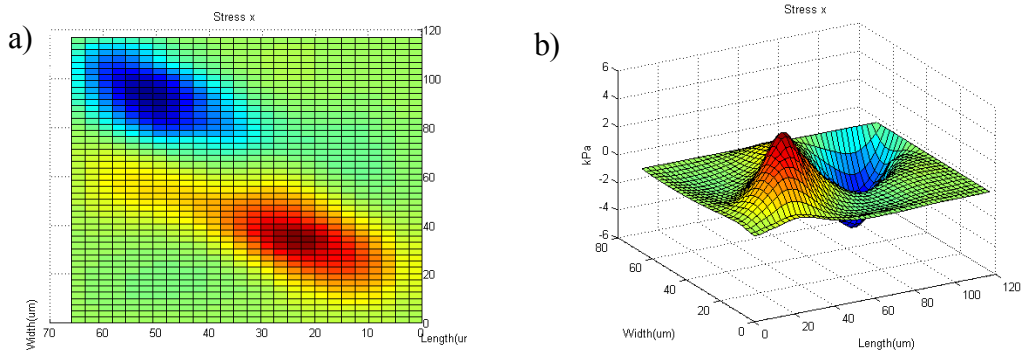

Figure 126. Stress maps of the stress in the *x* direction on layer-4
a) shows the 2D stress along layer-4 and b) shows the 3D stress along layer-4. The positive values indicate stress in the positive *x* direction and negative values indicate stress in the negative *x* direction.

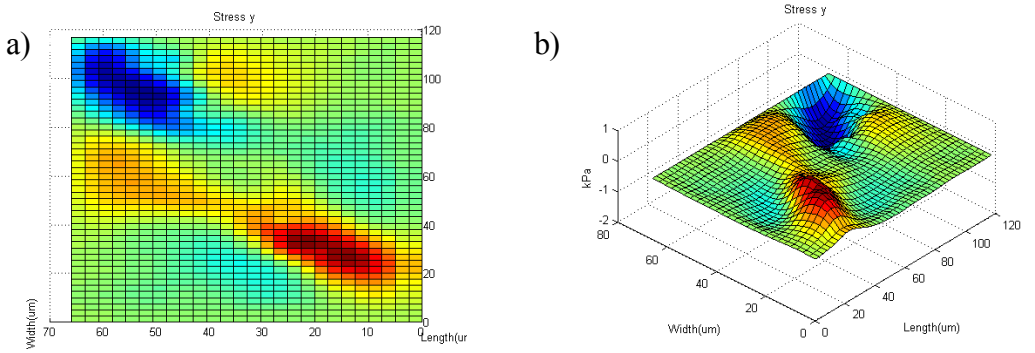

Figure 127. Stress maps of the stress in the *y* direction on layer-4
a) shows the 2D stress along layer-4 and b) shows the 3D stress along layer-4. The positive values indicate stress in the positive *y* direction and negative values indicate stress in the negative *y* direction.

6.II.C.6. Random Data Set 3

Figure 128 shows the two phase images of random cells under contraction. Figure 129 shows the displacement map generated through Optical Flow. Figure 130 shows the stress in the *x* direction on layer-8. Figure 131 shows the stress in the *y* direction on layer-8. Figure 132 shows the stress in the *x* direction on layer-4. Figure 133 shows the stress in the *y* direction on layer-4. The maximum and minimum stresses in the *x* direction were 230 kPa and -190 kPa. The maximum and minimum stress in the *y* direction were 110 kPa and -35 kPa.

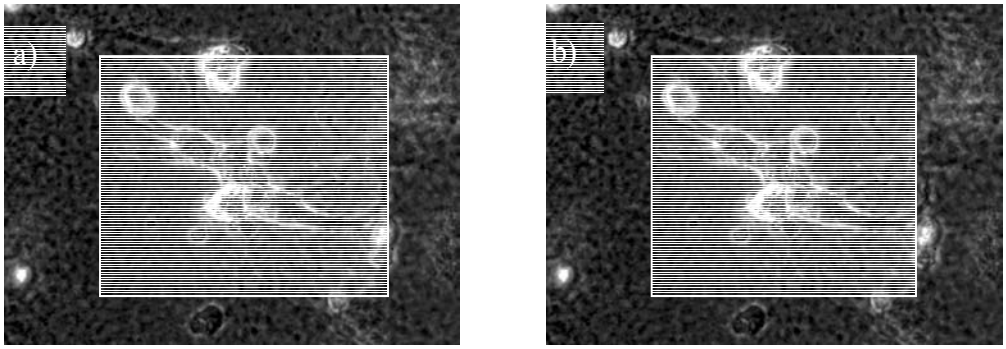

Figure 128. 40x Phase images of unaligned myocytes undergoing contraction
Two consecutive images taken from a time lapse with <1ms between images. The cell morphology is less phenotypic (rod-like) than cells in the aligned data sets (Figures 98, 104 and 110)

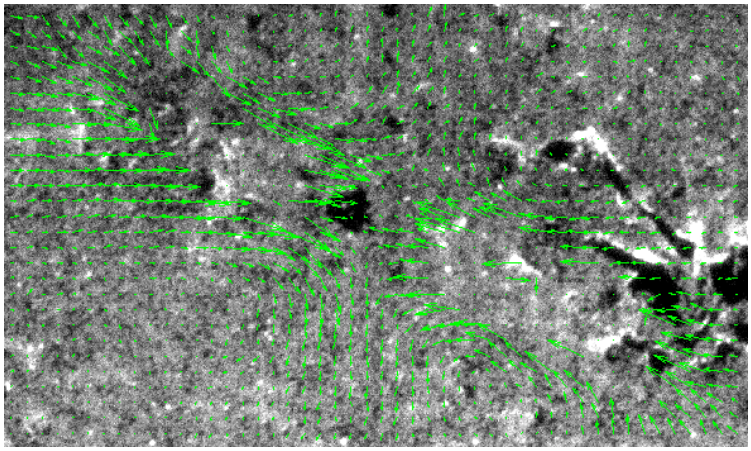

Figure 129. Fluorescent bead image masked with displacement data
The fluorescent image corresponds to the enclosed area in Figure 128a and uses green arrows to indicate the displacement of each node as defined in the program.

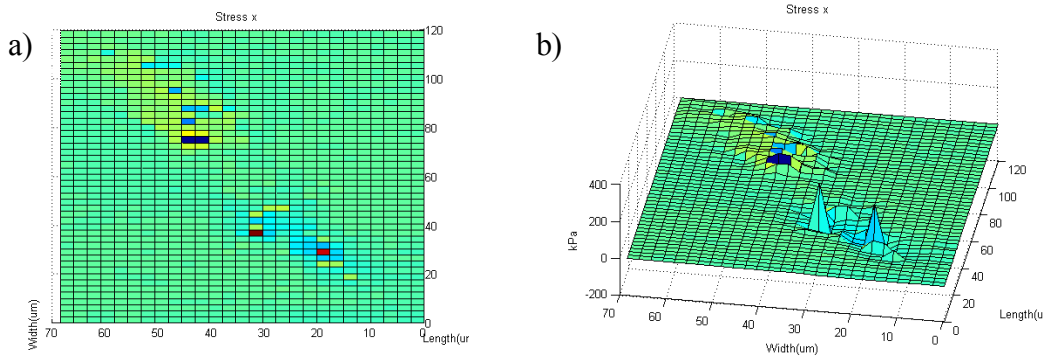

Figure 130. Stress maps of the stress in the *x* direction on layer-8
a) shows the 2D stress along layer-8 and b) shows the 3D stress along layer-8. The positive values indicate stress in the positive *x* direction and negative values indicate stress in the negative *x* direction. Notice the large point stresses.

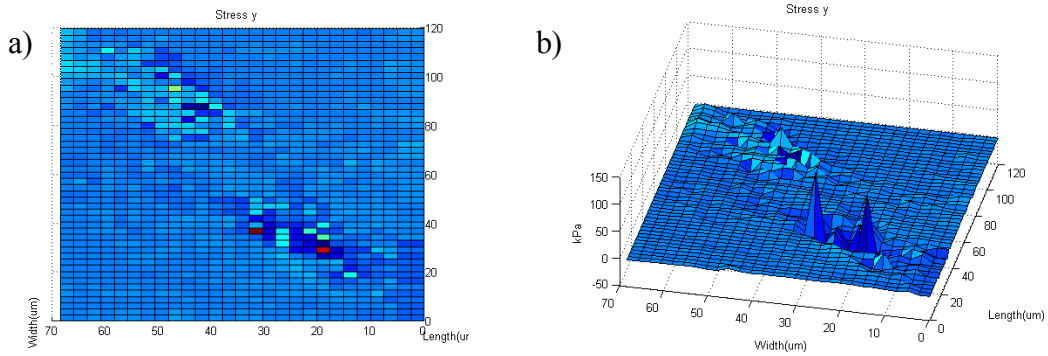

Figure 131. Stress maps of the stress in the *y* direction on layer-8
a) shows the 2D stress along layer-8 and b) shows the 3D stress along layer-8. The positive values indicate stress in the positive *y* direction and negative values indicate stress in the negative *y* direction. Notice the large point stresses.

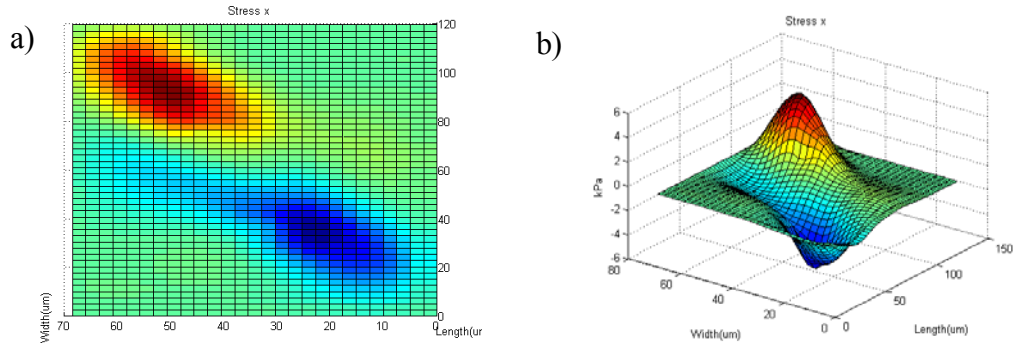

Figure 132. Stress maps of the stress in the *x* direction on layer-4
a) shows the 2D stress along layer-4 and b) shows the 3D stress along layer-4. The positive values indicate stress in the positive *x* direction and negative values indicate stress in the negative *x* direction.

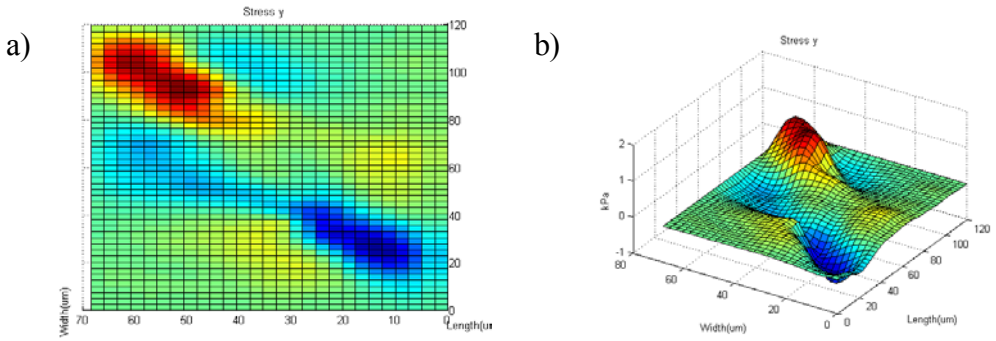

Figure 133. Stress maps of the stress in the *y* direction on layer-4
a) shows the 2D stress along layer-4 and b) shows the 3D stress along layer-4. The positive values indicate stress in the positive *y* direction and negative values indicate stress in the negative *y* direction.

6.III. Stained Images

The following 40x images show myocytes that have been either aligned on collagen or seeded randomly on 75 kPa gels. We did not use different stiffness gels for staining as the stiffness of the substrate (within the ranges used in this study) have not affected cell phenotype in the literature. Two stains were used in this study, FITC labeled anti-Connexin-43 and FITC labeled Phalloidin (F-Actin stain).

6.III.A. Connexin-43 Stained Images

The following images detail aligned myocytes stained with anti-Connexin-43:

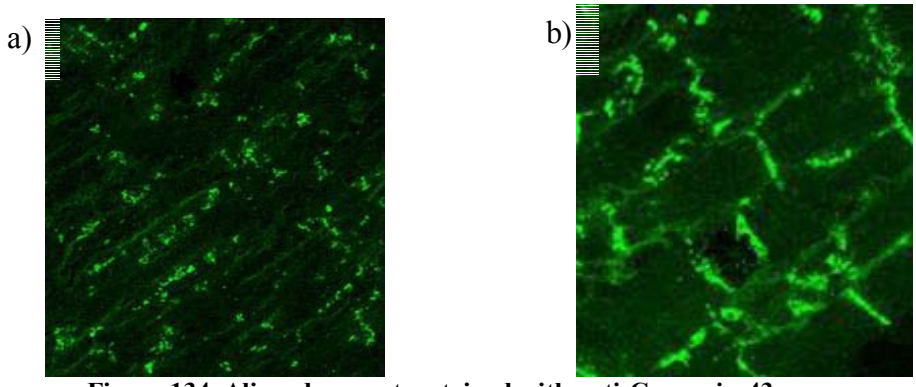

Figure 134. Aligned myocytes stained with anti-Connexin-43
Lighter spots designate the presence of Connexin-43 in cell membranes. b) highlights the location of normal aligned gap junctions at the ends of the rod-like phenotype

The following images detail random myocytes stained with anti-Connexin-43:

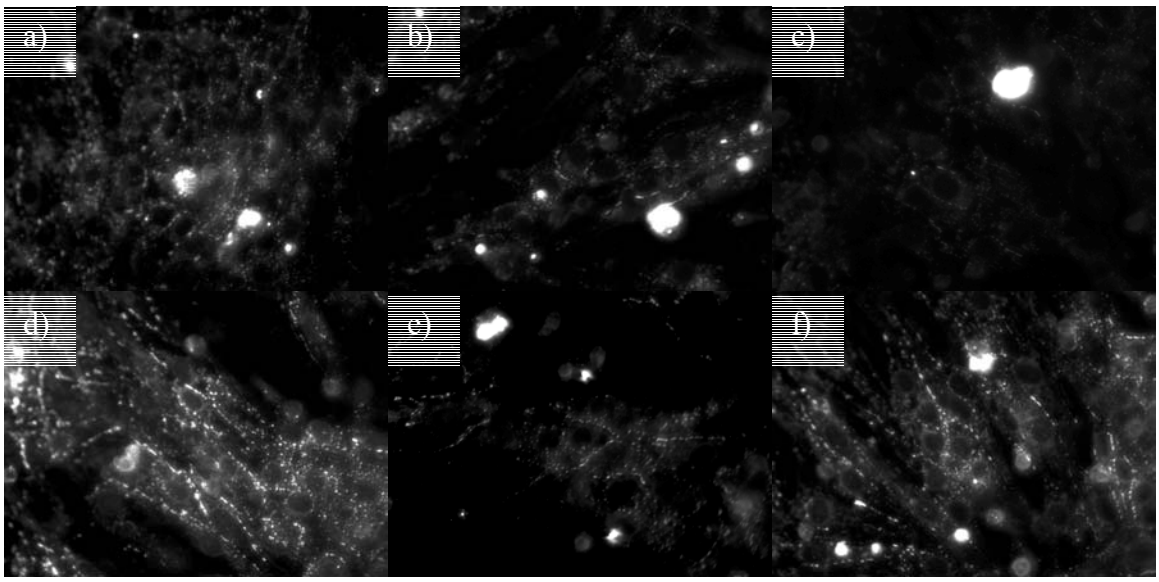

Figure 135. Random myocytes stained with anti-Connexin-43
Lighter spots designate the presence of Connexin-43 in cell membranes. Gap junctions were found to be present along the length of the cell periphery.

6.III.B.F-Actin Stained Images

The following images detail aligned myocytes stained with FITC Phalloidin:

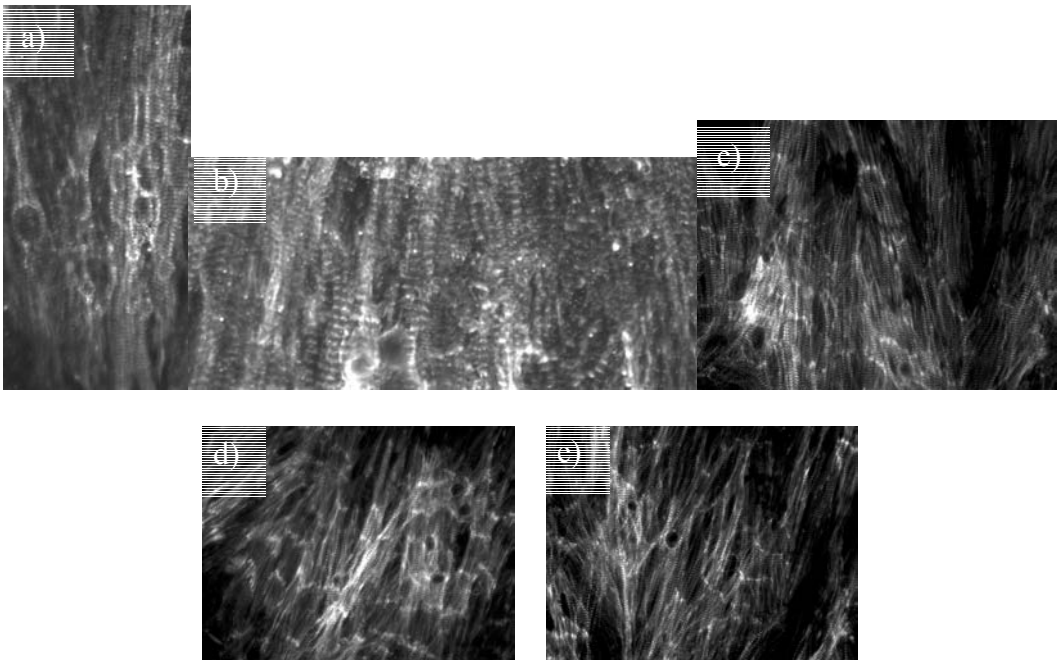

Figure 136. Aligned myocytes stained with FITC Phalloidin

F-Actin is a main component of cardiac sarcomeres and appear perpendicular to the long axis of aligned myocytes. This orientation is indicative of healthy myocytes.

The following images detail random myocytes stained with FITC Phalloidin:

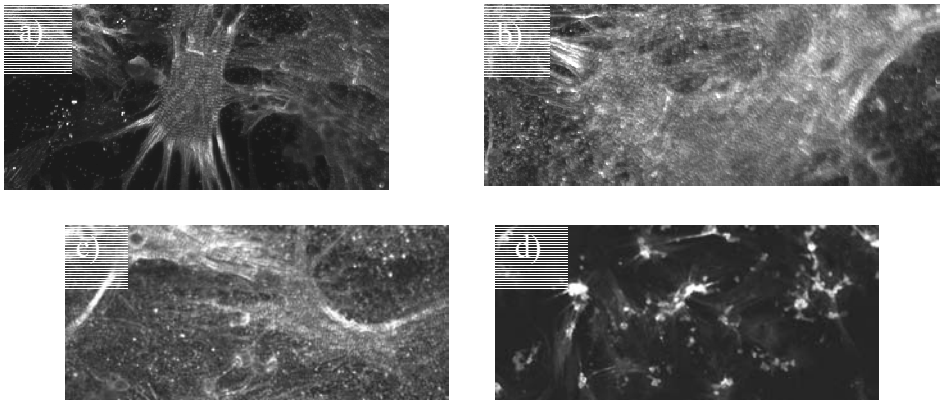

Figure 137. Random myocytes stained with FITC Phalloidin
F-Actin is a main component of cardiac sarcomeres and appear perpendicular to the long axis of aligned myocytes. As compared to the images in Figure 111, these sarcomere orientations are not aligned and are oriented in random directions indicative of a maladaptive phenotype

6.IV. Stress Trends

The following graph depicts the trends of the average maximum stresses measured for aligned and unaligned cells on 75 kPa, 30 kPa and 7 kPa gels.

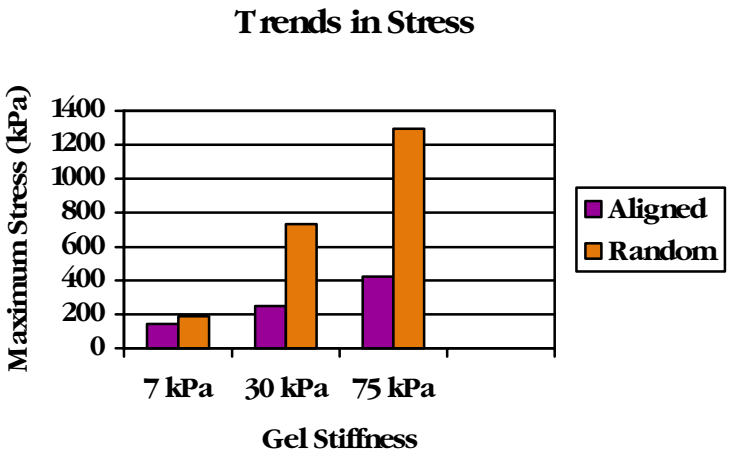

Graph 2. Trends in Stress. Gel Stiffness vs Maximum Contractile Stress
Maximum stress for 7 kPa: 141.63 kPa aligned & 186.68 kPa random. Maximum stress for 30 kPa: 249.19 kPa aligned & 734.81 random. Maximum stress for 75 kPa: 420.73 kPa aligned & 1293.55 kPa random

Chapter 7: Discussion

7.I. Gel Stiffness Confirmation

Gel stiffness was confirmed through AFM indentation testing reflected in Graph 1 of Section 6.I. For all three gel stiffnesses, the respective curves showed very little hysteresis, which is defined as a discrepancy between the indentation and releasing curves. As the tip is pressed further into the gel, the substrate will generate a reaction force and press back against the tip. The stiffer gels will prevent larger indentation depths while producing larger forces. If the substrate is of good physical properties, then the forces produced during indentation and releasing should be identical and overlap. If they are not, two distinct curves will be present. The current data suggests that these acrylamide gels have acceptable properties to allow even contraction and relaxations while under stress.

7.II. Dynamic Simulation Assumption

During the calculation of stress images using our dynamic simulation technique, we made the assumption to reduce our discretized element substrate into nodes with mass *m*. Doing so significantly reduced the complexity of the calculation as it allowed the analysis of six dimensions of displacement in stead of the continuous element displacement. By doing so, we also eliminated a significant amount of data that lent to the final magnitudes of contractile stresses. Thus, the current system is only capable of

producing relative stress profiles and not capable of predicting the strength of cell contraction. However, this assumption does not hinder the goal of this project. By comparing the relative trends of contraction stress, we still were able to determine the average differences in contractile stress between aligned and unaligned cells on surfaces with controlled physical properties, the details of which will be discussed in Section 7.VI.

7.III. Surface Layer Noise

The stress images generated through MATLAB on / near the surface layer consistently showed noise that was large enough to be comparable to some of the smaller contractile stresses. Clear evidence of such noise can be seen in Figure 22b, Figure 57b and Figure 58b. We know that this noise was only present on surface layers (layer-8) as the corresponding images taken for the same data set on a lower layer (layer-4) did not have these artifacts in all cases. To ensure that this noise was not being generated through our programs, we input the same data into similar programs written by colleagues that generate stress maps and the same noise was also observed, indicating that the artifacts were present in the data and not a result of our programs. This noise was small enough to not affect the overall trends of contractions and did not affect the results. Similarly, since we were looking for contraction stress trends (Section 7.II) the effect of the noise is further reduced because it constitutes only a small proportion of the stresses present. Thus, we can look at stress trends without the noise affecting our results.

It is our current belief that this noise was generated from cell-ECM junctions. As discussed in Section 2.I.A.3., myocytes use focal adhesions to physically attach themselves to the ECM. These attachments must, by their nature, exert some forces onto

the surface. If we consider the number of focal adhesions present between all of the myocytes and the substrate, then this background noise can be easily explained. Also, it follows to reason that these forces are still relatively small to those generated during contraction.

7.IV. Cell Orientation and Stress Concentrations

The normal myocyte phenotype is set up to generate stress along the longitudinal axis of the cell. The sarcomeres are all aligned so that when they contract all of the contractile stress is generated in the same direction. It is suggested that having these sarcomeres all aligned is more efficient for the cell as their total stress is a sum of their individual stresses. Thus, the average stress generated per sarcomeres can be kept to a minimum to produce the desired level of stress.

If a cell begins to undergo a phenotype change, like in a de-differentiated hypertrophy state, the sarcomeres begin to loose their aligned orientation. When this occurs, the combined strength of contraction is lost and sarcomeres begin to contract in various random orientations. Also, since hypertrophy is a response to pressure or volume overload, the individual myocyte typically begins to exert more force during contraction. Thus, with the loss of contractile orientation and the increased strength of contraction, myocytes that have lost their normal phenotype begin to contract with a stronger, less directed force.

Evidence of this occurrence can be seen in Figures 65, 66, 71 and 72. These figures show cells that have been randomly oriented and as a result, their stresses were

located around the periphery of the cell regions instead of being located at the ends as seen in Figures 17 & 18. Our system provided clear evidence that cells that have lost their normal phenotype produce stress distributions that have lost their concentrated end-to-end locations and have instead become randomly direction around the cell periphery.

7.V. Confirmation of De-Differentiated, Hypertrophic Phenotype

As previously discussed in Section 2.II.A.1 and Section 2.II.A.2, an increase in the amount and a change in the location of gap and adherens junctions has been shown to be coupled to a change in cell phenotype from normal to de-differentiated. This de-differentiated phenotype was shown to be an attempt by the cell to compensate for an increased load. A similar trend is also observed with the rearrangement of sarcomeres as discussed in the previous section.

In this study, we took confocal images of cells that had been stained for Connexin-42 and F-Actin to deduce the location and concentration of these two proteins in order to demonstrate that randomly oriented cells actually do exhibit this de-differentiated state. Evidence of this phenotype change can be seen in Section 6.III.A. Cells that were aligned on collagen exhibited the normal phenotype of having gap junctions at the ends of their longitudinal axis and having their sarcomeres oriented perpendicular to their longitudinal axis (Figures 109 & 111). Contrastingly, cells that have been randomly oriented showed a loss redistribution of Connexin-43 to the cell

periphery as well as a reorientation of sarcomeres units. This conclusively demonstrates that randomly oriented cells begin to exhibit a de-differentiated, hypertrophic phenotype.

7.VI. Contractile Stress Trends

The results of the trends in contractile stress are seen in Graph 2 in Section 6.IV. By looking at this graph, two trends become apparent: randomly oriented myocytes exert stronger contractile forces and stiffer gels produce stronger contractions.

As discussed in the previous two sections, the stress distribution as well as the cell phenotype changes in a random cell culture. The stresses become exerted in random orientations and sarcomeres become unaligned as a result of a de-differentiation to a juvenile phenotype. Cells that are oriented tend to concentrate their stresses at the end of the cell and are then able to reduce the strength of contraction of individual sarcomeres. When this orientation is lost, each sarcomere attempts to compensate by generating more force. Considering this and that some of these contraction orientations may overlap, the overall strength of contraction increases. This also makes sense as this de-differentiated phenotype is an attempt to generate more force.

Our data shows that cells on the 7 kPa gel had a 24.23% increase in contraction strength, a 66.09% contraction increase on the 30 kPa gel and a 67.47% contraction increase on the 75 kPa gel. Each of these relative increases confirms our prediction that randomly oriented myocytes will generate stronger contractile stresses than aligned myocytes.

The other trend seen in Graph 2 is that cells seeded on stiffer gels will produce stronger contraction stresses. To explain this, consider that the cell will contract with a

strength that is relative the reaction force produced through the acrylamide substrate. On weaker gels, there gel exhibits more elastic properties and begins to deform at lower applied stresses. Thus, the gel is not able to produce a strong enough reaction force to overcome the strength of the cell's force. The cell then is not able to exert any more force on its substrate. If the gel is stiffer, then it can generate stronger reaction forces before deforming, allowing the cell to produce stronger and stronger forces. Thus, we can explain the trends seen in the data: average maximum stress 420.73 kPa on 75 kPa gel, 249.19 kPa on 30 kPa gel and 141.63 kPa on 7 kPa gel. This trend is also observed regardless of cell orientation. The average maximum stress on random cell cultures: 1293.55 kPa on 75 kPa gel, 734.81 kPa on 30 kPa gel and 186.68 on 7 kPa gel. Despite the actual stress values being larger on random than aligned, they still increase as gel stiffness increases.

Chapter 8: Conclusions

The goal of this project was to create a system capable of characterizing the mechanical environment of specially designed myocyte cultures for the purpose of understanding the stress distribution of a normal and dysfunctional contractile myocyte. To do so, we fabricated substrates with defined physical properties, seeded aligned and random cardiac myocytes, imaged their contraction and processed those images to recreate representative stress maps. It is our belief that this system is fully capable of observing the trends of contraction between individual myocytes. There is room for improvement by increasing the complexity of our calculations; however, we have conclusively demonstrated an appropriate system for comparing the mechanical environments of myocytes with differing phenotypes. Likewise, we have provided evidence for our other objectives: that cells seeded onto stiffer gels will produce stronger contraction forces, and that aligned myocytes generate and are under less stress than unaligned myocytes. It is for these reasons that we consider our study a success in meeting our goal.

Currently, we are researching how to adjust our dynamic simulation technique to accommodate for elemental deformations such that our system will be able to predict exact magnitudes for contractile stresses as well as providing a more accurate stress distribution map.

In future applications of this system, we plan on using Laser Micropatterning to introduce fibroblasts into myocyte cell cultures. Laser Micropatterning is a technique that utilizes a weakly focused laser to trap a cell or particle within the beam. By adjusting the substrate beneath the cell within the laser, we can deposit specific cells at a desired

location on the substrate [106-108]. With this tool in conjunction with our current system, we would be capable of generating a multi cellular environment where we can analyze the mechanical stresses applied to the substrate. Because fibroblasts have been shown to affect the mechanical environment, these cells would be ideal candidates to test the mechanical reaction of myocytes to physiologic stimuli. By analyzing this more complex cell culture model, we can begin investigating some of the same cellular interactions observed in vivo and are one step closer to creating a cell culture model that can accurately describe the mechanical environment of adaptive and maladaptive hypertrophic cardiac cells.

Appendix A: Traction Force Microscopy Details

1. Preparation of Poly(Acrylamide) Gel Substrates

Coverslips prepared in similar fasion to Dembo *et al* [87] were first treated to allow for a covalent linkage between the glass surface and the polyacrylamide gel providing a flat, stable surface. The following steps illustrate the steps taken to prepare the glass coverslips for the polyacrylamide.

1) Coverslips (No. 1, 45 mm x 50 mm) were passed briefly through the inner flame of a Bunsen burner.
2) A drop of 0.1 N NaOH was smeared over the surface of each coverslip with a Pasteur pipette and allowed to dry in air.
3) The treated side of the coverslips was marked using a diamond-tipped pen and a small drop of 3-aminopropyltrimethoxysilane was smeared evenly on this surface.
4) After 4–5 min the coverslips were washed extensively with distilled H_2O.
5) The coverslips were then transferred, marked-side up, into petri dishes and covered with 0.5% glutaraldehyde in PBS (prepared by diluting 1 part of 70% stock solution with 140 parts of PBS).
6) After incubation at room temperature for 30 min the coverslips were washed extensively with multiple changes of distilled H_2O on a shaker and allowed to dry in air.

7) The treated coverslips were stored for up to 48 h after preparation [87]. At this step, the glass coverslips contain gluteraldehyde linkages and are able to covalently bind to most polymers containing amide groups.

The preparation of the acrylamide solutions was performed in the following fashion.

1) acrylamide (30% w/v) was mixed with *N*, *N*-methylene-bis-acrylamide (2.5% w/v) and distilled H_2O to obtain a final concentration of 10% acrylamide and 0.03% BIS. For more rigid or more flexible substrata the percentage of BIS was increased or decreased.

2) Fluorescent latex beads (0.2 mm FluoSpheres, carboxylate-modified) were sonicated briefly in a bath sonicator and added to the acrylamide mixture in volume ratio of 1:125. 3) The acrylamide/BIS solution was degassed and polymerization was initiated by addition of ammonium persulfate (10% w/v solution, 1:200 volume) and *N*,*N*,*N*,*N*-tetramethyl ethylenediamine (TEMED, 1:2000 volume).

4) Twenty-five ml of the acrylamide solution was immediately placed onto the surface of an activated coverslip and the droplet was flattened using a large circular coverslip (No. 1, 22 mm diam.).

5) The resulting sandwich assembly was turned upside down.

6) After polymerization (10–30 min), the circular cover glass was removed and the gel was washed on a shaker with HEPES (50 mM, pH 8.5) [87].

At this step the glass coverslip is bonded to a polyacrylamide gel with defined physical properties, however the gel is not yet capable of supporting cell adhesion. As stated earlier, cell adhesion is mediated through ECM proteins, specifically collagen I. As such,

the gels must then be treated such that a layer of the desired ECM protein is conjugated to the surface.

To accomplish this, a chemical named sulfo-SANPAH (sulfosuccinimidyl 6 (4-azido-2-nitrophenyl- amino) hexanoate) was used. Sulfo-SANPAH is a photoactivatable heterobifunctional reagent that acts as an intermediary between the acrylamide surface of the gel and the desired ECM protein. Specifically, sulfo-SANPAH contains a succinimidyl ester group that will react with the lysine ε-NH_2 sub regions of proteins and also a phenylazide group that, upon photoactivation, reacts nonspecifically with many chemically inert molecules including polyacrylamide and water. The protocol that was used is as follows:

1) fluid was drained off the surface of the polyacrylamide gels and 200 ml of Sulfo-SANPAH (1 mM in 50 mM HEPES, pH 8.5,) was applied.
2) The surface of each gel was then exposed to UV light from a 30 W germicidal lamp at a distance of 6 inches for 5 min. The darkened Sulfo-SANPAH solution was removed and the photoactivation procedure was repeated a second time.
3) The glass-supported polyacrylamide sheets were twice subjected to 15 min shaker washes with 50 mM HEPES (pH 8.5).
4) The polyacrylamide sheets were then covered with a solution of soluble type I collagen (0.2 mg/ml) and allowed to react overnight at 4°C on a shaker.
5) The gels were then washed extensively with PBS, mounted onto culture chambers, and sterilized with UV irradiation [87].

The gel thickness was determined by using a microscope to focus on the plane of the surface of the glass and then focusing on the surface of the gel and using microscope

software to interpret the gel thickness, on average the gels were ~70μm. The physical properties of these gels were tested by using compression testing. A coverslip was placed on the surface of a polyacrylamide gel and weights were then placed on the slip, compressing the gel. The degree of compression was determined using the microscope method. The Young's Modulus was then approximated using the following equation:

$$E = (F / A)(\Delta L / L) \qquad \text{Eq.10}$$

where A is the surface area of the gel, F is the weight applied, ΔL is the compression distance and L is the unstressed distance. In this study, the average Young's Modulus was found to be ~ 62 ± 1 kdyn/cm^2 (~6200 pN/μm^2). During these tests, there was no detection of any changes in the total volume of the gels and as such Poisson's ratio for these substrata was assumed to be approximately 0.5.

At this point, the gels were capable of supporting viable cells. The cells used by Dembo *et al*[87] were Swiss 3T3 fibroblasts and were cultured in DMEM supplemented with 10% donor calf serum, 2 mM L-glutamine, 50 μg/ml streptomycin, 50 U/ml penicillin, and 250 μg/ml amphotercin B. These 3T3 cells were allowed to adhere, spread and begin migration. During migration, the cells would transmit their tractional forces to the substrata and in doing so would displace the fluorescent beads within the substrate. Images were taken at 40x magnification with a 0.65 NA Achromat Zeiss objective. In order to generate one stress map, two images must be taken so that the positions of the beads embedded in the gels can be compared. This was accomplished using images taken just prior to cells being trypsinized and images taken just after the trypsinization. Doing so will produce images where the substrate is stressed (prior to trypsinization) and images where the substrate is relaxed (after trypsinization). After these images are captured, they

are processed to create distribution maps that are representative of the displacements of the fluorescent particles within the substrates.

2. Correlation-Based Optical Flow

Optical flow is used for interpretations between sets of images and exists in a variety of forms. Differential optical flow compares the derivatives of image profiles by using high-pass, low-pass, velocity-tuned and band-pass filters. Region based optical flow use the actual image or motion profiles and define the velocities as a displacement vector. The benefit of region based optical flow over differential is that the later is subject to noise because a small number of frames exist or because of aliasing in the image acquisition process. These displacement vectors are generated using normalized cross-correlation or minimizing a distance measure. A typically used function for this procedure is the Sum-of-Squared Difference (SSD) equation:

$$SSD_{1,2}(\mathbf{x};\mathbf{d}) = \sum_{j=-n}^{n}\sum_{i=-n}^{n} W(i,j)[I_1(x+(i,j)) - I_2(x+(i,j))]^2 \qquad \text{Eq11.}$$

where W denotes a discrete 2-D window function, and $\mathbf{d} = (d_x\ d_y)$ take on integer values. Using this equation, minimizing the SSD distance measure will ensure that the pixels at (i,j) in I_1 and I_2 are most likely the same positions and as such the displacement is calculated with high accuracy [109, 110].

Correlation-based optical flow uses a similar normalizing function to compare regions of intensity. For two images with intensity profiles defined as follows:

$$I_k = \begin{bmatrix} P_k(1,1) & P_k(2,1) & P_k(n_x-1,1) & P_k(n_x,1) \\ P_k(1,2) & P_k(2,2) & P_k(n_x-1,2) & P_k(n_x,2) \\ P_k(1,n_y-1) & P_k(2,n_y-1) & P_k(n_x-1,n_y-1) & P_k(n_x,n_y-1) \\ P_k(1,n_y) & P_k(2,n_y) & P_k(n_x-1,n_y) & P_k(n_x,n_y) \end{bmatrix} \qquad \text{Eq12.}$$

where $k = 0$ or 1 and $P_k(x, y)$ is the intensity at pixel (x, y), we want to test if a pixel at (x, y) on I_0 has moved to (u, v) on I_1. To do so, we define two correlation windows with a distance of C pixels from (x, y) and (u, v). These windows are labeled B_0 and B_1 and are said to have "similar intensity" patterns if the pixel at $(x + \delta_x, y + \delta_y)$ on B_0 has an intensity value that has a high correlation to the corresponding pixel $(u + \delta_x, v + \delta_y)$ on B_1. As previously mentioned, this technique utilizes the following equation which is similar to Eq11:

$$R(x,y,u,v,C) = \frac{\sum_{\delta_x}\sum_{\delta_y} P_0(x+\delta_x, y+\delta_y) P_1(u+\delta_x, v+\delta_y)}{(\sum_{\delta_x}\sum_{\delta_y} P_0^2(x+\delta_x, y+\delta_y))^{1/2} (\sum\sum P_1^2(u+\delta_x, v+\delta_y))^{1/2}} \qquad \text{Eq13.}$$

where R is the correlation coefficient, which determines how close B_0 is to B_1. Since R is a normalization constant, the closer it comes to 1 the more "correlated" B_0 is to B_1 and if R is 0 then B_0 and B_1 are said to be "uncorrelated". Eq3 indicates that all values of δ_x and δ_y within B_0 and B_1, i.e. with $+C$ to $-C$. Figure 1 gives a visual example of the correlation process. Of particular importance when assigning values to the parameters of Eq3 is the value of C. Choosing a value that is too small will reduce the number of markers in which to compare correlation windows leading to an unambiguous pattern and causing the calculation to fail. Choosing a value that is too large will result in a loss of resolution since smaller movements would be lost within the correlation windows. The maximum testing distance in which to select pixels is defined as a term S from (x, y) [90].

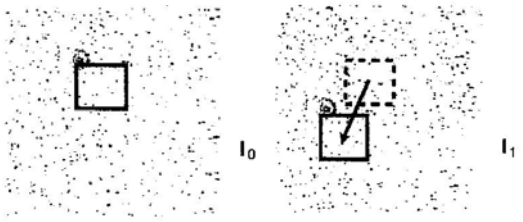

Figure 138. Correlation-Based Optical Flow.
A correlation window is selected in I_0 of size C at (x, y) and mapped onto I_1 beginning at (u, v) and testing at points $(u + \delta_x, v + \delta_y)$. The summation of these assessments results in the correlation value R. R ranges from +1 to -1 and the closer R is to 1, the more correlated the two windows are [90].

Procedurally, each pixel $(u + \delta_x, v + \delta_y)$ to be tested with (x, y) will be mapped onto a set of R values for each $(u + \delta_x, v + \delta_y)$ within the desired area. A graphical representation of R can be seen in Figure 2:

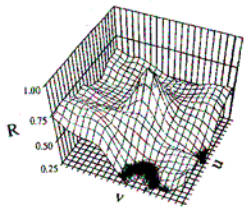

Figure 139. 3-D graph of the correlation coefficient *R*.
The value of $R(x, y, u, v, C)$ is plotted for various values of u and v. As seen a clear maximum for R exists at ~0.93 for the images selected [90].

Once a maximum value of R is determined, additional iterations are performed to fine tune the final displacement from (x, y) to (u, v). This is accomplished by taking the values of (u, v) from the previous iteration and imputing those as the new (x, y) in the next iteration and shortening S and reducing C. Doing so will begin the correlation process at the pixel with the highest previous R and increase the resolution by decreasing S and C. This iteration process continues until the new value of R does not change with the previous iteration's R value. At this point, the pixel that corresponds to the highest R value is taken to be the final position (u^*, v^*) and the displacement between it and (x, y) is calculated and stored. Additional resolution is also obtained through sub-pixel resolution by using the following equations:

$$u_{jk}^{**} = u_{jk}^{*} \frac{0.5[R(x_j, y_k, u_{jk}^{*}+1, v_{jk}^{*}, C) - R(x_j, y_k, u_{jk}^{*}-1, v_{jk}^{*}, C)]}{2R(x_j, y_k, u_{jk}^{*}, v_{jk}^{*}, C) - R(x_j, y_k, u_{jk}^{*}-1, v_{jk}^{*}, C) - R(x_j, y_k, u_{jk}^{*}+1, v_{jk}^{*}, C)}$$

Eq14a.

$$v_{jk}^{**} = v_{jk}^{*} \frac{0.5[R(x_j, y_k, u_{jk}^{*}, v_{jk}^{*}+1, C) - R(x_j, y_k, u_{jk}^{*}, v_{jk}^{*}-1, C)]}{2R(x_j, y_k, u_{jk}^{*}, v_{jk}^{*}, C) - R(x_j, y_k, u_{jk}^{*}, v_{jk}^{*}-1, C) - R(x_j, y_k, u_{jk}^{*}, v_{jk}^{*}+1, C)}$$

Eq14b.

with u_{jk}^{**} and v_{jk}^{**} as the new final pixel positions. Equation 14 averages the adjacent pixels in order to generate a new set of end position coordinates with sub-pixel resolution. This sub-pixel resolution reflects the smooth and continuous nature of the correlation coefficient as well as its own necessity as the particles used to approximate the substrate deformations have approximate diameters of 0.3-0.6μm whereas pixels are generally 0.1-0.3μm. Thus, in order to generate accurate displacements, sub-pixel resolution is a needed [90].

After the set of $(u_{jk}^{**}, v_{jk}^{**})$ has been found for all initial (*x, y*) test pixels, there is still the need to check for correspondence errors in the data. That is, because of S/N ratios, low density of marker beads or a small correlation window, discontinuous and random displacements can occur. In order to detect and correct these errors, the in-plane strain components are estimated with the following equations:

$$\varepsilon_{xx}^{2} = 0.5\left|\frac{u_{(j+1)k}^{**} - u_{jk}^{**}}{x_{j+1} - x_j} - 1\right|^2 + 0.5\left|\frac{u_{jk}^{**} - u_{(j-1)k}^{**}}{x_j - x_{j-1}} - 1\right|^2$$

Eq15a.

$$\varepsilon_{yx}^{2} = 0.5\left|\frac{v_{(j+1)k}^{**} - v_{jk}^{**}}{x_{j+1} - x_j}\right|^2 + 0.5\left|\frac{v_{jk}^{**} - v_{(j-1)k}^{**}}{x_j - x_{j-1}}\right|^2$$

Eq15b

$$\varepsilon_{xy}^2 = 0.5\left|\frac{u_{j(k+1)}^{**} - u_{jk}^{**}}{y_{k+1} - y_k}\right|^2 + 0.5\left|\frac{u_{jk}^{**} - u_{j(k-1)}^{**}}{y_k - y_{k-1}}\right|^2 \quad \text{Eq15c}$$

$$\varepsilon_{yy}^2 = 0.5\left|\frac{v_{j(k+1)}^{**} - v_{jk}^{**}}{y_{k+1} - y_k} - 1\right|^2 + 0.5\left|\frac{v_{jk}^{**} - v_{j(k-1)}^{**}}{y_k - y_{k-1}} - 1\right|^2 \quad \text{Eq15d}$$

$$\left\|\varepsilon_{jk}\right\| = \sqrt{\varepsilon_{xx}^2 + \varepsilon_{xy}^2 + \varepsilon_{yx}^2 + \varepsilon_{yy}^2} \quad \text{Eq16}$$

The value of $\left\|\varepsilon_{jk}\right\|$ is then compared with a limiting value of strain ε_{max} which will change depending on the physical properties of the substrate used. If $\left\|\varepsilon_{jk}\right\|$ is larger than ε_{max} or drastically different then those points $(u_{jk}^{**}, v_{jk}^{**})$ should be considered suspect and recalculated with any changes in *C* that may prevent the points from becoming subject to reinvestigation again [90].

Additional errors may occur during this process through microscope drift or any other background vibration that may cause the entire sample to shift during observation, which is called a registration artifact. To remove this artifact, it must first be realized that because the desired displacements occur within a relatively small area of the entire field of observation, the artifacts will occur at all points and with maximum frequency. Thus in order to remove it from the final displacement set a frequency histogram of all displacements (as seen in Figure 3) is set up.

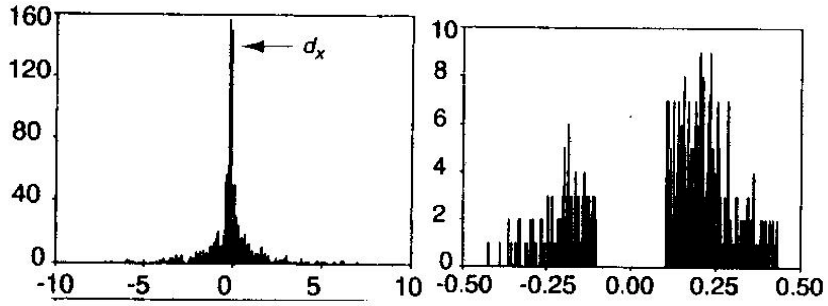

Figure 140. Frequency Histogram of displacements.
A distribution of all the displacements on the x-axis and the number of pixels with that displacement on the y-axis (left). The trimmed histogram with the most frequent distributions removed leaving behind the meaningful data (right) [90].

These histograms consist of the uncorrected displacements in the x and y directions. The displacement values are placed into bins and the most frequent value is measured and stored. This value is then set to 0 and the displacements are placed into more exacting bins creating a new most frequent value. This process is repeated until the most frequent value does not change after being zeroed. At this point all of the shifts made to zero the most frequent values are added together and the artifact is quantified. This value is then subtracted from each displacement leaving behind the meaningful values (Figure 4) [90].

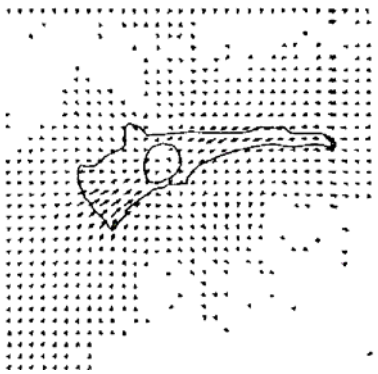

Figure 141. Displacement map of a locomoting 3T3 fibroblast.
The displacement map generated through correlation-based optical flow of a fibroblast applying traction during locomotion on a deformable substrate [90].

By processing sequences of images using correlation-based optical flow, multiple displacement maps can be generated in a relatively short period of time. Thus, by taking images of fluorescent particles embedded in polyacrylamide gels during cell traction, displacement maps can be generated and refined and then are ready to be used by the next stage of Traction Force Microscopy.

3. Continuum Mechanics

In order to generate test displacement data, the calculations begin with a standard force balance:

$$h(\partial_1 \sigma_{\alpha 1} + \partial_2 \sigma_{\alpha 2}) + T_\alpha = 0 \qquad \text{Eq17}$$

with $\sigma_{\alpha\beta}$ as the stress tensor, T_α as the applied traction stress and h as the gel thickness. In addition to Equation 17, the plane deformation must also be considered as a point $\mathbf{x} = (x_1, x_2)$ will be displaced to a new equilibrium position $\mathbf{x}' = \mathbf{x} + \mathbf{d}$. In order to take this deformation into account, the strain tensor is defined as such:

$$\varepsilon_{\alpha\beta} = 0.5(\partial_\alpha d_\beta + \partial_\beta d_\alpha) \qquad \text{Eq18}$$

Finally, by combining Hooke's Law with the strain tensor requirements the following equation can be generated:

$$\sigma_{\alpha\beta} = \frac{E}{(1+\nu)}\varepsilon_{\alpha\beta} + \frac{E\nu(\varepsilon_{11}+\varepsilon_{22})}{(1-\nu^2)}\delta_{\alpha\beta} + \bar{\sigma}\delta_{\alpha\beta} \qquad \text{Eq19}$$

with E as the Young modulus, ν as the Poisson ratio and $\bar{\sigma}$ as the prestressed drumhead tension. For the substrates used in this experiment, polyacrylamide was found to be incompressible and thus Poisson's ratio is very close to 0.5 [71, 105, 111]. The significance of $\bar{\sigma}$ is one of the main differences between the current method of measuring

beads and the older methods of measuring wrinkles [83]. With a high $\bar{\sigma}$, the surface remains flat and resists creating wrinkles when under stress ensuring that the deformations are planar. If this value were to be lower, then it would become impossible to generate any quantitative data as the measurements from the bead images would include a vertical displacement that would not be compensated for resulting in the system failing.

Through substitution of Equation 19 into Equation 17, a second order partial differential equation for deformation equilibrium in the midplane is generated:

$$\frac{E_s}{1-\nu^2}\partial_1\partial_1 d_1 + \frac{E_s}{2(1+\nu)}\partial_2\partial_2 d_1 + \frac{E_s}{2(1-\nu)}\partial_1\partial_2 d_2 = -T_1 \qquad \text{Eq20a}$$

$$\frac{E_s}{1-\nu^2}\partial_2\partial_2 d_2 + \frac{E_s}{2(1+\nu)}\partial_1\partial_1 d_2 + \frac{E_s}{2(1-\nu)}\partial_2\partial_1 d_1 = -T_2 \qquad \text{Eq20b}$$

with $E_s = Eh$ as the Young's modulus on the surface of the substrate, which compensates for the membrane thickness as mentioned previously. From here in order to rearrange Equations 20a and 20b to solve for d, some assumptions need to be made. Specifically, the membrane is assumed to be infinite and that $\sigma_{\alpha\beta} \to \bar{\sigma}\delta_{\alpha\beta}$ as $|\mathbf{x}| \to \infty$. In other words, the tractional stress component drops to zero and the total stress becomes the drumhead tension with more distance between the point of interest and the cell. With this consideration, an integral equation can be generated that solves for d given the continuous stress function:

$$d_\alpha(\mathbf{x}) = \frac{1}{E_s}\iint [g_{\alpha 1}(\mathbf{x},\mathbf{f})T_1(\mathbf{f}) + g_{\alpha 2}(\mathbf{x},\mathbf{f})T_2(\mathbf{f})]d\mathbf{f} \qquad \text{Eq21}$$

where

$$g_{\alpha\beta} \equiv \frac{(1+\nu)^2}{4\pi}\left[\frac{(x_\alpha - f_\alpha)(x_\beta - f_\beta)}{|\mathbf{x}-\mathbf{f}|^2} + \delta_{\alpha\beta}\frac{(3-\nu)}{(1+\nu)}\ln\left(\frac{1}{|\mathbf{x}-\mathbf{f}|}\right)\right]. \qquad \text{Eq22}$$

The following Equation 12 is the so-called Green's function and can be thought of as the displacement in the α direction at the point (x_1, x_2) resulting from an impulse delta function stress in the β direction at the point (f_1, f_2). In order to ensure that all stress fields input to Equation 21 generate displacement data, one last generalization needs to be made. There needs to be a bounded support for Equation 21 and satisfy a global force balance:

$$\iint T_1(\mathbf{f})d\mathbf{f} = \iint T_2(\mathbf{f})d\mathbf{f} = 0. \qquad \text{Eq23}$$

In other words, the contribution of the stresses generated from cell traction does not change the overall traction of the surface along the entire lengths of the gel, which when considering the size and area of cell traction forces is found to be true [71, 112].

In the next step, it is important to remember that cells use focal adhesions to not only mechanically attach to the polyacrylamide substrate but also apply traction stresses to their environment. Thus, cells will not directly apply stresses outside of the area (Ω) they occupy on the substrate. This consideration will be taken into account when generating test stress fields.

Finally, the equation to generate the test stress distributions is as follows:

$$\mathbf{T}(\mathbf{f}) = \sum_{k=1}^{N}\mathbf{w}^k\left(S^k(\mathbf{f}) - \frac{A^k}{A_T}\right), \mathbf{f} \in \Omega \qquad \text{Eq24}$$

where

$$A_T \equiv \iint_{\Omega} d\mathbf{f} \qquad \text{Eq25}$$

is the total mesh area within Ω;

$$A^k \equiv \iint_{\Omega} S^k(\mathbf{f}) d\mathbf{f} \qquad \text{Eq26}$$

is the area of the *k*th node in the mesh under Ω;

$$S^k(\mathbf{f}^j) = \delta_{kj} \quad \forall_j = 1,2,....N \qquad \text{Eq27}$$

is the shape function for the defined quadrilateral mesh under Ω. *N* is the number of nodes within the mesh, $\mathbf{f}^j$ is the position of the *j*th node, δ_{kj} is the Kronecker delta function and $\mathbf{w}^k$ are the mesh associated degrees of freedom at the *k*th node. Equation 24 generates a continuous stress field through quadrilateral shape functions for all points $\mathbf{f}^j$ in Ω. With these definitions, it is convenient to define the latent background drift as the degrees of freedom at the zeroth node $\mathbf{w}^0$. In coordination with this, the zeroth shape function and area of the null set are $S^0(\mathbf{f}) = 0$ and $A^0 = 0$ respectively [71].

By generating test stress fields using Equation 24, checking those stress fields in Equation 16 and by inputting those fields into Equation 21 continuous test displacement fields are generated that are within the physical boundaries and restrictions of the system. At this point, finite displacement fields have been calculated from fluorescent images of the substrate as well as continuous displacement fields that have been calculated from test continuous stress fields, which have themselves been created based on the physical restrictions of the system. The last remaining step required is to use statistical analysis,

specifically Bayesian hypothesis testing, to match the best continuous stress field to the calculated finite displacement field.

4. Bayesian Hypothesis Testing

Let $\{X\}$ be the set of all possible outcomes of one experiment and let X be the particular result obtained during the actual experiment. Then, let H be a test hypothesis as to the information necessary to completely predict the outcome of the experiment. The probability that H actually does completely predict the correct information is represented as $P(H)$ and the same probability given the outcome X is correct is represented as $P(H|X)$. Thus, of all the possible H in the set $\{H\}$, the hypothesis that maximizes $P(H \mid X)$ will be the best explanation of the experiment. In terms pertinent to the current study, $\{X\}$ is the set of finite displacement maps generated through correlation-based optical flow and X is the particular map for the desired frames that are being analyzed. $\{H\}$ is the set of continuous displacement maps generated through finite element analysis and H is the particular test map that is being compared to X for the highest likelihood that they are identical, maximizing $P(H \mid X)$ [71, 87].

In order to compute $P(H \mid X)$ for the values of H and X the rule of inductive logic is used that describes the postexperimental probability of the hypothesis H is given as:

$$P(H \mid X) = P(X \mid H)P(H)S_x^{-1}. \qquad \text{Eq28}$$

In Equation 28, the term on the left $P(X \mid H)$ is the probability of producing the result X given that the hypothesis H is true, i.e. the probability of producing the finite displacement map given that the continuous displacement map is true. The last term S_x^{-1} is a normalization constant to ensure that the probability distribution of $P(H \mid X)$ for

all $H \in \{H\}$ will be exactly 1. In order to quantitatively determine *P(X | H)*, first each term on the right side of Equation 28 needs to be represented mathematically [71].

The first term *P(X | H)* is identical to probability of obtaining discrete values of the errors by random sampling from an appropriate distribution. In the case of the current experiments, the errors in the particle displacement measurements are assumed to be Gaussian with means equal to 0 and standard deviations equal to the pixel radius. Thus, the probability of the observed experiment is:

$$P(X \mid H) \propto \exp(-\mathrm{X}^2) \qquad \text{Eq29}$$

where

$$\mathrm{X}^2 \equiv \sum_{p=1}^{P} \left| \frac{\mathbf{r}^p}{s} \right|^2 = \frac{1}{s^2} \sum_{p=1}^{P} \left| \hat{\mathbf{d}}^p - \mathbf{w}^0 - \mathbf{d}^p \right|^2 \qquad \text{Eq30}$$

which is the chi-square statistic with $\mathbf{w}^0$ as the drift error determined from Equation 24, $\hat{\mathbf{d}}^p$ is the experimental position of the *p*th particle (position in *X*) and $\mathbf{d}^p$ is the theoretical position of the *p*th particle (position in *H*) [71].

The second term *P(H)* is more complicated to determine as it is subject to personal and subjective biases. As such, we must assume that this probability follows Occam's rule that the actual result will occur with as few assumptions as possible. Thus, it would follow that the probability would also be approximate to the inverse of the complexity of the system:

$$P(H) \propto \exp(-\zeta^2) \qquad \text{Eq31}$$

where

$$\zeta^2 = \int_{\Omega} \left(\frac{T_1(f_1, f_2}{\lambda} \right)^2 + \left(\frac{T_2(f_1, f_2}{\lambda} \right)^2 \frac{df_1 df_2}{A_{TOT}} \qquad \text{Eq32}$$

with λ as a complexity scale factor with the same dimensions as the traction density and defined as:

$$\left[\frac{E_S s}{\lambda}\right]^2 = \sum_{m=1}^{N}\sum_{p=1}^{P}\frac{N}{2P}\sum_{\alpha=1}^{2}\sum_{\beta=1}^{2}\left[\iint g_{\alpha\beta}(\mathbf{x}^p,\mathbf{f})\left(S^m(\mathbf{f})-\frac{A^m}{A_T}\right)d\mathbf{f}\right]^2. \qquad \text{Eq33}$$

By using Equations 32 and 33, the complexity C^2 can be calculated and the probability *P(H)* can be estimated. Of particular note is that the complexity depends on mesh geometry and not on bead displacements ensuring *P(H)* does not depend on any value from the set $\{X\}$ [71].

Using Equations 29 and 31, a quantitative value for the probability that the continuous displacement map is identical to the finite displacement map is obtained. By systematically comparing all values in $\{H\}$ against the desired value from $\{X\}$, the most probable stress map can be decisively said to be the most accurate representation of the traction exerted by the locomoting fibroblast across the deformable substrate [71].

5. Further Details

Finding the continuous stress map with the highest likelihood of being identical to the measured displacement map is based on a Bayesian Hypothesis Test represented by maximizing Equation 28. Continuous stress maps are generated by using the physical restrictions of the system using Equation 24 and then used to generate continuous displacement maps using Equation 21. Examples of these maps can be seen in the following Figures:

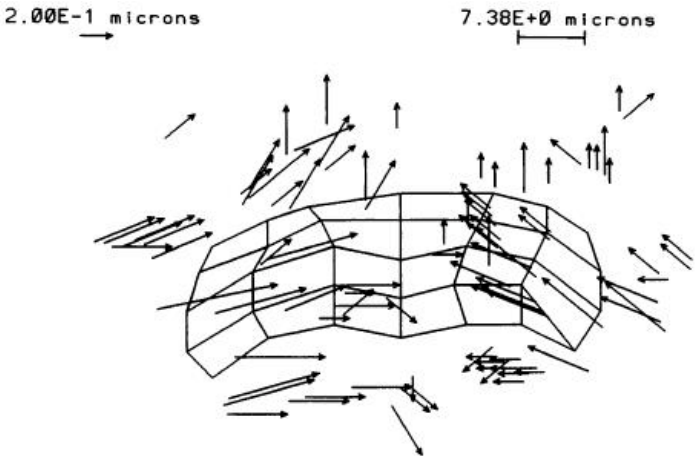

Figure 142. Finite Displacement Map.
Image of a displacement map generated through Correlation-Based Optical Flow [71].

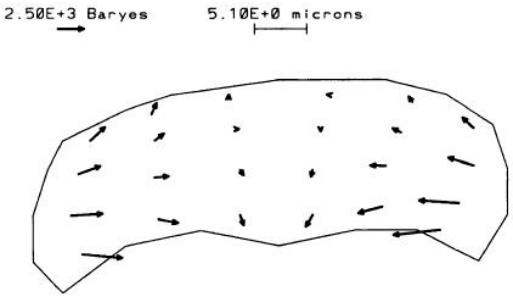

Figure 143. Continuous Stress Map.
Image of a stress map generated through Equation 14 to be tested [71].

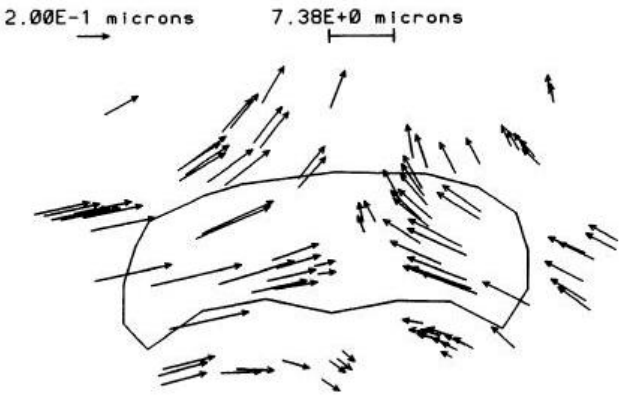

Figure 144. Continuous Displacement Map.
Image of displacement map generated from Image 2 through Equation 11 and then compared to Image 1 with Equation 18 and found to be the most likely to be the continuous field for the traction [71].

By visually comparing Figures 1 and 3, the similarity can be seen and through Equation 18, Figure 3 is found to be the most likely continuous map of the displacements and thus Figure 2 is the most likely continuous map of the tractions. Despite the

appearance that Figure 2 is finite, however the vectors shown in the Figure are representatives of finite elements of the continuous map. The rms error determined through Bayesian hypothesis testing was found to be ±0.094μm, authenticating Figure 2 being the actual traction map [71].

Also of interest is the effect of noise on the generation of displacement maps when using Equation 14. Figures 4-7 illustrate that effect. Figure 4 shows a hypothetical test stress map for a given cell boundary Ω. Figure 5 shows a typical displacement map calculated with Equation 14. Figure 6 shows a stress map calculated in the same manner as the image in Figure 5, however a drift error and a random error has been added to each displacement vector giving a signal to noise ratio of 5:1. It is apparent when comparing Figures 5 and 6 that error drastically effects the test displacements and reinforces the need for the precautions set up in the previous equations. Figure 7 furthers the example by increasing the signal to noise ratio to 1:1 [71].

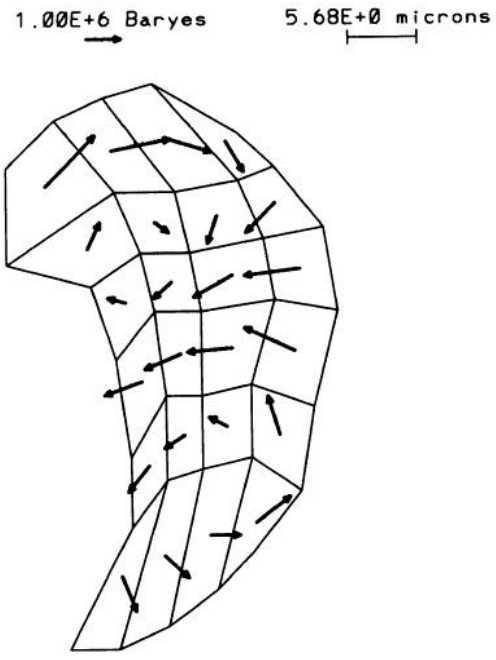

Figure 145. Test Stress Map
. Hypothetical stress map generated using Equation 14 [71].

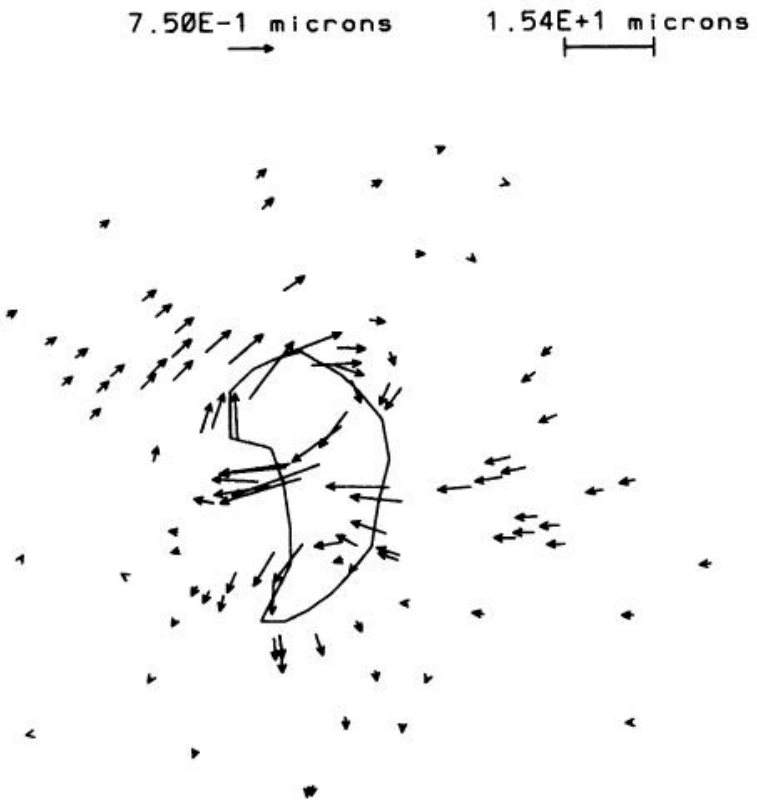

Figure 146. Test displacement map.
Displacement map generated from Figure 4 using Equation 11 [71].

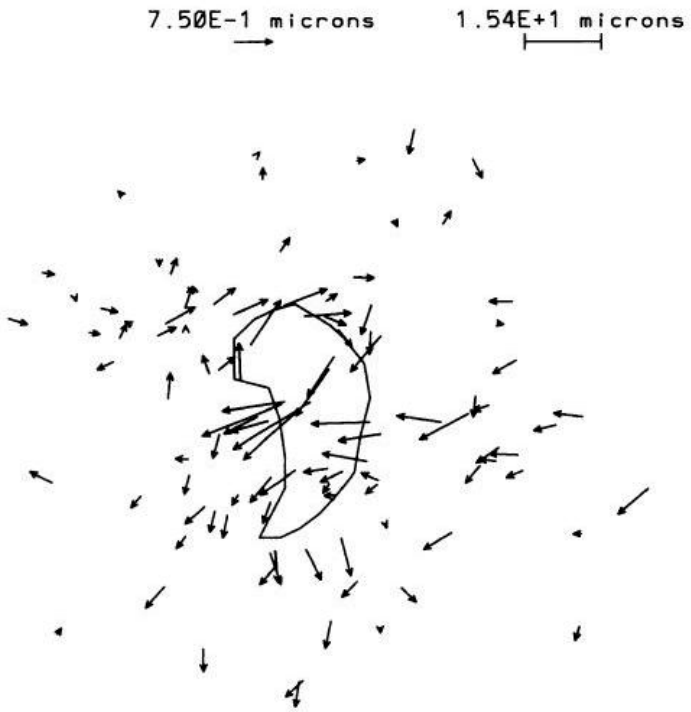

Figure 147. Test displacement map with error.

Displacement map generated with error added to result with a signal to noise ratio of 5:1. Comparing to Figure 4, the vectors are more scattered [71].

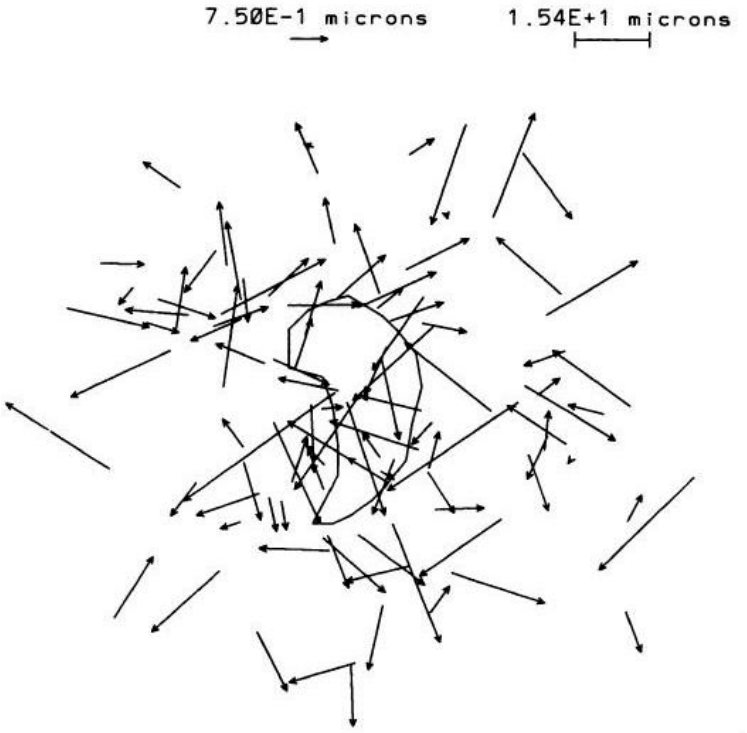

Figure 148. Test displacement map with large error.
Displacement map generated with a larger error than Figure 6 with a signal to noise ratio of 1:1 [71].

Appendix B: Cell Culture Protocols

3 Day Neonatal Rat Heart Dissection

Protocol for Percoll Gel Columns

1. Prepare Percoll Stock Solution (9:1 of Percoll : 1.5M NaCl)
2. Add 3.7g/100mL of Hepes to 10x MEM and dilute to 1x with distilled water
3. Prepare Percoll solutions

   Percoll A: (60% Percoll Stock Solution : 40% MEM) = 1.08 g/mL (for 3mL use 1.8mL of Percoll Stock and 1.2mL of MEM)

   Percoll B: (40% Percoll Stock Solution : 60% MEMα) = 1.06 g/mL (for 3mL use 1.2mL of Percoll Stock and 1.8mL of MEMα)

   Percoll C: (75% Percoll Stock Solution : 25% MEMα) =1.10 g/mL (for 3mL use 2.25mL of Percoll Stock and 0.75mL of MEMα)

4. Column preparation. In a 15mL conical tube add 3mL of **Percoll C**. Then **CAREFULLY** add 3mL of **Percoll A** on top of the bottom layer. **DO NOT MIX LAYERS**. Then **CAREFULLY** add 3mL of **Percoll B** on top of the middle layer. **DO NOT MIX LAYERS**.
5. Leave columns until cell suspension is ready

Procedure

1. Add 1mL of Pen/Strep per 100mL of KRB. pH to 7.4 and filter. Then add 0.4% Horse Serum (1mL per 250mL of KRB)
2. Put 50mL of KRB into a conical tube and add 6000 units of type 1 collagenase (for total of 120 units/mL)
3. Place KRB w/ HS, Myocyte media, Fibroblast media and collagenase in waterbath at 37degrees
4. Fill 2 50mL tubes with Moscona's Saline and place in ice bucket with 2 empty 15mL tubes.
5. **AT ANIMAL CARE FACILITY**. Fill the 2 empty 15mL tubes with Moscona's Saline and put on ice. Use remaining Saline to fill the bottom of 2 100mm culture dishes.
6. **UNDER THE HOOD,** decapitate the pups and cut down the sternum to open the chest cavity. Then pinch the shoulder blades together to have the heart pop out of the chest cavity. Remove the heart with sterile forceps and place into a 100mm dish with Saline (15 maximum).
7. Gently rinse the hearts in Saline while trying to remove any blood present than may have congealed. Place the hearts into the 15mL tubes on ice.
8. Clean up by placing the bodies and heads in ziploc bags unless other people requested the parts. Place the cover mats and the used dishes and tubes into the ziploc bags as well. Leave bags in hood. Clean the surface of the hood with EtOH and clean the instruments in the sink with soap and place on rack to dry.
9. **AT LAB,** clean off as much blood as possible using cold Moscona's Saline. Remove as much Saline as possible and place hearts into a 30mm dish and mince using sterile scissors.

10. Once the hearts are minced, place the tissue into a 50mL tube and label it **H** and add 8mL of collagenase. Place tube **H** in the water bath @ **5min, 37 degrees, at 85 rpm**.
11. Allow suspension to settle and pour off the supernatant into the waste. Add 8mL of collagenase and place tube **H** in the water bath @ **10min, 37 degrees, at 85 rpm**.
12. Take tube **H** out of the water bath and add 1mL of DNAse. Use either a pipette or a syringe needle to break up the heart pieces. For the larger pieces use a 10mL pipette and then go to a 5mL pipette, 18G syringe needle and then a 20G syringe needle for each progressive cycle.
13. Allow the heart pieces to settle and pour supernatant into a 50mL tube labeled **R**. Add KRB w/ HS to **R** to reach 30mL mark. Place tube **R** in centrifuge @ **8min, 25 degrees (room temp), at 1000 rpm**.
14. Once **R** is done spinning, remove supernatant into waste and resuspend pellet in 5mL KRB w/ HS. All subsequent **R** tubes will be resuspended into this first tube.
15. Add 8mL of collagenase to tube **H** and place in water bath @ **10min, 37 degrees, at 85 rpm**. Repeat from step 12 by adding 1mL DNAse until heart pieces are totally digested.
16. Take total resuspended heart cells from tube **R** and filter through 40um cell strainers into a 50mL tube. Replace strainer if it gets full/clogged.
17. Add fibroblast media to reach the 7.5mL mark. Add 7.5mL fibroblast media into a T75 Flask and add the cell suspension into the flask. Label the flask Fibroblasts, p0 and the date. Keep flask in incubator @ **37 degrees and 5% CO2 for 30 min**. After 30min remove media and place in a 50mL tube labeled **S**. Add 15mL fibroblast media to the flask and place back into incubator.
18. Count cells in tube **S**. Then add Fibroblast media to reach 30mL mark and spin in centrifuge @ **8min, 25 degrees (room temp), at 1000 rpm**. After done spinning, remove supernatant and resuspend in fibroblast media to reach a concentration of maximum 5E6 cells/mL
19. Take this cell suspension and add to Percoll columns. **DO NOT EXCEED 5E6 CELLS PER COLUMN**. **DO NOT MIX LAYERS**. Spin the columns @ **20min, 25 degrees, at 2000 rpm**.
20. After the spin carefully remove the layer in between **Percoll A** and **Percoll B** (top pink and clear layer) and add to a 50mL tube. These are myocytes. Place 4 myocyte layers in 1 50mL tube.
21. Fill each 50mL tube with myocyte media to reach the 50mL mark and spin in centrifuge @ **8min, 25 degrees (room temp), at 1000 rpm**.
22. Remove supernatant from tubes and resuspend in one tube. Count cells.

Polyacrylamide Gel Protocol

Materials

- No.1 coverslip, 45x50 mm rectangular and 22 mm circular.
- NaOH, 0.1 N, 100 ml.
- 3-aminopropyltrimethoxy silane.
- PBS, 500 ml.
- Glutaraldehyde, 0.5%. Mix 357 ul of 70% glutaraldehyde with 50 ml of PBS. Keep the 70 % stock tightly sealed in zip bags in a closed container at 4^{o}C.
- HEPES, 1 M, pH 8.5, 1 ml and 50 mM, pH 8.5, 500 ml. Use at room temperature.
- Fluorescent latex beads, 0.2 um diameter.

- Acrylamide (40%, Bio-Rad) and Bis (2%, Bio-Rad).
- Ammonium persulfate (Bio-Rad) solution, 10 mg in 100ul distilled water. Prepare immediately before use in step 10.
- TEMED (Bio-Rad).
- Sulfo-SANPAH (Pierce), 0.5 mg/ml in 50 mM HEPES pH 8.5, need 400 ul per dish. PREPARE IMMEDIATELY BEFORE USE IN STEP 15. Handle sulfo-SANPAH in the dark. Weigh the appropriate amount, add 1 ul DMSO per mg of sulfo-SANPAH. While vortexing, add 50 mM HEPES at room temperature to obtain the final concentration.
- Protein solution for coating the substrate. Use type I collagen (10 mg/ml stock), at 0.2 mg/ml (40 ul + 2 ml PBS), or fibronectin at 10 ug/ml in a volume of 2 ml.

Procedure

1. Mark one side of a #1 cover slip with a diamond tip pen. Pass the marked side over the inner flame of a Bunsen burner.

2. Place the cover slip, flamed side up, on a test tube rack. Smear the surface with 0.1 N NaOH in the hood and allow the surface to air dry.

3. Smear the dried surface with 3-aminopropyltrimethoxy silane, wear gloves and do this in the hood. Incubate at room temperature for 5 minutes.

4. Collect the cover slips in a pan. Wash with distilled water on a shaker until the cover slip surfaces are clear.

5. Put the cover slips back on test tube rack. Pipette 0.5 % gluteraldehyde to cover the treated surface of the cover slips. Incubate for 30 minutes at room temperature in the hood. Ware gloves.

6. Collect the used glutaraldehyde in liquid waste. Wash as in step 4 and let air-dry. Activated cover slip may be stored in a dessicator for two weeks. Cover slips may be mounted onto chamber dishes before proceeding with the following steps.

7. Mix 5 ml of acrylamide solution in a small beaker according to the dilution scheme below.

Final Acryl/Bis	**40%Acrylamide**	**2%Bis**	**1M HEPES**	**H_20**	**Young's Modulus**
8%/0.1%	1000 ul	250 ul	50 ul	3700 ul	?? kN/m2
8/0.08	1000	200	50	3750	75
8/0.06	1000	150	50	3800	30
8/0.05	1000	125	50	3825	23
8/0.04	1000	100	50	3850	17
8/0.03	1000	75	50	3875	14
8/0.02	1000	50	50	3900	10
5/0.12	625	300	50	4025	33
5/0.10	625	250	50	4075	28

5/0.08	625	200	50	4125	24
5/0.06	625	150	50	4175	15
5/0.025	625	63	50	4262	7

8. Degas the solution for 20 minutes to remove oxygen, which inhibits acrylamide polymerization.

9. Sonicate the fluorescent beads for 1-2 minutes in a bath sonicator.

10. Add beads, 30 ul ammonium persulfate, 20 ul TEMED. Seal the beaker with parafilm and mix gently by swirling.

11. Pipette the acrylamide mixture onto the activated cover slip. Use 15 ul for a 75 um-thick gel. Quickly place a 22 mm circular cover slip onto the acrylamide droplet and invert the chamber dish.

12. Let acrylamide polymerize for 30 minutes.

13. Flood the surface with ~2 ml of 50 mM HEPES. Remove the circular cover slip with two pairs of fine tipped tweezers.

14. Rinse the substrate well with 50 mM HEPES. The substrate may be stored at 4^{o}C for 2 weeks.

15. Remove as much liquid form the substrate as possible without drying, then layer 200 ul of the sulfo-SANPAH solution on top.

16. Place under 302 nm UV, at a distance of 2-3 inches from two 15W tubes, for 5-8 minutes. The solution will darken when activated.

17. Repeat steps 15 and 16

18. Wash with 50 mM HEPES to remove excess reagent. Do this quickly.

19. Add the protein to be coupled and incubate either 4 hours at room temperature or overnight in the cold room on a shaker.

20. Rinse with PBS and store coated substrates in the cold room for up to a week.

21. Before plating cells, expose the gel to UV for 15 minutes.

22. Replace PBS with complete culture medium. Place in incubator for 1 hour to allow equilibrium.

Myocyte Media

Chemicals

- 6.685g Dulbecco's Modified Eagle Medium (13.37 g/L) (DMEM)
- 600mg Sodium Bicarbonate $NaHCO_3$ (1.2 g/L)
- 1.787 g HEPES (15mM)
- 40mL (8%) Horse Serum (HS)
- 25mL (5%) Newborn Calf Serum (NCS)

- 5mL (1%) Penicillin/Streptomycin (Pen/Strep or Anti/Anti)
- 2 mL Cytosin β-D-arabinofuranoside (ara-C) (100mg/100mL Moscona's Saline)
- 1 mL Amphotericin B (50mg/100mL dH_2O)

Procedure

1. Measure and put 430mL of distilled water into an autoclaved 500mL beaker
2. Weigh and add the DMEM, $NaHCO_3$, and HEPES to the beaker
3. pH to 7.4
4. Filter with a 0.22m filter unit
5. Add the HS, NCS, Pen/Strep, and ara-C to the media
6. Date & Label and place in the refrigerator

Fibroblast Media

Chemicals

- 6.685g Dulbecco's Modified Eagle Medium (13.37 g/L) (DMEM)
- 600mg Sodium Bicarbonate $NaHCO_3$ (1.2 g/L)
- 1.787 g HEPES (15mM)
- 50mL (10%) Newborn Calf Serum (NCS)
- 25mL (5%) Fetal Bovine Serum (FBS)
- 5mL (1%) Penicillin/Streptomycin (Pen/Strep or Anti/Anti)
- 500 mL Gentamicin

Procedure

1. Measure and put 420 mL of distilled water into an autoclaved 500 mL beaker
2. Weigh and add the DMEM, $NaHCO_3$, and HEPES to the beaker
3. pH to 7.4
4. Filter with a 0.22m filter unit
5. Add the NCS, FBS, Pen/Strep, and Gentamicin to the media
6. Date & Label and place in the refrigerator

Moscona's Saline

Chemicals

- 8g Sodium Chloride (NaCl)
- 200mg Potassium Chloride (KCl)
- 1g of Sodium Bicarbonate ($NaHCO_3$)
- 1.7g Glucose
- 5mg Sodium Phosphate Monohydrate ($NaH_2PO_4 \bullet H_2O$)

Procedure

1. Combine NaCl, KCl, $NaHCO_3$, Glucose and NaH_2PO_4 in 1L of distilled water in an autoclaved 1L beaker

2. pH to 7.4
3. Filter with a 0.22m filter unit
4. Date & Label and place in the refrigerator

Kreb's Ringers Bicarbonate buffer (KRB)

Chemicals

- 3.46g Sodium Chloride (NaCl)
- 0.146g Magnesium Sulphate ($MgSO_4$)
- 0.177g Potassium Chloride (KCl)
- 1.05g Sodium Bicarbonate ($NaCO_3$)
- 0.081g Potassium Phosphate Monobasic (KH_2PO_4)
- 1mL of Phenol Red (1mg/mL)

Procedure

1. Measure and put 500 mL of distilled water into an autoclaved 500 mL beaker
2. Add NaCl, $MgSO_4$, KCl, $NaCO_3$, KH_2PO_4 and Phenol Red to the beaker
3. pH to 7.4
4. Filter with a 0.22m filter unit
5. Date & Label and place in the refrigerator

References

The following are the references used in this thesis:

1. Klabunde, R., *Cardiovascular Physiology Concepts*. 2004: Lippincott Williams & Wilkins.

2. Guyton, A.C. and J.D. Hall, *Textbook of Medical Physiology*. 11 ed. 2005: Elsevier Science Health Science Div.

3. Kung, *National Vital Statistics Report.* CDC Bulletin, 2008. **56**(10).

4. Zhuang, J.P., et al., *Pulsatile stretch remodels cell-to-cell communication in cultured myocytes.* Circulation Research, 2000. **87**(4): p. 316-322.

5. Dorn, G.W., J. Robbins, and P.H. Sugden, *Phenotyping hypertrophy - Eschew obfuscation.* Circulation Research, 2003. **92**(11): p. 1171-1175.

6. Leri, A., J. Kajstura, and P. Anversa, *Myocyte proliferation and ventricular remodeling.* J Card Fail, 2002. **8**(6 Suppl): p. S518-25.

7. Schaub, M.C., et al., *Various hypertrophic stimuli induce distinct phenotypes in cardiomyocytes.* Journal of Molecular Medicine, 1997. **75**(11-12): p. 901-920.

8. Borg, T.K., et al., *The cell biology of the cardiac interstitium.* Trends in Cardiovascular Medicine, 1996. **6**(2): p. 65-70.

9. Simpson, D.G., et al., *Mechanical regulation of cardiac myocyte protein turnover and myofibrillar structure.* American Journal of Physiology-Cell Physiology, 1996. **39**(4): p. C1075-C1087.

10. Khan, M.G., *Encyclopedia of Heart Diseases*. 1 ed. 2000: Academic Press.

11. Paulev, P.-E., *Textbook in Medical Physiology And Pathophysiology: Essentials and clinical problems*. 1999: Copenhagen Medical Publishers.

12. Ingber, D.E., *Mechanical signalling and the cellular response to extracellular matrix in angiogenesis and cardiovascular physiology.* Circulation Research, 2002. **91**(10): p. 877-887.

13. Ingber, D.E., *Mechanobiology and diseases of mechanotransduction.* Annals of Medicine, 2003. **35**(8): p. 564-577.

14. Booz, G.W. and K.M. Baker, *Actions of angiotensin II on isolated cardia myocytes.* Heart Failure Reviews, 1998. **3**: p. 125-130.

15. Bouzegrhane, F. and G. Thibault, *Is angiotensin II a proliferative factor of cardiac fibroblasts?* Cardiovascular Research, 2002. **53**(2): p. 304-312.

16. Black, F.M., et al., *The vascular smooth muscle alpha-actin gene is reactivated during cardiac hypertrophy provoked by load.* J Clin Invest, 1991. **88**(5): p. 1581-8.

17. Kumar, A., et al., *Rescue of cardiac alpha-actin-deficient mice by enteric smooth muscle gamma-actin.* Proc Natl Acad Sci U S A, 1997. **94**(9): p. 4406-11.

18. Sugiura, S., et al., *Comparison of unitary displacements and forces between 2 cardiac myosin isoforms by the optical trap technique: molecular basis for cardiac adaptation.* Circ Res, 1998. **82**(10): p. 1029-34.

19. Winegrad, S., *How actin-myosin interactions differ with different isoforms of myosin.* Circ Res, 1998. **82**(10): p. 1109-10.

20. Borisov, A.B., M.G. Martynova, and M.W. Russell, *Early incorporation of obscurin into nascent sarcomeres: implication for myofibril assembly during cardiac myogenesis.* Histochem Cell Biol, 2008.

21. Chung, C.Y., H. Bien, and E. Entcheva, *The role of cardiac tissue alignment in modulating electrical function.* J Cardiovasc Electrophysiol, 2007. **18**(12): p. 1323-9.

22. Carver, W., et al., *Collagen expression in mechanically stimulated cardiac fibroblasts.* Circ Res, 1991. **69**(1): p. 116-22.

23. Brooks, G., R.A. Poolman, and J.M. Li, *Arresting developments in the cardiac myocyte cell cycle: role of cyclin-dependent kinase inhibitors.* Cardiovasc Res, 1998. **39**(2): p. 301-11.

24. Sussman, M.A., A. McCulloch, and T.K. Borg, *Dance band on the Titanic - Biomechanical signaling in cardiac hypertrophy.* Circulation Research, 2002. **91**(10): p. 888-898.

25. Diamond, J.A. and R.A. Phillips, *Hypertensive heart disease.* Hypertens Res, 2005. **28**(3): p. 191-202.

26. Dostal, D.E., *Regulation of cardiac collagen - Angiotensin and cross-talk with local growth factors.* Hypertension, 2001. **37**(3): p. 841-844.

27. Fredj, S., et al., *Interactions between cardiac cells enhance cardiomyocyte hypertrophy and increase fibroblast proliferation.* Journal of Cellular Physiology, 2005. **202**(3): p. 891-899.

28. Frey, N. and E.N. Olson, *Cardiac hypertrophy: The good, the bad and the ugly.* Annual Review of Physiology, 2003. **65**: p. 45-79.

29. Gilbert, S.F., *Developmental Biology*. 7 th ed. 2003, Sunderland: Sinauer Associates.

30. Glennon, P.E., P.H. Sugden, and P.A. Poolewilson, *Cellular Mechanisms of Cardiac-Hypertrophy.* British Heart Journal, 1995. **73**(6): p. 496-499.

31. Sadoshima, J. and S. Izumo, *The cellular and molecular response of cardiac myocytes to mechanical stress.* Annual Review of Physiology, 1997. **59**: p. 551-571.

32. Simpson, D.G., et al., *Regulation of cardiac myocyte protein turnover and myofibrillar structure in vitro by specific directions of stretch.* Circulation Research, 1999. **85**(10): p. E59-E69.

33. Zou, Y.Z., et al., *Molecular and cellular mechanisms of mechanical stress-induced cardiac hypertrophy.* Endocrine Journal, 2002. **49**(1): p. 1-13.

34. Anversa, P., et al., *Myocyte growth and cardiac repair.* Journal of Molecular and Cellular Cardiology, 2002. **34**(2): p. 91-105.

35. Fuster, V., et al., *Hurst's The Heart*. 10th ed, ed. M.-H.C. Inc. 2001, New York, NY. 115-1125.

36. Clark, E.B., R.R. Markwald, and A. Takao, eds. *Developmental mechanisms of heart disease*. 1995, Futura Pub: Armonk.

37. Chen, L., et al., *Opposing cardioprotective actions and parallel hypertrophic effects of delta PKC and epsilon PKC.* Proc Natl Acad Sci U S A, 2001. **98**(20): p. 11114-9.

38. Dorn, G.W., 2nd, et al., *Myosin heavy chain regulation and myocyte contractile depression after LV hypertrophy in aortic-banded mice.* Am J Physiol, 1994. **267**(1 Pt 2): p. H400-5.

39. Swynghedauw, B., *Developmental and functional adaptation of contractile proteins in cardiac and skeletal muscles.* Physiol Rev, 1986. **66**(3): p. 710-71.

40. Swynghedauw, B., *Cardiac Hypertrophy and Failure*. 1990: Libbey Eurotext. 792.

41. Swynghedauw, B., et al., *Molecular and cellular biology of the senescent hypertrophied and failing heart.* Am J Cardiol, 1995. **76**(13): p. 2D-7D.

42. Eppenberger, M.E., et al., *Immunocytochemical analysis of the regeneration of myofibrils in long-term cultures of adult cardiomyocytes of the rat.* Dev Biol, 1988. **130**(1): p. 1-15.

43. Eppenberger-Eberhardt, M., et al., *Reexpression of alpha-smooth muscle actin isoform in cultured adult rat cardiomyocytes.* Dev Biol, 1990. **139**(2): p. 269-78.

44. Eppenberger-Eberhardt, M., et al., *New occurrence of atrial natriuretic factor and storage in secretorially active granules in adult rat ventricular cardiomyocytes in long-term culture.* J Mol Cell Cardiol, 1993. **25**(7): p. 753-7.

45. Nag, A.C. and M. Cheng, *Biochemical evidence for cellular dedifferentiation in adult rat cardiac muscle cells in culture: expression of myosin isozymes.* Biochem Biophys Res Commun, 1986. **137**(2): p. 855-62.

46. Gradman, A., et al., *Predictors of total mortality and sudden death in mild to moderate heart failure. Captopril-Digoxin Study Group.* J Am Coll Cardiol, 1989. **14**(3): p. 564-70; discussion 571-2.

47. Kannel, W.B., J.F. Plehn, and L.A. Cupples, *Cardiac failure and sudden death in the Framingham Study.* Am Heart J, 1988. **115**(4): p. 869-75.

48. SOLVD, *Effect of enapril on survival in patients with reduced left ventricular ejection fractions and congestive heart failure.* N Engl J Med, 1991. **335**: p. 293-302.

49. Dodge, S.M., et al., *Effects of angiotensin II on expression of the gap junction channel protein connexin43 in neonatal rat ventricular myocytes.* J Am Coll Cardiol, 1998. **32**(3): p. 800-7.

50. Peters, N.S., et al., *Reduced content of connexin43 gap junctions in ventricular myocardium from hypertrophied and ischemic human hearts.* Circulation, 1993. **88**(3): p. 864-75.

51. Eppenberger, H.M., C. Hertig, and M. Eppenbergereberhardt, *Adult-Rat Cardiomyocytes in Culture - a Model System to Study the Plasticity of the Differentiated Cardiac Phenotype at the Molecular and Cellular-Levels.* Trends in Cardiovascular Medicine, 1994. **4**(4): p. 187-193.

52. Hertig, C.M., et al., *N-cadherin in adult rat cardiomyocytes in culture .2. Spatio-temporal appearance of proteins involved in cell-cell contact and communication. Formation of two distinct N-cadherin/catenin complexes.* Journal of Cell Science, 1996. **109**: p. 11-20.

53. Simpson, D.G., et al., *Modulation of Cardiac Myocyte Phenotype in-Vitro by the Composition and Orientation of the Extracellular-Matrix.* Journal of Cellular Physiology, 1994. **161**(1): p. 89-105.

54. Wijffels, M.C., et al., *Atrial fibrillation begets atrial fibrillation. A study in awake chronically instrumented goats.* Circulation, 1995. **92**(7): p. 1954-68.

55. Ausma, J., et al., *Dedifferentiation of atrial cardiomyocytes as a result of chronic atrial fibrillation.* Am J Pathol, 1997. **151**(4): p. 985-97.

56. Sharov, V.G., et al., *Evidence of cardiocyte apoptosis in myocardium of dogs with chronic heart failure.* Am J Pathol, 1996. **148**(1): p. 141-9.

57. Dispersyn, G.D., D.W. Donker, and P.G.A. Volders, *Aspects of cardiomyocyte dedifferentiation accompany biventricular hypertrophy in dogs with chronic complete AV block.* Europace, 2000. **1**(B23).

58. Ausma, J. and M. Borgers, *Dedifferentiation of atrial cardiomyocytes: from in vivo to in vitro.* Cardiovascular Research, 2002. **55**(1): p. 9-12.

59. Ausma, J., et al., *Structural changes of atrial myocardium due to sustained atrial fibrillation in the goat.* Circulation, 1997. **96**(9): p. 3157-63.

60. Rucker-Martin, C., et al., *Dedifferentiation of atrial myocytes during atrial fibrillation: role of fibroblast proliferation in vitro.* Cardiovasc Res, 2002. **55**(1): p. 38-52.

61. Marian, A.J. and R. Roberts, *Recent advances in the molecular genetics of hypertrophic cardiomyopathy.* Circulation, 1995. **92**(5): p. 1336-47.

62. Wolf, C.M., et al., *Somatic events modify hypertrophic cardiomyopathy pathology and link hypertrophy to arrhythmia.* Proc Natl Acad Sci U S A, 2005. **102**(50): p. 18123-8.

63. Neissen, C.M., *Tight Junctions/Adherens Junctions: Basic Structure and Function.* Journal of Investigative Dermatology, 2007. **127**: p. 2525-2532.

64. Ilic, D., et al., *Reduced cell motility and enhanced focal adhesion contact formation in cells from FAK-deficient mice.* Nature, 1995. **377**(6549): p. 539-44.

65. Frame, M.C., et al., *v-Src's hold over actin and cell adhesions.* Nat Rev Mol Cell Biol, 2002. **3**(4): p. 233-45.

66. Angers-Loustau, A., et al., *Protein tyrosine phosphatase-PEST regulates focal adhesion disassembly, migration, and cytokinesis in fibroblasts.* J Cell Biol, 1999. **144**(5): p. 1019-31.

67. Tan, J.L., et al., *Cells lying on a bed of microneedles: an approach to isolate mechanical force.* Proc Natl Acad Sci U S A, 2003. **100**(4): p. 1484-9.

68. Cukierman, E., et al., *Taking cell-matrix adhesions to the third dimension.* Science, 2001. **294**(5547): p. 1708-12.

69. Wang, H.B., et al., *Focal adhesion kinase is involved in mechanosensing during fibroblast migration.* Proc Natl Acad Sci U S A, 2001. **98**(20): p. 11295-300.

70. Lorell, B.H. and B.A. Carabello, *Left ventricular hypertrophy - Pathogenesis, detection, and prognosis.* Circulation, 2000. **102**(4): p. 470-479.

71. Dembo, M., et al., *Imaging the traction stresses exerted by locomoting cells with the elastic substratum method.* Biophysical Journal, 1996. **70**(4): p. 2008-2022.

72. Cooper, G.t. and R.J. Tomanek, *Load regulation of the structure, composition, and function of mammalian myocardium.* Circ Res, 1982. **50**(6): p. 788-98.

73. Komuro, I., et al., *Stretching cardiac myocytes stimulates protooncogene expression.* J Biol Chem, 1990. **265**(7): p. 3595-8.

74. Kijima. K, et al., *Mechanical Stretch Induces Enhanced Expression of Angiotensin II Receptor Subtypes in Neonatal Rat Cardiac Myocytes.* Circulation Research, 1996. **79**: p. 887-897.

75. Vandenburgh, H. and S. Kaufman, *In vitro model for stretch-induced hypertrophy of skeletal muscle.* Science, 1979. **203**(4377): p. 265-8.

76. Gopalan, S.M., et al., *Anisotropic stretch-induced hypertrophy in neonatal ventricular myocytes micropatterned on deformable elastomers.* Biotechnology and Bioengineering, 2003. **81**(5): p. 578-587.

77. Kang, T. and F.C. Yin, *The need to account for residual strains and composite nature of heart wall in mechanical analyses.* American Journal of Physiology, 1996. **271**: p. H947-H961.

78. Lee, A.A., et al., *An equibiaxial strain system for cultured cells.* Am J Physiol, 1996. **271**(4 Pt 1): p. C1400-8.

79. Leri, A., et al., *Up-regulation of AT(1) and AT(2) receptors in postinfarcted hypertrophied myocytes and stretch-mediated apoptotic cell death.* Am J Pathol, 2000. **156**(5): p. 1663-72.

80. Gudi, S.R., et al., *Equibiaxial strain and strain rate stimulate early activation of G proteins in cardiac fibroblasts.* Am J Physiol, 1998. **274**(5 Pt 1): p. C1424-8.

81. Rana, O.R., et al., *A simple device to apply equibiaxial strain to cells cultured on flexible membranes.* Am J Physiol Heart Circ Physiol, 2008. **294**(1): p. H532-40.

82. Bhatia, S.N., M.L. Yarmush, and M. Toner, *Micropatterning cells in tissue engineering*. Methods in Molecular Medicine, ed. N.J. Totowa. 1998: Humana Press.

83. Harris, A.K., P. Wild, and D. Stopak, *Silicone rubber substrata: a new wrinkle in the study of cell locomotion.* Science, 1980. **208**(4440): p. 177-9.

84. Lee, J., et al., *Traction forces generated by locomoting keratocytes.* J Cell Biol, 1994. **127**(6 Pt 2): p. 1957-64.

85. Oliver, T., M. Dembo, and K. Jacobson, *Traction forces in locomoting cells.* Cell Motil Cytoskeleton, 1995. **31**(3): p. 225-40.

86. Oliver, T., K. Jacobson, and M. Dembo, *Design and use of substrata to measure traction forces exerted by cultured cells.* Methods Enzymol, 1998. **298**: p. 497-521.

87. Dembo, M. and Y.L. Wang, *Stresses at the cell-to-substrate interface during locomotion of fibroblasts.* Biophysical Journal, 1999. **76**(4): p. 2307-2316.

88. Pelham, R.J. and Y.-L. Wang, *Cell locomotion and focal adhesions are regulated by substrate flexability.* Proc Natl Acad Sci U S A, 1997. **94**: p. 13661-13665.

89. Wang, Y.L. and R.J. Pelham, *Preparation of a flexible, porous polyacrylamide substrate for mechanical studies of cultured cells.* Molecular Motors and the Cytoskeleton, Pt B, 1998. **298**: p. 489-496.

90. Marganski, W.A., M. Dembo, and Y.L. Wang, *Measurements of cell-generated deformations on flexible substrata using correlation-based optical flow.* Biophotonics, Pt B, 2003. **361**: p. 197-211.

91. Bernardo, J.M. and A.F.M. Smith, *Bayesian Theory*. 1994, Chichester: John Wiley & Sons.

92. Bloom, R.J. and G.P. George, *Mapping Local Matrix Remodeling Induced by a Migrating Tumor Cell Using Three-Dimensional Multiple-Particle Tracking.* Biophysical Journal, 2008. **95**(8): p. 4077 - 4088.

93. Lu, L., et al., *Mechanical Properties of Actin Stress Fibers in Living Cells.* Biophysical Journal, 2008. **95**(12): p. 6060-6071.

94. Munevar, S., Y.L. Wang, and M. Dembo, *Regulation of mechanical interactions between fibroblasts and the substratum by stretch-activated Ca2+ entry.* Journal of Cell Science, 2004. **117**(1): p. 85-92.

95. Odde, D.J. and M.J. Renn, *Laser-guided direct writing for applications in biotechnology.* Trends in Biotechnology, 1999. **17**(10): p. 385-389.

96. Rohr, S., R. Fluckiger-Labrada, and J.P. Kucera, *Photolithographically defined deposition of attachment factors as a versatile method for patterning the growth of different cell types in culture.* Pflugers Archiv-European Journal of Physiology, 2003. **446**(1): p. 125-132.

97. Odde, D.J. and M.J. Renn, *Laser-guided direct writing of living cells.* Biotechnology and Bioengineering, 2000. **67**(3): p. 312-318.

98. Renn, M.J. and R. Pastel, *Particle manipulation and surface patterning by laser guidance.* Journal of Vacuum Science & Technology B, 1998. **16**(6): p. 3859-3863.

99. Borg, T.K. *The dynamic interaction between the extracellular matrix and cellular components of the heart*. in *Symposium on Dynamic Bio-Nano-Fibers in the Cells Focusing Human Body: Cells is being organized with nano-bibers*. 2004. National Museum of Emerging Science and Innovation, Tokyo.

100. Borg, T.K., et al., *The role of the extracellular matrix (ECM) in cardiac development.* Faseb Journal, 2003. **17**(4): p. A359-A359.

101. Borg, T.K., et al., *Recognition of extracellular matrix components by neonatal and adult cardiac myocytes.* Developmental Biology, 1984. **104**: p. 86-96.

102. Costa, K.D., E.J. Lee, and J.W. Holmes, *Creating alignment and anisotropy in engineered heart tissue: Role of boundary conditions in a model three-dimensional culture system.* Tissue Engineering, 2003. **9**(4): p. 567-577.

103. Thompson, N.I. and B.Z. Gao, *Alignment of extracellular matrix in a patterned cardiac fibroblast culture.* Molecular Biology of the Cell, 2003. **14**: p. 221a.

104. Landau, R.H., M.J. Paez, and C.B. Cristian, *A Survey of Computational Physics*. 2008, Princeton: Princeton University Press.

105. Fung, Y.C., *Continuum Mechanics*. 1969, Englewood Cliffs, N.J.: Prentice-Hall.

106. Bakken, D., et al. *Laser Micropatterning Of Polylactide Microspheres Into Neuronal-Glial Coculture To Quantitatively Study Axonal Regeneration*. in *The Polymer Network Conference*. 2004. Bethesda, MD.

107. Narasimhan, S., *Laser Cell Micropatterning System*, in *Bioengineering*. 2004, Clemson University: Clemson, SC.

108. Narasimhan, S.V., et al., *Multiple Beam Laser Cell Micropatterning System.* Proceedings of SPIE, 2004. **5514**: p. 437-446.

109. Barren, J.L., D.J. Fleet, and S.S. Beauchemin, *Performance of Optical Flow Techniques.* IEEE Engineering in Medicine and Biology Magazine, 1992.

110. Barren, J.L., D.J. Fleet, and S.S. Beauchemin, *Performance of Optical Flow Techniques.* International Journal of Computer Vision, 1994. **12**(1): p. 43-77.

111. Landau, L.D. and E.M. Lifshitz, *Theory of Elasticity*. 3 ed. 1984: Pergamon Press.

112. Timoshenko, S., *Theory of Elasticity*. 1934, New York: McGraw-Hill.